

國立臺灣大學理學院物理學研究所

博士論文

Institute of Physics

College of Science

National Taiwan University

Doctoral dissertation



磁流體與波型態的暗物質

Magnetohydrodynamcis and Wave Dark Matter

張瑋瀚

Ui-Han Zhang

指導教授：闕志鴻 博士

Advisor: Tzihong Chiueh, Ph.D.

中華民國 106 年 7 月

July, 2017





國立臺灣大學博士學位論文  
口試委員會審定書

磁流體與波型態的暗物質

Magnetohydrodynamics and Wave Dark Matter

本論文係張瑋瀚君 (D00222003) 在國立臺灣大學物理學研究  
所完成之博士學位論文，於民國 106 年 7 月 21 日承下列考試委員  
審查通過及口試及格，特此證明

口試委員：

關志鴻

陳秋華

吳建宏

陳宜良

梅津敬一





## 誌謝

大學四年，碩士班兩年，博士班六年，總共十二年的光陰，總算拿到在台灣大學的第三張畢業證書。這部分首先要感謝我的指導教授，闕志鴻教授。從碩士就進入此實驗室到現在共八個年頭，跟著闕教授做了好幾個研究案子-儀器製作，訊號處理，恆星形成，電漿物理以及暗物質。在每個專題研究中，都可以體驗到闕教授源源不絕的想法，以及他對研究的堅持與熱誠，著實欽佩。再來感謝口委們，陳秋榮教授、陳宜良教授、吳建宏教授以及梅津敬一教授。謝謝您們寶貴的意見以及容忍我的破英文和對您們問題的誤解。

感謝實驗室的大家與我一起奮鬥。跟我同期的老滕、阿邦、Sid、簡鴻裕學長、小光、小于、姝蓉、弘旭與彥麟兄，謝謝你們一同與我喝酒及聊天，甚至與老滕、小光與小于一同合歡山一日遊及單攻玉山。老滕我跟你差了十七歲還可以認識真是有緣分，也是因為你帶我進入了通訊領域。小于，沒有你我可能很難把磁流體完成，但還是抱怨一下不要自己寫的程式自己都忘記寫甚麼，這樣我很難改程式。弘旭我們一起去日本開會認識南韓妹及搭訕大阪妹如今歷歷在目。姝蓉謝謝妳容許我偷吃妳的零食。彥麟兄謝謝你陪我聊金庸與歷史。小我兩屆的李忠翰、廖明璿、吳佳鴻、小潘、若有、陳之藩、黃聖凱、賴打及謝侑廷，謝謝你們帶給實驗室熱鬧，我不會忘記一起登雪山看日出的情景。這兩三年加入實驗室的許家榮、黃冠維、黃彥凱、梁家豪及趙子翔讓我博士班最後幾年有人可以嘴砲。前輩的意見要聽，否則很容易步入萬劫不復的深淵。

感謝實驗室助理惠敏處理實驗室大大小小的行政事務及倒垃圾，祝妳未來在澳洲一切順利。其他實驗室的曾之寅、魏瑀潔、羅文斌、劉宗哲，邱奕儂、亮亮及李傳睿，謝謝你們讓我可以串門子以及陪我聊天與抱怨。大學同學發主席、鄭為晉、黃彥鈞、馮聖元及洪國華，謝謝你們有聚會或回國都沒忘邀請我。台大田徑隊的大家，由於待在學校太久，上到大我十二屆，下到小我十二屆都有認識，族譜龐大在此不一一詳載。總之很感謝大家讓我除了研究外還有另一個自在天地。其中佳佑、胤翔、俊傑、梓桓、維康家舍這對賢伉儷，謝謝你們百忙之中抽空陪我跑步練課表。陳廷軒是男人就勇敢地去追，不要讓我又賭輸給瘦哥。國中同學們，謝謝你們的陪伴，十八年的友誼不是混假的。其中湯沂、安吟及阿瑞，謝謝你們在我很谷底時拉我一把，特地來台北來看我。小淳雖然我知道你交女朋友後會變得很難約，但有空還是回桃園一起跑步。肥肥我未來一年會經常跑虎頭山去光顧你的簡餐店的。

感謝我人生的另一半伊庭，感謝妳無怨無悔地陪著我。雖然很抱歉從碩士畢業到博士畢業，女朋友的頭銜尚未改變，但我不會讓妳一直是這頭銜的。感謝伊庭爸媽對我的支持，也很謝謝您們常送手工肥



皂給我使用。也感謝伊庭的同事們，蘿絲、雅珽、Apple、壽民以及家聲，謝謝你們不把我當外人而當成自己人一樣的對待。最後要感謝我的家人，爸爸媽媽、大哥大嫂、二哥二嫂及三位姪子。謝謝你們的鼓勵，縱使家族出現一些變革也一肩扛起讓我無後顧之憂地完成學業。尤其是爸爸，您是我的榜樣。我會讀博班應是受到您的影響。謝謝您縱使這兩年身體出現變故也不忘了關心我的研究進度。非常感謝您對我的用心與支持。

結束了學生身份，要往下一個人生階段邁進。雖然不知道未來的路是怎樣，但我相信順著自己內心的目標持續努力不懈，總有開花結果之時。



## 摘要

GAMER 是一個利用繪圖處理單元 (Graphic-processing-unit, GPU) 加速及自適網格解析度調整 (Adaptive-Mesh-Refinement, AMR) 的天文物理應用模擬程式。此程式已順利擴展成可以數值模擬磁流體動力學 (Magnetohydrodynamics, MHD)。磁流體動力學的數值模擬演算法是具有限制傳輸 (Constraint transport, CT) 技術的逆流邊角傳輸 (Corner-transport-upwind, CTU) 演算法。另一方面，散度保持算符 (Divergent preserving operator) 保證了自適網格解析度調整中磁場的零散度條件。模擬結果顯示磁流體 GAMER 程式跟其他高解析度均勻網格模擬一樣準確。我們引進一個新的三維測試問題。在此問題中，磁場滿足阿諾德-貝爾特拉米-柴爾德里斯 (Arnold-Beltrami-Childress) 樣態。這樣的電漿組態一開始會變成有片狀電流密度的紊流，但最後將收斂到最低能量的平衡態。此測試問題很適合檢驗本程式的效能。本程式在單一 K20X 的繪圖處理單元下每秒可以演化  $2 \times 10^7$  個網格，比藍水 (Blue Waters) 超級電腦上的一顆擁有 16 個核心的中央處理單元 (Center-processing-unit, CPU) 快 25 倍。我們同時發現當使用 1024 個藍水超級電腦的計算節點，此程式的平行效率可高達 70 個百分點。

我們分析在輻射主宰時期的波形態暗物質，或者稱作  $\psi$  暗物質之線性微擾。在此分析中， $\psi$  暗物質微擾的演化可分成四個階段。其中在質量震盪 (Mass oscillation) 之後的晚期階段，長波的  $\psi$  暗物質微擾幾乎和冷暗物質 (Cold dark matter, CDM) 模型雷同。然而對於中短波的情況，在整個演化過程中，沒有一個階段跟冷暗物質一樣。我們同時討論餘弦型態純量場勢能的軸子模型 (Axion model)。軸子模型的演化幾乎與  $\psi$  暗物質相同。但當軸子初始角度非常靠近勢能的頂端，有三個新特徵會顯現。其中最新穎的特徵是在某些波數的範圍內，頻譜會比冷暗物質高。這樣的差異可能會非常大以致於造成紅移 10 以上的

高紅移宇宙有顯著的改變。亞視界 (Sub-horizon) 的擾動可以被馬蒂厄 (Mathieu) 方程式準確地描述且受到參數不穩定 (Parametric instability) 的影響。這解釋了此新穎的特徵。

關鍵字：磁流體動力學，繪圖處理單元，自適網格解析度調整，波形態暗物質，輻射主宰時期，軸子模型。

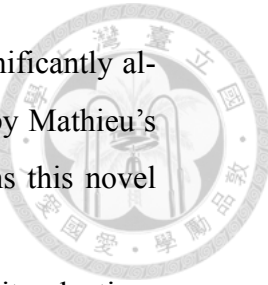




# Abstract

GAMER, a Graphic-processing-unit-accelerated Adaptive-MEsh-Refinement Astrophysical code, is extended to support magnetohydrodynamics (MHD), where the solver features the corner-transport-upwind (CTU) scheme with the constraint transport (CT) technique. The divergent preserving operator for adaptive mesh refinement (AMR) is applied to reinforce the divergence-free constraint on the magnetic field. Numerical results show GAMER-MHD is as robust as those given by high-resolution uniform-grid runs. We explore a new 3D MHD test, where the magnetic field assumes the Arnold-Beltrami-Childress (ABC) configuration, temporarily becomes turbulent with current sheets and finally settles to a lowest-energy equilibrium state. This 3D problem is adopted for the performance test of GAMER-MHD. The single-GPU performance can reach  $2 \times 10^7$  cell-updates/sec for K20X and is 25 times faster than a single 16-core CPU on the Blue Waters supercomputer. We also demonstrate a parallel efficiency of 70% using 1,024 nodes on Blue Waters.

Linear perturbations of the wave dark matter, or  $\psi$  dark matter ( $\psi$ DM), in the radiation-dominant era are analyzed. We identify four phases of evolution for  $\psi$ DM perturbations. While in late stages after mass oscillation long-wave  $\psi$ DM perturbations are almost identical to cold dark matter (CDM) perturbations except that intermediate-to-short waves that bear no resemblance with those of CDM throughout the whole evolutionary history. We also discuss the axion model with a cosine field potential. The evolution of axion models are almost identical to those of  $\psi$ DM, but three new features are found in the extreme case where the initial axion angle is near the field potential top. A particularly novel new feature is the spectral excess relative to the CDM model in some wave number range, where the excess may be so large that



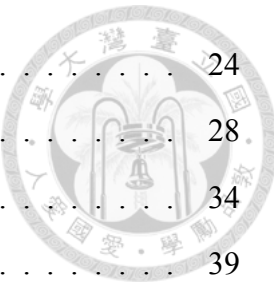
landscapes of high-redshift universe beyond  $z = 10$  can be significantly altered. The sub-horizon perturbations are accurately described by Mathieu's equation and subjected to parametric instability, which explains this novel feature.

Key words: magnetohydrodynamics, graphic-processing-unit, adaptive-mesh-refinement, wave dark matter, radiation-dominant era, axion model.



# Contents

誌謝	v
摘要	vii
<b>Abstract</b>	<b>ix</b>
<b>1 Introduction</b>	<b>1</b>
<b>I MAGNETOHYDRODYNAMICS WITH PARALLEL GRAPHIC-PROCESSING-UNIT-ACCERALATED ADAPTIVE MESH REFINEMENT CODE</b>	<b>3</b>
<b>2 GAMER-MHD</b>	<b>5</b>
<b>3 MHD Equations</b>	<b>9</b>
<b>4 Numerical Algorithm</b>	<b>13</b>
4.1 MHD Scheme . . . . .	13
4.2 Adaptive Mesh Refinement . . . . .	15
4.3 Hybrid MPI/OpenMP/GPUs Parallelization . . . . .	17
<b>5 Numerical Results</b>	<b>19</b>
5.1 Accuracy Test . . . . .	19
5.1.1 Linear Wave Test . . . . .	19
5.1.2 Shock Tube Test . . . . .	20



5.1.3	Orszag and Tang Vortex Test . . . . .	24
5.1.4	Blast Wave Test . . . . .	28
5.1.5	Magnetic field with ABC pattern . . . . .	34
5.2	Performance Test . . . . .	39
5.2.1	GPU Performance . . . . .	39
5.2.2	Overall Performance . . . . .	43
<b>6</b>	<b>Conclusions for Part I</b>	<b>51</b>
<b>II</b>	<b>LINEAR WAVE DARK MATTER PERTURBATIONS</b>	<b>53</b>
<b>7</b>	<b>Brief Review of Wave Dark Matter</b>	<b>55</b>
<b>8</b>	<b>Governing Equations</b>	<b>59</b>
<b>9</b>	<b>Free Particle Model</b>	<b>63</b>
9.1	Passive Evolution and Asymptotic Solutions . . . . .	63
9.1.1	Phase (i): After mass oscillation $2H, k \ll ma$ . . . . .	64
9.1.2	Phase (ii): Before mass oscillation . . . . .	70
9.2	Evolution of Perturbations in Full Treatment . . . . .	72
9.2.1	Neutrino Decoupling . . . . .	73
9.2.2	Photon Fluid Equation of State . . . . .	73
9.2.3	Baryon-Photon Drag . . . . .	74
9.2.4	Matter Self-Gravity . . . . .	75
9.3	Critical Mode, Matter Power Spectrum and Sub-Horizon Dynamics . . .	76
9.4	Adiabatic Perturbations for Superhorizon Modes . . . . .	81
<b>10</b>	<b>Axion Model</b>	<b>83</b>
10.1	Abrupt Growth of $\delta\theta$ . . . . .	86
10.2	Parametric Instability . . . . .	88
10.3	Numerical Solution and General Nonlinear Model . . . . .	94



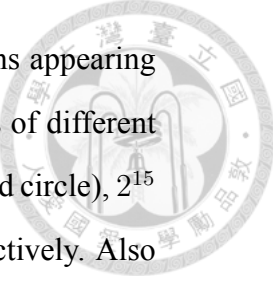
<b>11 Conclusions for Part II</b>	
<b>12 Discussion and Perspective</b>	
<b>A Linear Stability Analysis of the ABC Magnetic Field Configuration</b>	<b>105</b>
<b>B Passive Evolution</b>	<b>115</b>
<b>C Full Treatment Evolution</b>	<b>131</b>
<b>D Particle Mass Dependence</b>	<b>137</b>
<b>E General Dispersion Relation</b>	<b>141</b>
<b>Bibliography</b>	<b>145</b>



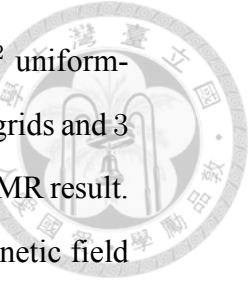


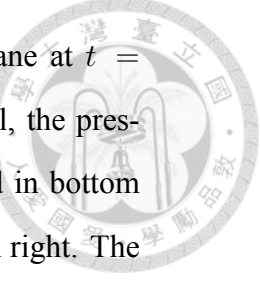
# List of Figures

4.1	Schematic diagram for the locations of conserved variables, fluxes, the magnetic and the electric fields. . . . .	14
4.2	Schematic diagram for the refinement operation acting on the magnetic field in the two-dimensional case. . . . .	16
4.3	Schematic diagram of the hybrid MPI/OpenMP/GPUs parallelization in GAMER. . . . .	18
5.1	The L1-Error plot for the slow, Alfvén and fast wave. Noted that these errors follow the inverse square of the number cells, implying a second order accuracy. . . . .	20
5.2	Density, pressure, velocity components, transverse component of the magnetic field, and rotational angle $\Phi \equiv \tan^{-1}(B_z/B_y)$ for the RJ2a problem at $t = 0.2$ . The simulating setup has 512 uniform grids, PPM data reconstruction and Roe Solver. Also plotted with solid line here is the exact regular solution (Torrilhon, 2002). . . . .	22
5.3	Density, pressure, velocity components, transverse component of the magnetic field, and rotational angle $\Phi \equiv \tan^{-1}(B_z/B_y)$ for the Torrilhon problem at $t = 0.08$ . The simulating setup is the same with RJ2a test. Also plotted with solid line here is the exact regular solution (Torrilhon, 2002). . . . .	23

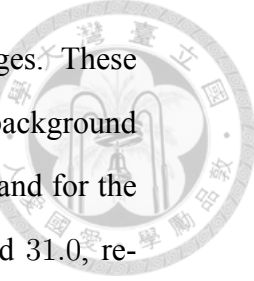


- 5.4 Converging test for Torrihon problem at  $t = 0.08$ . Notations appearing in this figure are the same with Fig. (5.3). Four simulations of different resolutions are shown and they are  $2^9$  (filled square),  $2^{12}$  (filled circle),  $2^{15}$  (filled triangle) and  $2^{18}$  (filled diamond) uniform grids, respectively. Also plotted here is the exact regular solution (Torrilhon, 2002). The numerical solution is seen to slowly approach the exact solution as the resolution increases. . . . . 24
- 5.5 L1-error for Torrihon problem at  $t = 0.08$ . Notations appearing in this figure are the same with Fig. (5.3). The slow convergent rate can be fitted by the power law with a power index  $-3/4$ . . . . . 25
- 5.6 The  $xy$  images at  $t = 0.5L/C_s$ . The left column is the  $1024^2$  uniform-grid result and the middle column is AMR with  $256^2$  base level grids and 3 refinement levels. The right column is zoom-in images of the AMR result. The two rows present the density (normalized by  $\rho_0$ ) and pressure (normalized by  $P_0$ ) from up to bottom, respectively. The color stands for the magnitude. On the other hand, patch structures of AMR results are also shown with the square stands for one patch. (consisting of  $8^3$  cells here). The AMR result agrees with the uniform case. . . . . 26





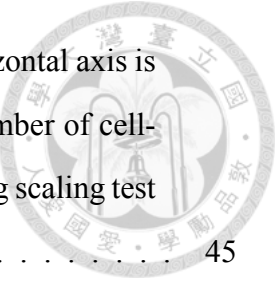
- 5.10 The profile of a line to the box center on the equatorial plane at  $t = 6r_0/C_A$ . The four panels are the density in the top left panel, the pressure in top right, the transverse component of magnetic field in bottom left, and the normal component of the velocity field in bottom right. The normal component of the magnetic field and the transverse component of the velocity field are almost zero. The shock are captured by 1 to 2 cells and the contact discontinuity by 4 – 5 cells. Oscillation of the contact discontinuity emit waves, which are steepen to become shocks behind the strongest shock. All shocks are fast shocks. . . . . 31
- 5.11 The profile along the symmetric axis at  $t = 6r_0/C_A$ . The four panels are same as Fig. (5.10), except for  $B_n$  replacing  $B_T$ . The contact discontinuity is located at  $r = \pm 5.4r_0$  and mixed with the rarefaction wave. The shock is located at  $r = \pm 7.2r_0$ , a slow shock. . . . . 32
- 5.12 The pressure slices (normalized by  $B_0^2$ ) for two different orientations of ambient magnetic fields, which are oriented to  $(\theta, \phi) = (\pi/4, 17\pi/36)$  for the right and  $(\theta, \phi) = (\pi/4, \tan^{-1}(\sqrt{2}))$  for the left at  $t = 0.5r_0/C_A$ . The box size is the same with the size of the zoom-in image in Fig. (5.9). The initial density perturbation is given by Eq. (5.2). Small structures are similar for the two, except for the resolved ringing pattern in the lower middle region of the right panel that is not resolved in the left panel. . . . . 34
- 5.13 The 3D image of the current density magnitude normalized by  $\sqrt{P_0}/L$  at  $t = 1.3L/C_s$  (upper row) and  $t = 2.0L/C_s$  (lower row) with two different viewing angles. The domain of these images is  $[L/4, 5L/8] \times [0, 3L/8] \times [0, 5L/16]$  in the rest frame in which the background uniform flow becomes zero. Current sheets are produced shortly before  $t = 1.3L/C_s$  and two adjacent current sheets tend to merge together at  $t = 2.0L/C_s$ . The strongest current densities are distributed over several patches on the thin sheets. . . . . 38



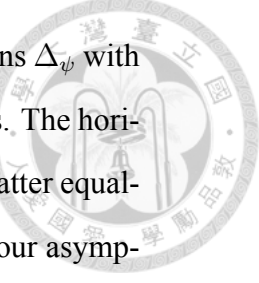
- 5.14 The time sequence of magnetic field magnitude  $xz$  slice images. These images are drawn at  $y = 0.77L$  in the rest frame in which the background uniform flow becomes zero. Numbers labeled in the figure stand for the chronological order and they are at  $t = 0, 3.9, 7.7, 15.5$  and  $31.0$ , respectively. Here time is normalized by  $L/C_s$ . The color stands for the magnetic magnitude. The rightest bottom image is constructed by Eq. (5.7), which is the one-period ABC-flow pattern configuration. The reconstructing image agrees with the  $5-th$  image very well, and the system converges to a stable state. . . . . 40

- 5.15 The evolution of the total energy ( $E_T$  with the dash-dotted line), the magnetic energy ( $U_B$  with the dashed line), the flow energy ( $U_V$  with the dotted line) and the magnetic helicity ( $H$  with the solid line). The horizontal axis is the time normalized to the sound crossing time ( $t_{cross} = L/C_s$ ). The total, magnetic energy and helicity are normalized to their corresponding initial values while the flow energy is normalized to  $U_B(0)/10$  with the initial magnetic energy  $U_B(0)$  for comparison. The total energy remains the same due to the finite-volume method. The magnetic energy decreases while the flow energy first increases and then oscillates. However, the flow energy decreases to zero in the end. Finally, our scheme maintains the magnetic helicity at least 98% up to 32 sound crossing time. This figure shows the consistency with Taylor's conjecture (Taylor, 1986). 41

- 5.16 The number of cell-updates per second versus total simulation cells. We use two different sizes of the patch ( $8^3$  cells for dashed lines and  $16^3$  cells for solid lines) to measure the performance of two different GPUs, Tesla P100 (blue lines) and Tesla K20X (red lines). We also plot the CPU performance under the same coding structure for the numerical scheme. The speed up ratio (GPU performance over CPU one ) is at least 25. . . . . 42



- 5.17 The overall performance for the strong scaling test. The horizontal axis is the number of computing nodes. The vertical axis is the number of cell-updates in one second. Filled circle points is GAMER's strong scaling test result and the dashed line is the ideal scaling. . . . . 45
- 5.18 The quantitative analysis of the strong scaling test for GAMER application. The horizontal axis is the number of Blue water computing nodes. Four panels show different quantities and they are (1) wall-clock time in the left top panel, (2) memory per node in the right top panel, (3) parallel efficiency in the left bottom panel, and (4) doubling efficiency in the right bottom panel. Definitions of these quantities are in the main text. There are 70% parallel efficiency and 78% doubling efficiency up to  $10^3$  computing nodes. . . . . 46
- 5.19 The overall performance for the weak scaling test. The horizontal and vertical axes are the same with Fig. (5.17). Filled circle points are the uniform application results and Filled diamond points are the AMR application. The dashed line is the ideal scaling. . . . . 48
- 5.20 The quantitative analysis of weak scaling test for GAMER application. There are four panels in this figure and they are (1) performance per node (number of cells updated per second per node) in the left top panel, (2) total number of cells in the right top panel, (3) parallel efficiency in the left bottom panel, and (4) MPI time fraction in the right bottom panel. The AMR case has better parallel efficiency than the uniform one which is consistent with the MPI time fraction result. . . . . 49



9.1 Two cases of gauge covariant $\psi$ DM energy density perturbations $\Delta_\psi$ with passive evolution for the very long and very short wave modes. The horizontal axis is $a/a_{eq}$ where $a_{eq}$ is the scale factor at radiation-matter equality, and the particle mass is chosen to be $10^{-22}$ eV. There are four asymptotic phases as labeled. The vertical line marks the beginning of mass oscillation. The bold lines have log-slopes 6, 2, $\sim 0$ , respectively from left to right. . . . .	65
9.2 Passive evolution and full treatment of gauge covariant $\psi$ DM energy density perturbations for several different $k$ 's. The full treatments (dotted lines) deviate from the passive evolution (solid lines) only near the epoch of radiation-matter equality except for very high- $k$ modes, as explained in the text. . . . .	76
9.3 The $\psi$ DM transfer function relative to CDM evaluated at $a_{eq}$ and $2.5a_{eq}$ . The horizontal axis is the wavenumber normalized to $k_c$ . The solid line is for the passive evolution and the dashed line for the full treatment evaluated at $a_{eq}$ . The dotted line is the full treatment evaluated at $2.5a_{eq}$ where the plasma is still fully ionized. The particle mass is the same with Fig. (9.1). We see the passive evolution and the full treatment makes very little difference for $k < 0.4k_c$ , and both follow the CDM power spectrum closely. But for $k > 0.4k_c$ , the two begin to have noticeable differences, due primarily to slightly different frequencies in the matter-wave oscillation. The transfer function for the full treatment at $a = a_{eq}$ also has little difference from that at $a = 2.5a_{eq}$ for $k < k_c$ . Above $k_c$ , the wave function oscillates during this period. The bold line is the analytical fitting formula given by Hu et al. (2000) evaluated at the present, where further short-wave suppression well after $a = a_{eq}$ is clearly seen. . . . .	78

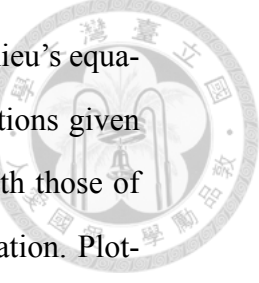
9.4 Phases of wave functions,  $\Re[\hat{\psi}]/|\hat{\psi}|$  and  $\Im[\hat{\psi}]/|\hat{\psi}|$ , evaluated at  $a = a_{eq}$  and  $a = 2.5a_{eq}$  as functions of  $k$ , and obtained by the full treatment. This plot also allows one to narrow down the value of Jeans length during this period as explained in the main text. . . . .

81

### 10.1 Full treatments of the axion model with three different initial angles $\theta_0$ .

The dotted line represents  $\theta_0 \ll 1$  (free-particle model), the dashed line  $\theta_0 = \pi/2$  and the solid line  $\theta_0 = 179\pi/180$ . We also plot three different wavenumbers,  $k \ll k_c$ ,  $k = 0.5k_c$  and  $k = k_c$ , for the above three  $\theta_0$ . For  $k \ll k_c$ , the initial angle  $\theta_0$  does not make any difference in covariant energy density perturbations  $\Delta_\theta$ . For  $k = 0.5k_c$ , some differences appear, particularly for the  $\theta_0 = 179\pi/180$  case, which has a higher amplitude. For  $k = k_c$ , the  $\theta_0 = 179\pi/180$  case becomes very different from the other two cases. For all three  $k$ 's, the  $\theta_0 \ll 1$  and  $\theta_0 = \pi/2$  cases have similar  $\Delta_\theta$ , indicative of that  $\Delta_\theta$  is insensitive to  $\theta_0$ , unless  $\theta_0$  assumes an extreme value very close to  $\pi$ . We also plot the short wavelength case ( $k = 10k_c$ ) for  $\theta_0 = 179\pi/180$  with the orange solid line and CDM model for  $k = k_c$ ,  $0.5k_c$  and  $0.1k_c$  with black solid lines to demonstrate three peculiar features of the extreme axion model. The background energy density  $\varepsilon_\theta$  which is normalized by  $(1/2)(\Omega_{DM}/(\Omega_{DM} + \Omega_b))\varepsilon_t^{eq} \times 10^{12}$  for the axion model with corresponding different initial angles  $\theta_0$  are also plotted with dot-dashed lines. Here  $\varepsilon_t^{eq}$  is the total energy density at the equality. The axion decay constant  $4\pi G f^2$  is  $4.64 \times 10^{-4}$  and  $1.71 \times 10^{-5}$  for  $\theta_0 = \pi/2$  and  $179\pi/180$ , respectively. . . . .

85



10.2 Comparison of $\Delta_\theta$ 's constructed from passive evolution, Mathieu's equation, Eq. (10.8) and the fluid equation, Eq. (D.1). The solutions given by Mathieu's equation and fluid equation agree very well with those of passive evolution long after the onset of nonlinear mass oscillation. Plotted here are also solutions of passive evolution for another nonlinear scalar field model with a potential $\propto 1 - \text{sech}(x)$ and of the corresponding Mathieu's equation and fluid equation for comparison, and excellent agreement is also found. Black lines are passive CDM perturbations for $k = 0.6$ and $1.2k_c$ . Particle mass $m = 10^{-22}$ eV is assumed. . . . .	95
10.3 Transfer functions of the extreme axion model of $m = 10^{-22}$ eV with different initial angles at $a_{eq}$ , $2.5a_{eq}$ and $5a_{eq}$ . Note that the quantity $k_{peak}$ is almost frozen ever since $a = a_{eq}$ . The three initial angles correspond to the axion field strengths, $4\pi Gf^2 = 1.71, 1.13, 0.821 \times 10^{-5}$ from large to small $\delta\theta_0$ . . . . .	97
C.1 The envelopes of gauge covariant photon and baryon energy density perturbations solved by Eq. (C.17) (thick line) and full treatment equations (thin line) for two distinct wavenumbers. Solutions of Eq. (C.17) well agrees with those of the full treatment. Noted that damping for short wavelength modes is controlled by $(\epsilon_b/\epsilon_{ph})k^2l_T/H$ , while damping for long wave modes is $k$ -independent. . . . .	135





# List of Tables

5.1 Left- and right-states for 1D Riemann Problems . . . . .	21
--	----





# Chapter 1

## Introduction

More and more phenomena in Astrophysics and Cosmology are governed by complicated equations. This complexity makes it impossible to find analytical solutions for governing equations. Fortunately, numerical calculations provide approximated solutions and give some quick insights for the physical process. In Astrophysics, the most important equation is magnetohydrodynamics (MHD) model, which describes the evolutionary process for many of astrophysical objects, such as the molecular cloud, stars and galaxies and so on. MHD equations satisfy conservation laws, which are usually solved by finite-volume method (Toro, 1999) numerically. Furthermore, the divergence-free method (Gardiner and Stone, 2008) makes the magnetic field maintains the zero-divergence at any time step. On the other hand, the astrophysical evolution involves very wide range of length scale, from A.U. to Kpc scale, for example. Hence, it becomes a main issue how to resolve such kind of different length scales in the numerical calculation accurately and efficiently. Fortunately, a novel code called GAMER, which is Graphic-processing-unit-accelerated Adaptive-MEsh-Refinement astrophysical code, provides the excellent architecture to achieve the above goal. In the first part of this thesis, we will demonstrate how to use GAMER code to solve MHD equations for astrophysical problems.

In Cosmology, the interesting issue is the large scale structure of our universe. One believes the structure is from the dark matter. Dark matter particles attract each other to form the deep gravitational potential well first and this potential well attracts the usual matter to form objects we observed, such as galaxy clusters. In this scenario, how to

find the dark matter power spectrum in different epochs becomes the crucial problem. Although the governing equation may be complicated, the usual way is to find the power spectrum in the linear regime. This approximation can reduce the problem to be governed by system of ordinary differential equations (ODE). Such kind of ODEs are solved by Runge-Kutta methods, especially the fourth-order one (Press et al., 2007). In the second part of this thesis, a novel dark matter candidate, called the wave dark matter or  $\psi$  dark matter ( $\psi$ DM), are explored to find its corresponding power spectrum near the radiation-matter equality epoch and make the comparison to the traditional cold dark matter (CDM).



## Part I

# MAGNETOHYDRODYNAMICS WITH PARALLEL GRAPHIC-PROCESSING-UNIT- ACCERALATED ADAPTIVE MESH REFINEMENT CODE



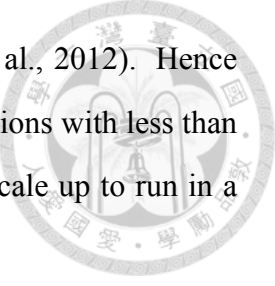


# Chapter 2

## GAMER-MHD

Magnetohydrodynamics (MHD) plays crucial roles in many astrophysical settings, such as dynamo of the primordial magnetic field (Kulsrud and Anderson, 1992; Kulsrud et al., 1997; Naoz and Narayan, 2013; Schober et al., 2013), active galactic nuclei disks (Balbus and Hawley, 1991; Balbus, 2003; Kazanas et al., 2012; Fukumura et al., 2015) and jets (Blandford and Payne, 1982; Pelletier and Pudritz, 1992; Ferreira, 1997; Pudritz et al., 2012; Stepanovs et al., 2014), star forming clouds (Li and McKee, 1996; Balsara et al., 2001; Shu et al., 2004; McKee, 2007). Many of these problems nowadays are often tackled numerically with 3D simulations. However, high-precision 3D simulations are costly. For example, a reasonable research-grade simulation with  $8192^3$  resolution conventionally must run in supercomputers equipped with  $> 100$  nodes.

A new development in the past 10 years has opted in an alternative direction for scientific computing, the graphic-process-unit (GPU) computing. One of the earliest achievements in high-performance computing making good use of GPU's capability is GAMER (Schive et al., 2010, 2012), which is a 3D hydrodynamic (HD) code. It takes advantage of GPU acceleration for number crunching. GAMER differs from other pure GPU codes, in that it also make good use of the central-processing-unit (CPU). Operations other than number crunching in GAMER, such as mesh refinements, data preparation, data transfer among different nodes, Hilbert curve construction, etc., are conducted in the much more versatile, but slower, CPU. As GPU and CPU computing tasks are performed parallel, concurrency of the two is a strong indicator of performance, and GAMER-HD can of-



ten achieve more than 90% concurrency in different tests (Schive et al., 2012). Hence GAMER-HD allows one to efficiently conduct research-grade simulations with less than a dozen of computing nodes. Not only that, GAMER-HD can also scale up to run in a supercomputer with thousands of nodes.

This work extends GAMER-HD into MHD. We closely follow the GAMER data structure and communication techniques. One of the two major new undertakings of GAMER-MHD is the MHD solver with GPU. The MHD solver we adopted follows a well-known CPU-based, MHD simulation code, Athena (Stone et al., 2008). The numerical algorithms in Athena are corner-transport-upwind (CTU) (Colella, 1990) and predictor-corrector (Falle, 1991) methods, both of which are directionally unsplit, higher order Godunov schemes, with the former more accurate than the latter, and hence CTU will be used for comparison. We implement CTU in the GAMER-MHD GPU solver and also adopt the constraint transport (CT) technique to solve the induction equation, a technique that preserves the divergence-free property of the magnetic field (Gardiner and Stone, 2008).

One important feature of GAMER is the AMR, adaptive mesh refinement, which allows one to increase the resolution in regions of interest dynamically. The AMR structure is based on constructing a hierarchy of grid patches with an octree data structure similar to the FLASH code (Fryxell et al., 2000), another well-known HD code. However, implementing the divergence-free constraint on the magnetic field in AMR is non-trivial. Fortunately, Balsara (2001) has proposed a novel method to reinforce the divergence-free constraint on the magnetic field in the AMR computation. This method proposes a scheme to interpolate the fine grid data from the coarse grid data that preserves the zero-divergence of the magnetic field. Therefore, implementation of Balsara's method into the GAMER code for the AMR structure is another new undertaking.

Taking advantage of the AMR strategy, we can apply sufficient resolution to examine standard test problems. Here we choose linear waves, two shock-tube problems (Toro (2003) and Ryu and Jones (1995)), Orszag and Tang (1979) vortex and the blast wave (Londrillo and Zanna, 2000) as our test problems. With sufficiently high resolution, we discover interesting features produced in these tests not reported before. These new

features should be understood via appropriate underlying physical mechanisms and are warranted for separate detailed studies. In this paper, we will only show robust numerical results and leave the comprehensive analyses in future works.

Inspired by the intriguing flow structure of the Arnold-Beltrami-Childress (ABC) flow (Arnold, 1965; Childress, 1970), we investigate a ABC magnetic-field configuration where the 3D incompressible flow is replaced by the 3D divergent-free magnetic field in a uniform plasma. The magnetic field configuration is in force-free equilibrium and the ABC field pattern is controlled by an integer number which determines how many periods appearing in a given box. The two-period configuration are chosen for investigation, as the one-period configuration is shown in this work to be linearly stable. The simulation result reveals that the strong current density takes place in sheets, and the two-period configuration is relaxed to the one-period force-free equilibrium, in agreement with the Taylor's conjecture. This 3D problem is also used for the performance test.

This part is organized as follows. The MHD equations are introduced in Chapter 3. In chapter 4 we present the MHD solver scheme and the AMR structure. In Chapter 4.3 the GAMER MHD structure are described, including the speed-up strategy used in GAMER. In Chapter 5 we show some numerical results including accuracy tests and performance tests. Conclusions are made in Chapter 6. Finally, the proof of the stability of the ABC-flow magnetic field configuration is presented in Appendix A.





# Chapter 3

## MHD Equations

The equations for MHD can be written in conservative form as

$$\frac{\partial \rho}{\partial t} + \nabla \cdot (\rho \mathbf{V}) = 0, \quad (3.1)$$

$$\frac{\partial \rho \mathbf{V}}{\partial t} + \nabla \cdot (\rho \mathbf{V} \mathbf{V} - \mathbf{B} \mathbf{B} + P^*) = \mathbf{0}, \quad (3.2)$$

$$\frac{\partial e}{\partial t} + \nabla \cdot [(e + P^*) \mathbf{V} - \mathbf{B}(\mathbf{B} \cdot \mathbf{V})] = 0, \quad (3.3)$$

$$\frac{\partial \mathbf{B}}{\partial t} + \nabla \times \mathbf{E} = \mathbf{0}. \quad (3.4)$$

where  $P^* = P + \mathbf{B} \cdot \mathbf{B}/2$  with the gas pressure  $P$ ,  $\mathbf{E} = -\mathbf{V} \times \mathbf{B}$  is the electric field and  $e$  is the total energy density

$$e = \frac{P}{\gamma - 1} + \frac{1}{2}\rho \mathbf{V} \cdot \mathbf{V} + \frac{\mathbf{B} \cdot \mathbf{B}}{2}. \quad (3.5)$$

Other symbols have their usual meanings. These equations are written in units such that the magnetic permeability  $\mu = 1$  and the speed of light  $c = 1$ .

In addition to these equations, the magnetic field must obey the divergence-free constraint, i.e.  $\nabla \cdot \mathbf{B} = 0$ .

The above equations can be rewritten as  $\partial_t \mathbf{U} + \partial_x \mathbf{F}_x + \partial_y \mathbf{F}_y + \partial_z \mathbf{F}_z = \mathbf{0}$  in Cartesian coordinate. Here  $\mathbf{U}$  is the vector of conserved densities with the following form

$$\mathbf{U} = \begin{bmatrix} \rho \\ M_x \\ M_y \\ M_z \\ e \\ B_x \\ B_y \\ B_z \end{bmatrix}, \quad (3.6)$$

where  $\mathbf{M} = (M_x, M_y, M_z) \equiv \rho \mathbf{V}$  is the momentum density.  $\mathbf{F}_x$ ,  $\mathbf{F}_y$  and  $\mathbf{F}_z$  are components of a vector of fluxes in the  $x$ -,  $y$ - and  $z$ -directions, respectively, and they are

$$\mathbf{F}_x = \begin{bmatrix} \rho V_x \\ \rho V_x^2 + P + \frac{1}{2}(\mathbf{B} \cdot \mathbf{B}) - B_x^2 \\ \rho V_x V_y - B_x B_y \\ \rho V_x V_z - B_x B_z \\ (e + P^*) V_x - (\mathbf{B} \cdot \mathbf{V}) B_x \\ 0 \\ B_y V_x - B_x V_y \\ B_z V_x - B_x V_z \end{bmatrix}, \quad (3.7)$$



$$\mathbf{F}_y = \begin{bmatrix} \rho V_y \\ \rho V_y V_x - B_y B_x \\ \rho V_y^2 + P + \frac{1}{2}(\mathbf{B} \cdot \mathbf{B}) - B_y^2 \\ \rho V_y V_z - B_y B_z \\ (e + P^*)V_y - (\mathbf{B} \cdot \mathbf{V})By \\ B_x V_y - B_y V_x \\ 0 \\ B_z V_y - B_y V_z \end{bmatrix}, \quad (3.8)$$

$$\mathbf{F}_z = \begin{bmatrix} \rho V_z \\ \rho V_z V_x - B_z B_x \\ \rho V_z V_y - B_z B_y \\ \rho V_z^2 + P + \frac{1}{2}(\mathbf{B} \cdot \mathbf{B}) - B_z^2 \\ (e + P^*)V_z - (\mathbf{B} \cdot \mathbf{V})Bz \\ B_x V_z - B_z V_x \\ B_y V_z - B_z V_y \\ 0 \end{bmatrix}. \quad (3.9)$$





# Chapter 4

## Numerical Algorithm

In this section, we describe the MHD algorithm and the AMR scheme implemented in GAMER-MHD.

### 4.1 MHD Scheme

The conservative MHD equations given in Chapter 3 is usually solved by the finite-volume method, in which conserved densities are treated as the volume-averaged quantities in a given cubic cell and evolved by fluxes defined on the cell interfaces. The CTU scheme, for instance, is a scheme based on this method. On the other hand, to preserve the divergence-free constraint on the magnetic field, the CT technique proposes that the magnetic field should be treated as the area-averaged quantity on the cell interface and it is evolved by the electric fields defined on the edges of the cubic cell, as illustrating in Fig. (4.1). Thus pure fluid variables, such as mass density, momentum density and energy density, are separated from the magnetic field in the way each is evolved. Unless otherwise noted, "conserved variables" will refer to the former.

In this work, we have implemented the CTU scheme with CT technique into GAMER. We summarize the procedures in CTU for updating the solution by one time step  $\Delta t$ , which is determined by the Courant-Friedrichs-Lowy stability condition (Courant et al., 1928). For more details of this scheme, the readers are referred to Stone et al. (2008).

1. Evaluate the left and right interface values for all cells in all three spatial directions

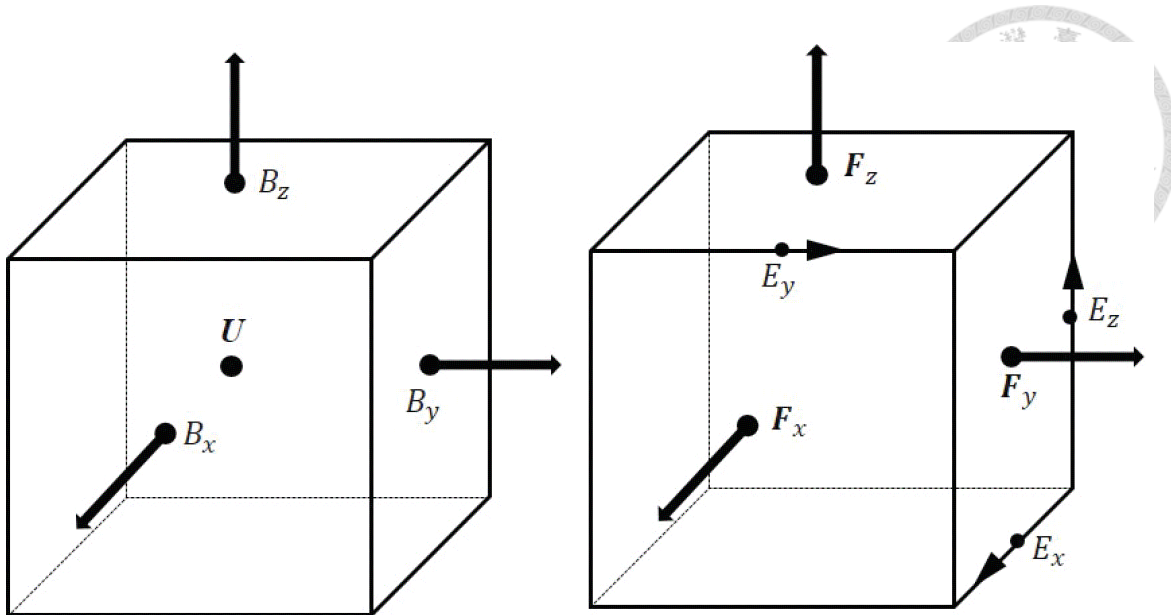


Figure 4.1: Schematic diagram for the locations of conserved variables, fluxes, the magnetic and the electric fields.

by the 1D data reconstruction. GAMER-MHD supports both the piece-wise linear (PLM) and piece-wise parabolic (PPM) interpolations.

2. Evaluate the fluxes across all cell interfaces by solving the Riemann problem. Here the electric field is defined at the cell interface. GAMER-MHD supports three Riemann solvers: HLLE, HLLD and Roe solvers.

3. Evaluate the electric field on the cell edge from the electric field at the cell interface obtained by step 2 together with the magnetic field at the cell interface and the velocity at the cell center.

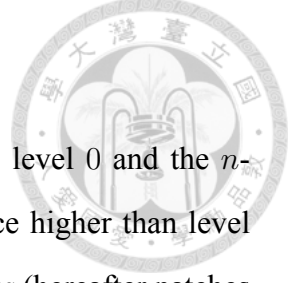
4. Update the area-averaged magnetic field using CT and all volume-averaged conserved variables by  $\Delta t/2$  by the conservative integration.

5. Correct the cell interface value obtained in step 1 by computing the transverse flux gradients.

6. Solve the Riemann problem with the corrected data to obtain the new fluxes across all cell interfaces.

7. Evaluate the fully updated electric field on the cell edge again with the electric field obtained by step 6 and the half-step magnetic field and velocity from step 4.

8. Update all conserved variables and magnetic field by  $\Delta t$ .



## 4.2 Adaptive Mesh Refinement

Following GAMER-HD, we define the base grid resolution as level 0 and the  $n$ -th refinement as level  $n$ , where level  $n$  has a spatial resolution twice higher than level  $n - 1$ . Data in GAMER-HD are always decomposed into *grid patches* (hereafter patches for short), each of which consists of  $N^3$  cells. The AMR implementation is realized by constructing a hierarchy of octree patches structure. The MHD is similar to the HD except for more equations. Two operations are required for updating the AMR data at the moment when the adjacent levels (say, level  $l$  and  $l + 1$ ) are synchronized.

1. *Correction Operation.* At this moment the coarse-grid data might be slightly inconsistent with the fine-grid data since they are evolved independently, and this is a procedure to correct the coarse-grid data by the fine-grid data. Two different situations can arise and the correction procedures are different. First, for a coarse grid overlapping with fine grids, the coarse-grid data are simply replaced by the volume average and area average of the fine-grid data for conserved variables and the magnetic field, respectively. Second, for a leaf coarse grid adjacent to a coarse-fine interface, the flux difference between the coarse and fine grids on the interface will be used to correct the coarse-grid conserved variables adjacent to this interface. A similar procedure is applied on the magnetic field correction where the electric field differences on coarse-fine interedges are used to correct the magnetic field. These corrections are necessary to preserve the conservation law of conserved variables and the divergence-free constraint on the magnetic field.

2. *Refinement/Derefinement Operations.* This is the procedure to create/remove fine grids according to the refinement criteria. In creating new fine grids, we adopt the conservative interpolation for conserved variables and the interpolation method proposed by Balsara (2001) to maintain a divergence-free magnetic field. In the following we use a 2D example to explain the Balsara's method.

Consider a coarse grid that needs to be refined to fine grids as illustrated by Fig. (4.2). There are 12 magnetic field refined values to be determined. We divide these 12 values into two sets. The first set includes those interfacing with the coarse grids (labeled as number (1)-(8)) and the second set includes the interior interfaces (number (9)-(12)). First, values

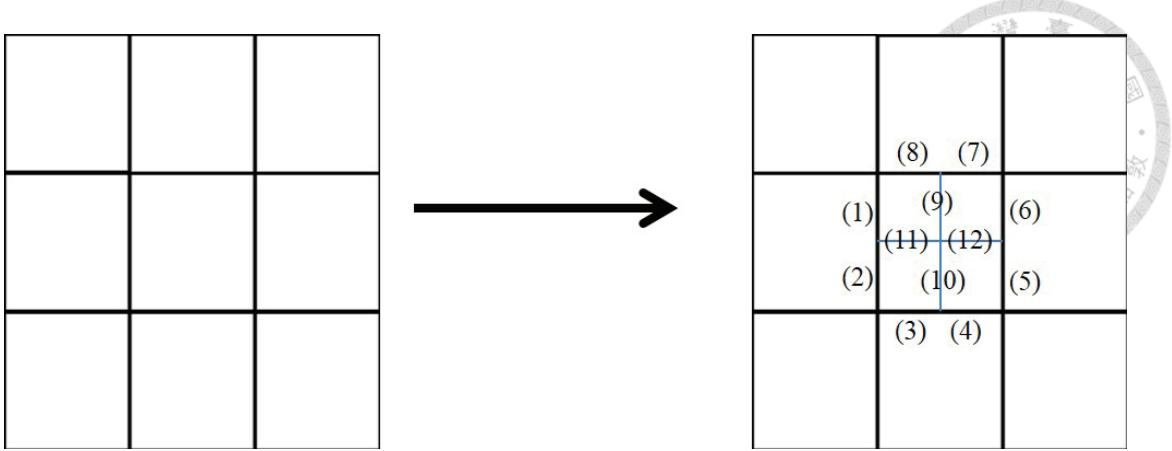


Figure 4.2: Schematic diagram for the refinement operation acting on the magnetic field in the two-dimensional case.

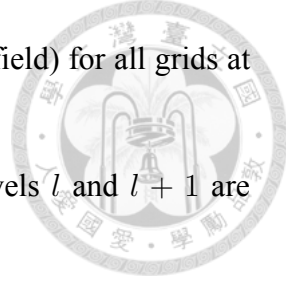
in the first set are determined by the piecewise linear interpolation among nearby coarse grids, which ensures that the average of fine magnetic field values is the same as the coarse value. For determining the second set (the interior part), we Taylor-expand the magnetic field about the coarse grid center,

$$\begin{aligned} B_x(x, y) &= a_0 + a_x x + a_y y + a_{xx} x^2 + a_{xy} x y, \\ B_y(x, y) &= b_0 + b_x x + b_y y + b_{yy} y^2 + b_{xy} x y, \end{aligned} \quad (4.1)$$

with 10 coefficients, whose values are to be determined. Here we ignore  $y^2$  term in  $B_x$  and  $x^2$  in  $B_y$  to fit linear profiles on the coarse grid interface, which is consistent with the piecewise linear interpolation acted on the first set. Moreover, evaluating Eq. (4.1) at the first set (interfaces of the coarse grid) gives eight equations. However, these eight equations are not independent due to the divergence-free constraint on the coarse-grid magnetic field. Hence only seven independent equations remain from the matching values on interfaces. On the other hand, applying the divergence-free constraint on Eq. (4.1) gives  $\partial_x B_x + \partial_y B_y = (a_x + b_y) + (2a_{xx} + b_{xy})x + (a_{xy} + 2b_{yy})y = 0$ . Values in the parentheses should separately be equal to zero and it gives three equations. In the end, we have 10 equations and these coefficients can be uniquely determined. Once fixing the coefficients, interior values can be determined by evaluating Eq. (4.1) at any appropriate position.

The procedure of updating grids at level  $l$  can be summarized as follows.

1. Update all quantities (conserved variables and the magnetic field) for all grids at level  $l$ .
2. Evolve the next refinement level  $l + 1$  until the data at levels  $l$  and  $l + 1$  are synchronized in time.
3. Apply the correction operation to correct quantities at level  $l$ .
4. Apply the refinement/derefinement operations to allocate/deallocate grids at level  $l + 1$  according to the refinement criteria.



### 4.3 Hybrid MPI/OpenMP/GPUs Parallelization

In GAMER, the MHD solver mentioned in Section 4.1 is parallel executed in the GPU. Nearby eight patches are grouped into a single *patch group* (which contains  $(2N)^3$  cells), and each patch group will be computed by one CUDA thread block. Choosing the patch group rather than a single patch as the computing unit can reduce the computational overhead associated with ghost zones due to the smaller surface/volume ratio. On the other hand, AMR operations e.g., the correction and refinement/derefinement operations mentioned in Section 4.2 are executed in CPU because they are much less time-consuming than the MHD solver. It also allows GAMER to store all the simulation data in the CPU memory, which is generally much larger than the GPU global memory, and send only a small number of patch groups (typically a few hundreds) into GPU at a time.

GAMER has implemented several performance optimization strategies which can also be applied to MHD. For example, the *CUDA stream* is used to overlap the MHD solver execution in GPU with the data transfer between CPU and GPU. Concurrent execution between CPU and GPU hides the preparation and closing steps in CPU by GPU execution, where the preparation step is for fetching appropriate data from the octree for the MHD solver to update and the closing step is for storing the newly updated data back to the octree. Furthermore, Open Multi-Processing (OpenMP) is used to parallelize the preparation and closing steps and other AMR operations.

In GAMER, the inter-node parallelization is achieved using Message-Passing-Interface (MPI), and the Hilbert space-filling curve domain decomposition is applied for load bal-

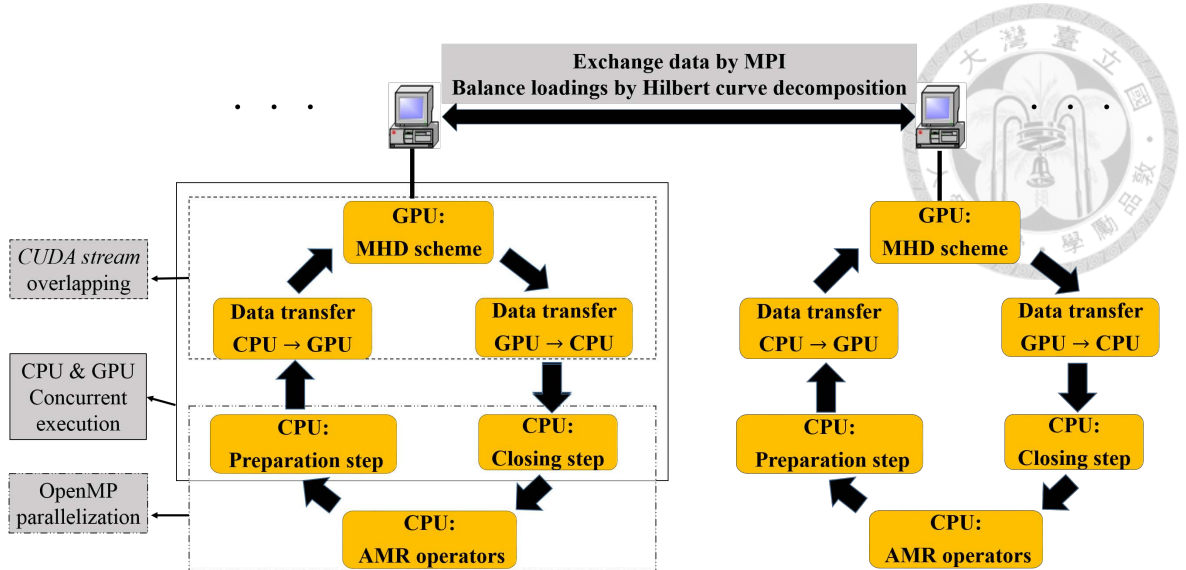


Figure 4.3: Schematic diagram of the hybrid MPI/OpenMP/GPUs parallelization in GAMER.

ance. This hybrid MPI/OpenMP/GPUs implementation allows for exploiting the computing power of multi-node/multi-core CPU/multi-GPUs in heterogeneous supercomputers. Figure (4.3) summarizes the schematics of this hybrid scheme. More details can be found in Schive et al. (2012).



# Chapter 5

## Numerical Results

In this section, we perform two different kinds of tests. The first is accuracy tests which show the correctness of GAMER-MHD code the performance tests that quantify the speed-up and scalability performance. In all tests the adiabatic index  $\gamma$  is chosen to be 5/3, and the Courant number for the Courant-Friedrichs-Lowy stability condition is set to 0.5.

### 5.1 Accuracy Test

#### 5.1.1 Linear Wave Test

There are three types of linear waves, slow, Alfvén and fast waves. In principle, these waves are one-dimensional problem. However, we can make the propagating speed along with the diagonal direction of the simulation box subjected to the periodic boundary for examining the 3D MHD algorithm.

To quantify the accuracy, the traveling wave with the relative amplitude  $10^{-6}$  by uniform grids is performed for one period and the "L1-Error" is measured. Here L1-Error,  $E_{L1}$  for short, is defined as  $E_{L1} \equiv \sum_{i=1}^N |u_i^T - u_i^0|/N$ , where  $N$  is number of cells and  $u$  is primitive variables (density, velocity, pressure and magnetic field). The subscript stands for the grid index and superscript is for temporal label with 0 for the initial time and  $T$  for the one period. Figure (5.1) depicts our results. Here PLM data reconstruction, Roe

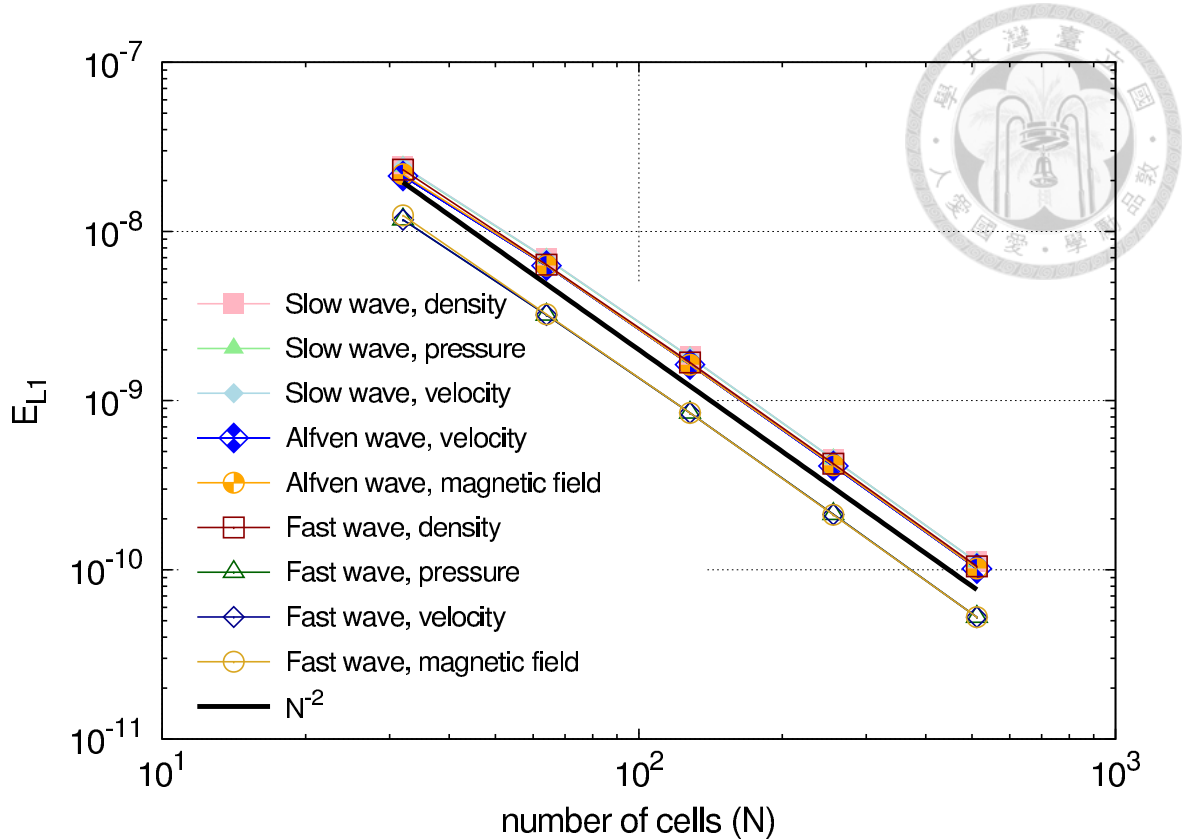


Figure 5.1: The L1-Error plot for the slow, Alfven and fast wave. Noted that these errors follow the inverse square of the number cells, implying a second order accuracy.

Riemann solver and the double precision calculation are adopted in these tests.

From Fig. (5.1), all errors are inversely proportional to the square of the number cells, and it is consistent to the second order accuracy of the CTU scheme with PLM data reconstruction.

### 5.1.2 Shock Tube Test

Shock tube tests are for examining the goodness for representing the nonlinear wave, especially capturing shocks and discontinuities. Such kind of tests can be generated by one dimensional Riemann problems. Without losing of generality, we set the propagating direction along the  $x$ -axis, i.e., all variables depend only on  $x$ . Here we choose the Ryu and Jones (1995) (RJ2a for short) and Torrilhon (2003) Riemann problems for our tests. These two problems are also standard tests in Athena code (Stone et al., 2008). The following table is the initial left and right states for these two tests. Here PPM data reconstruction, Roe Riemann solver and the double precision calculations are adopted for these tests,

Test	$\rho_L$	$V_{x,L}$	$V_{y,L}$	$V_{z,L}$	$P_L$	$B_{y,L}$	$B_{z,L}$	$\rho_R$	$V_{x,R}$	$V_{y,R}$	$V_{z,R}$	$P_R$	$B_{y,R}$	$B_{z,R}$
Torrilhon	1.0	0	0	0	1.0	1.0	0	0.2	0	0	0	0.2	$\cos(3)$	$\sin(3)$
RJ2a	1.08	1.2	0.01	0.5	0.95	$3.6/(4\pi)^{1/2}$	$2/(4\pi)^{1/2}$	1	0	0	0	1	$4/(4\pi)^{1/2}$	$2/(4\pi)^{1/2}$

Table 5.1: Left- and right-states for 1D Riemann Problems

and the boundary condition is Dirichlet type determined by the left and right states. The simulation box length is chosen to be 1.

Figures (5.2) and (5.3) are results. For MHD Riemann problems, the longitudinal magnetic field component ( $B_x$ ) should be specified. Here  $B_x = 2/(4\pi)^{1/2}$  for RJ2a and  $B_x = 1.0$  for Torrilhon. We simulate both cases with 512 uniform grids. All discontinuous waves are captured by 2 – 4 cells, especially shown by the solution of the RJ2a problem where all discontinuities in each MHD wave family are reproduced, i.e., that is left- and right-propagating fast and slow shocks, left- and right-propagating rotational discontinuities and a contact discontinuity. Small overshoot oscillations appear in the velocity and the transverse component of the magnetic field and they can be eliminated by using PLM data reconstruction.

The unphysical compound wave structure is seen in the Torrilhon test near  $x=-0.05$  due to numerical dissipation. This structure can be eliminated by increasing the resolution (Torrilhon, 2003). Due to its intrinsic 1-D problem and our hybrid MPI/OpenMP/GPU parallelization, we can attain a very high resolution uniform-grid simulation along the direction of propagation within a reasonable run time. Figure (5.4) is the result. The strength of the compound wave decreases and the slow shock on the right and the rotational discontinuity on the left are seen to be separated when the resolution becomes very high. Furthermore, we also measure the L1-Error of all quantities. The definition of L1-Error is the same as the linear wave test except for measuring the difference between the numerical and exact solutions. We only focus on the region of the compound wave within  $-0.073 < x < 0.04$  at  $t = 0.08$ , and measure the difference between the numerical solution and the exact solution in that region. Figure (5.5) presents the L1-Error versus the number of cells and the converging rate is much slower than normal second order schemes

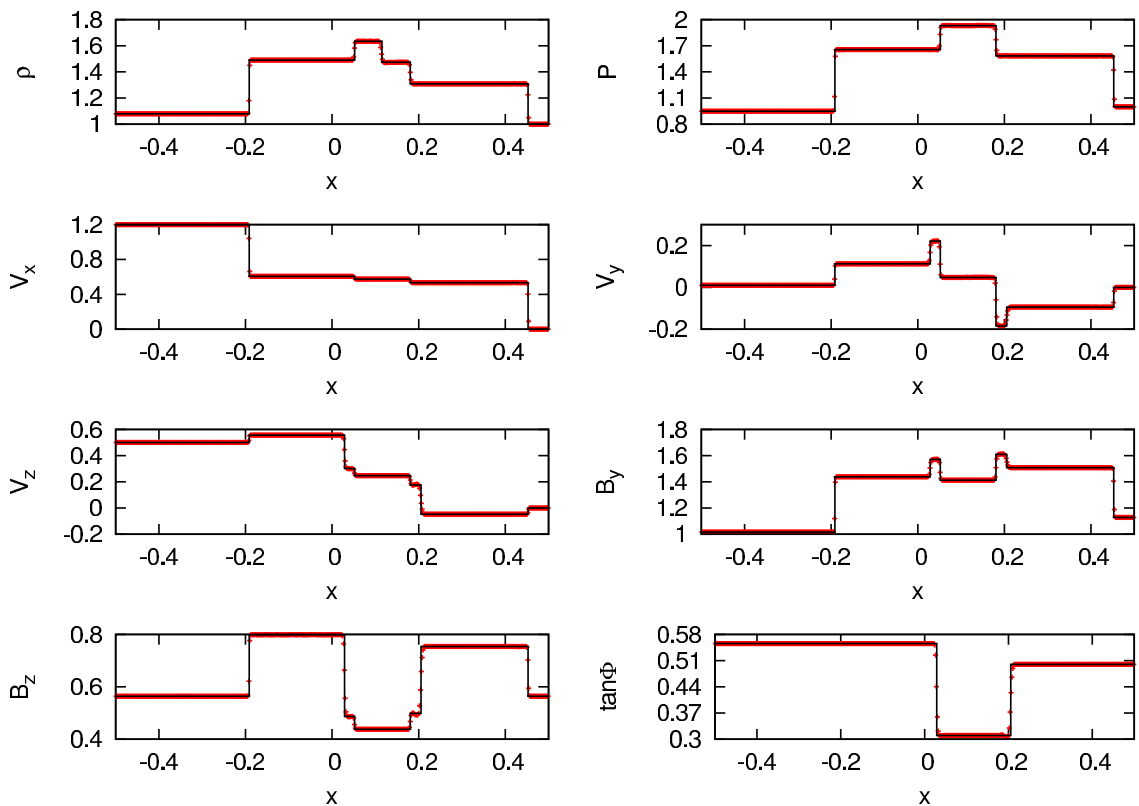


Figure 5.2: Density, pressure, velocity components, transverse component of the magnetic field, and rotational angle  $\Phi \equiv \tan^{-1}(B_z/B_y)$  for the RJ2a problem at  $t = 0.2$ . The simulating setup has 512 uniform grids, PPM data reconstruction and Roe Solver. Also plotted with solid line here is the exact regular solution (Torrilhon, 2002).

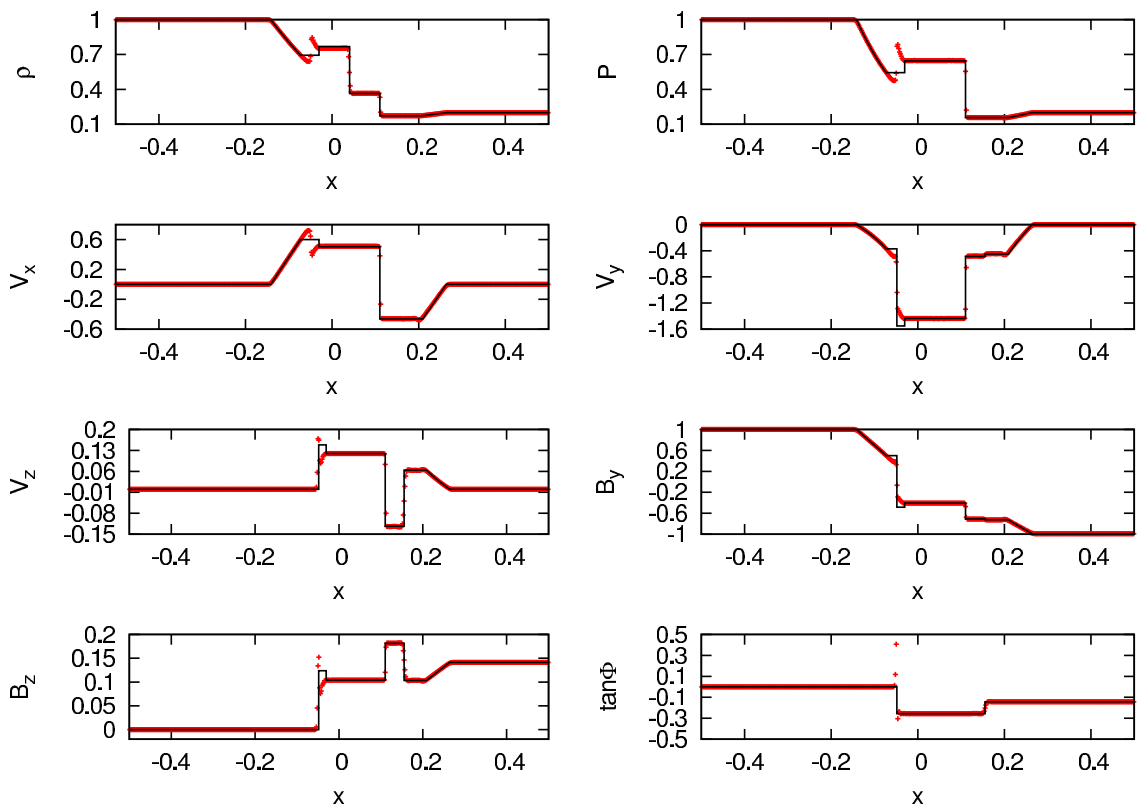


Figure 5.3: Density, pressure, velocity components, transverse component of the magnetic field, and rotational angle  $\Phi \equiv \tan^{-1}(B_z/B_y)$  for the Torrilhon problem at  $t = 0.08$ . The simulating setup is the same with RJ2a test. Also plotted with solid line here is the exact regular solution (Torrilhon, 2002).

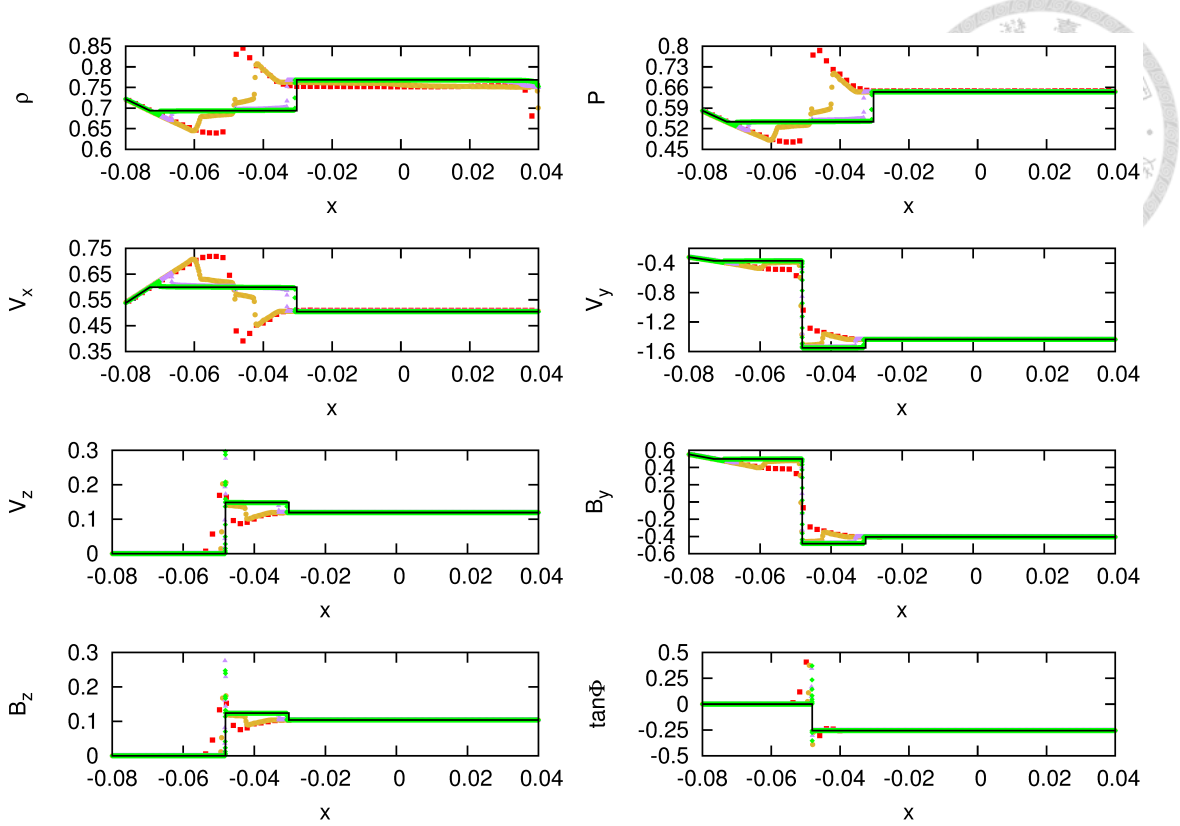


Figure 5.4: Converging test for Torrihon problem at  $t = 0.08$ . Notations appearing in this figure are the same with Fig. (5.3). Four simulations of different resolutions are shown and they are  $2^9$  (filled square),  $2^{12}$  (filled circle),  $2^{15}$  (filled triangle) and  $2^{18}$  (filled diamond) uniform grids, respectively. Also plotted here is the exact regular solution (Torrihon, 2002). The numerical solution is seen to slowly approach the exact solution as the resolution increases.

and can be fitted as the power law with a power index  $-3/4$ .

### 5.1.3 Orszag and Tang Vortex Test

This test was developed by Orszag and Tang (1979). In this test, small-scale structure can be generated via a single large-scale differentially rotating vortex acting on two circular magnetic structures of opposite signs. This is a two dimensional problem, so we start the simulation with a square box subject to the periodic boundary with the side of the box  $L$ . The initial density  $\rho_0$  and pressure  $P_0$  are constants everywhere. The initial velocity and the magnetic field are given by

$$\begin{aligned} \mathbf{V} &= -C_s \sin\left(\frac{2\pi}{L}y\right)\hat{x} + C_s \sin\left(\frac{2\pi}{L}x\right)\hat{y}, \\ \mathbf{B} &= -\sqrt{\frac{P_0}{\gamma}} \sin\left(\frac{2\pi}{L}y\right)\hat{x} + \sqrt{\frac{P_0}{\gamma}} \sin\left(\frac{4\pi}{L}x\right)\hat{y}, \end{aligned} \quad (5.1)$$

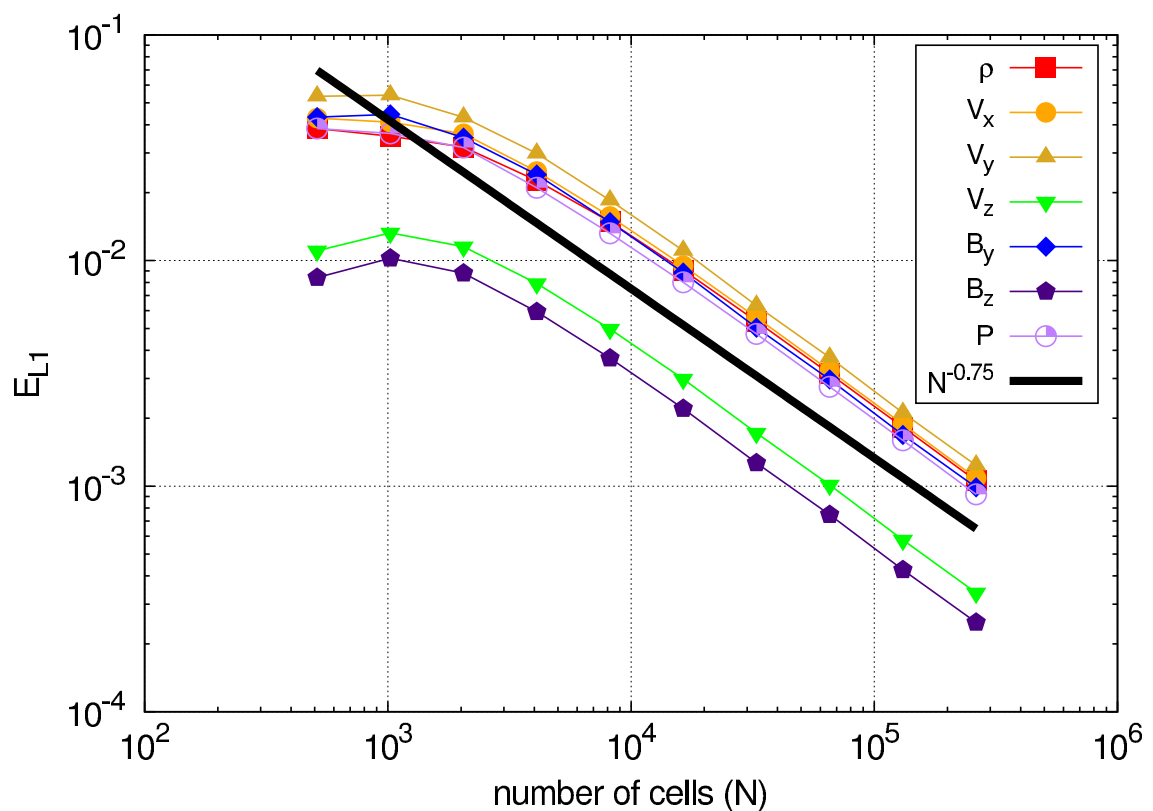


Figure 5.5: L1-error for Torrihon problem at  $t = 0.08$ . Notations appearing in this figure are the same with Fig. (5.3). The slow convergent rate can be fitted by the power law with a power index  $-3/4$ .

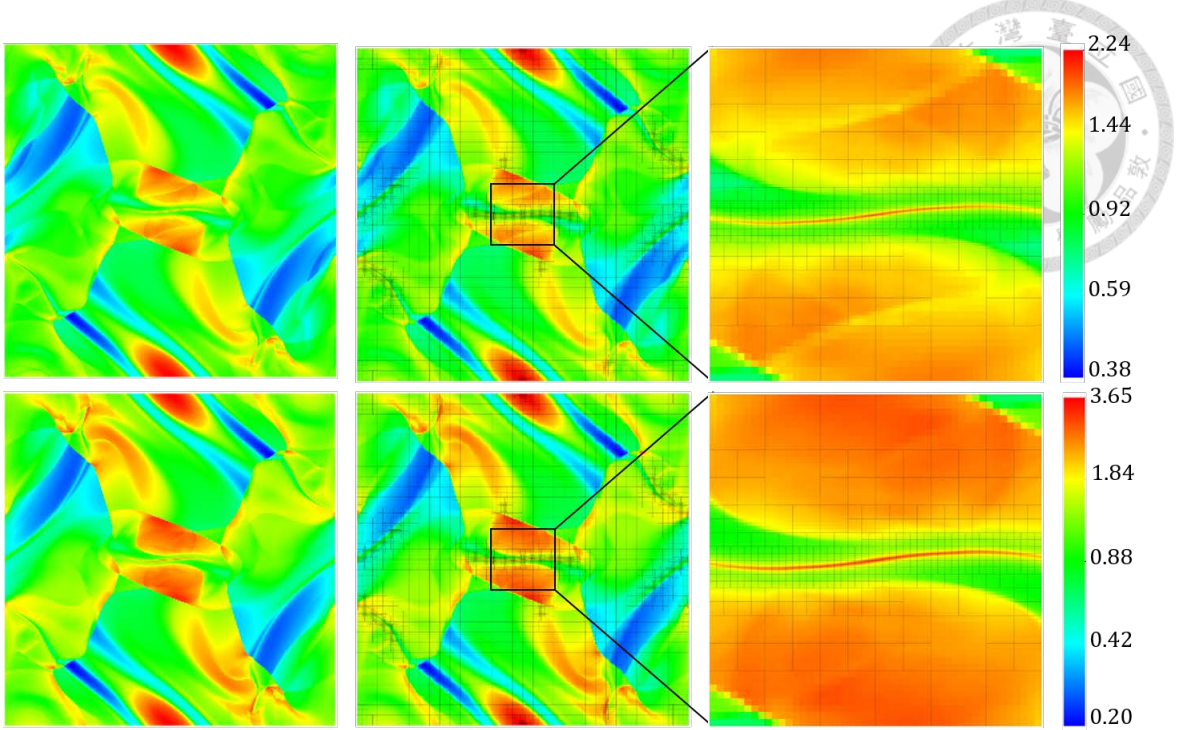


Figure 5.6: The  $xy$  images at  $t = 0.5L/C_s$ . The left column is the  $1024^2$  uniform-grid result and the middle column is AMR with  $256^2$  base level grids and 3 refinement levels. The right column is zoom-in images of the AMR result. The two rows present the density (normalized by  $\rho_0$ ) and pressure (normalized by  $P_0$ ) from up to bottom, respectively. The color stands for the magnitude. On the other hand, patch structures of AMR results are also shown with the square stands for one patch. (consisting of  $8^3$  cells here). The AMR result agrees with the uniform case.

where  $C_s \equiv \sqrt{\gamma P_0 / \rho_0}$  is the sound speed. Finally, the numerical setup (data reconstruction, Riemann solver and computing precision) is the same with shock tube tests. In addition, we turn on AMR.

Figure (5.6) and (5.7) depict the results at  $t = 0.5L/C_s$ . The left columns in Fig. (5.6) and (5.7) are made by the  $1024^2$  uniform-grid simulation and the other two columns by the the AMR simulation with  $256^2$  base level grids with 3 levels of refinement. The uniform-grid simulation has an equivalent resolution to the second refinement level in the AMR simulation. The quantity  $|\mathbf{J}|/|\mathbf{B}|$  is used as the refinement criterion. When the local  $|\mathbf{J}|/|\mathbf{B}| > 3.2/\Delta h(k - 1)$ , the grid is refined to level  $k$  where  $\Delta h(k)$  is the  $k$ -th level grid size. Here we stop the refinement at  $k = 3$ . This criterion aims to capture magnetic reconnection since  $|\mathbf{J}|/|\mathbf{B}|$  is becoming singular at reconnection sites.

Figure (5.6) and (5.7) show good match between the uniform-grid simulation and the AMR one. The quantitative analysis are in Fig. (5.8), in which we measure the ratio

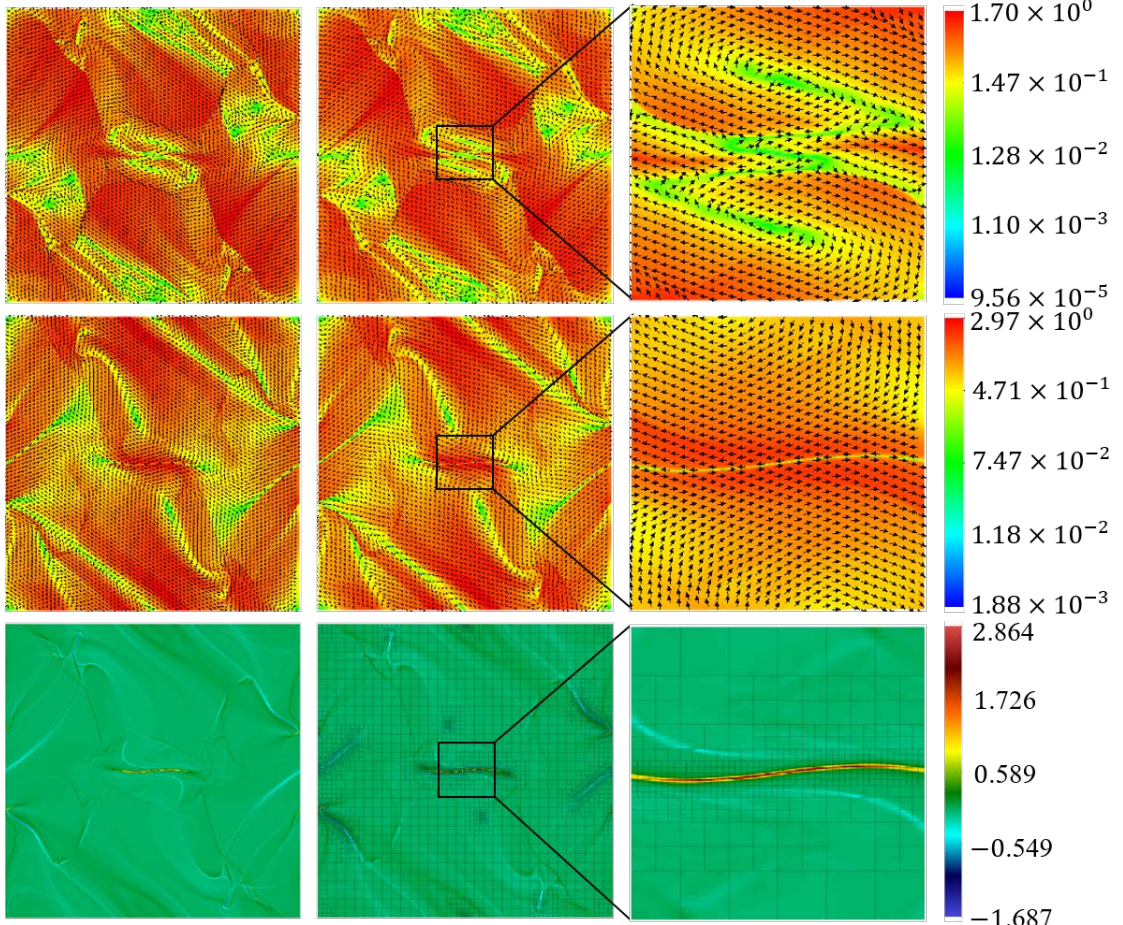


Figure 5.7: The  $xy$  images at  $t = 0.5L/C_s$ . The left column is the  $1024^2$  uniform-grid result and the middle column is AMR with  $256^2$  base level grids and 3 refinement levels. The right column is zoom-in images of the AMR result. The three rows present velocity field (normalized by  $C_s$ ), magnetic field (normalized by  $\sqrt{P_0/\gamma}$ ) and and the z-component of the current density (normalized by  $10^3 \sqrt{P_0/\gamma} / L$ ) from up to bottom, respectively. Note that the x- and y-component of the current density are zeros automatically. The color stands for the magnitude. On the other hand, arrows in velocity and magnetic fields present the directions. Patch structures of AMR results are also shown with the square stands for one patch. (consisting of  $8^3$  cells here). The AMR result agrees with the uniform case and the patch structure captures magnetic reconnection very well, which is found similar to the Sweet-Parker type, with rotational inflow outside the reconnection layer.

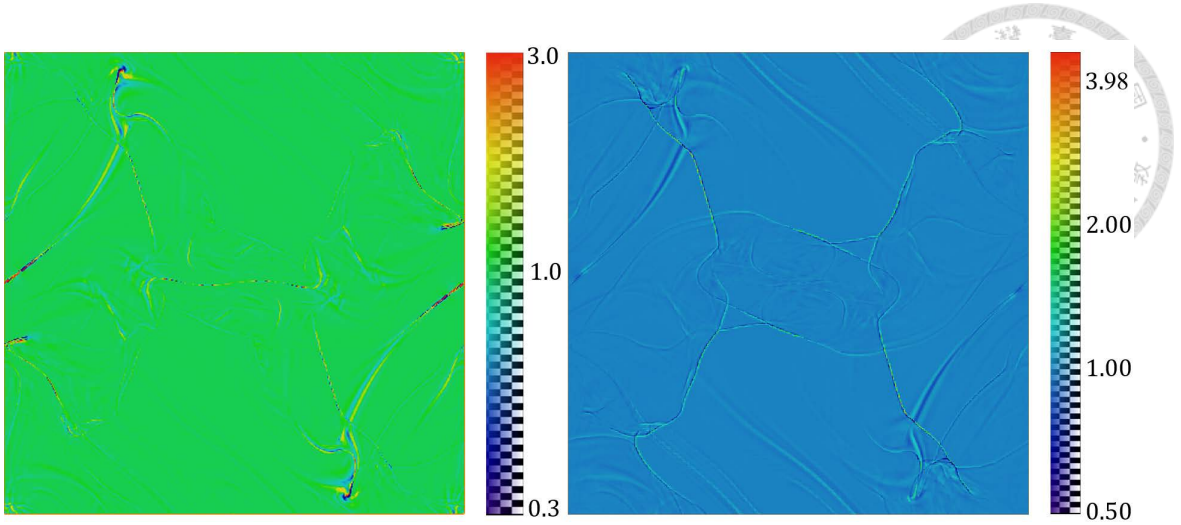


Figure 5.8: The ratio between AMR and uniform-grid simulations for the magnetic pressure (left panel) and the gas pressure (right panel) at  $t = 0.5L/C_s$ . The ratio is almost one throughout the whole domain except for some filamentary regions corresponding to shock and reconnection locations or the magnetic reconnection layer.

between the AMR result and the uniform-grid one for the magnetic pressure and gas pressure. Values in Fig. (5.8) are almost unity except for at shock locations and the magnetic reconnection layer, indicative of good match between the AMR solution and the uniform-grid solution. The patch structures shown in the right columns of Fig. (5.6) and (5.7) illustrate the refinement criterion captures magnetic reconnections quite well. Furthermore, reconnections found in this test appear to be a variant of Sweet-Parker reconnection (Parker, 1957; Sweet, 1958) with two spiral inflows and two horizon jet outflows located near the mid plane as depicted in the zoom-in image in Fig. (5.7). The inflow velocity structure has been modified by the large-scale differential rotation.

### 5.1.4 Blast Wave Test

This test examines the propagation of strong MHD shock in a magnetized plasma. We generalize the initial condition in Londrillo and Zanna (2000) to three dimensional setup, i.e., a uniform, static, spherical plasma with radius  $r_0$ , density  $\rho_0$  and pressure  $P_0$  is surrounded by an ambient one with constant density  $\rho_0$  and pressure  $10^{-2}P_0$ . The magnetic field is uniform everywhere with the strength  $B_0$ . Values of  $r_0$ ,  $\rho_0$ ,  $P_0$  and  $B_0$  we adopt follow Londrillo and Zanna (2000). In particular, the ambient plasma  $\beta = 0.2$  and the maximum fast shock March number  $M \equiv S/\sqrt{C_A^2 + C_s^2} = 2.54$  perpendicular to the



magnetic field, where  $S$  is the fast shock speed,  $C_A$  and  $C_s$  are the upstream Alfvén speed and sound speed, respectively. Numerical setups (data reconstruction, Riemann solver and calculating precision) are the same with Orszag-Tang test. Finally, the simulating domain is a cube with the length  $20r_0$  and the boundary is periodic.

Although the initial setup is three dimensional, this configuration has the rotational symmetry respect to the magnetic field line. Therefore, the initial magnetic field can be any arbitrary direction without changing features of the solution. To illustrate results, we make the magnetic field along with the diagonal direction of  $xy$  plane, i.e.,  $\mathbf{B} = \mathbf{i}B_0/\sqrt{2} + \mathbf{j}B_0/\sqrt{2}$ . Figure (5.9) shows the  $xy$  slice image which cuts through the center of explosion and the blast wave noses at  $t = 6r_0/C_A$ .

In Fig. (5.9), the left column is made with the simulation with uniform  $512^3$  cubic grids and the other two columns with the AMR simulation where the base level has  $256^3$  cubic grids up to 3 refinement levels. The uniform grid simulation has the equivalent resolution to the first refinement level in the AMR simulation. The AMR refinement criterion is as follows. The grid with normalized pressure gradient ( $10^2 r_0 |\nabla P|/P$ ) higher than  $1.25 \times 2^{n-1}$  is refined to level  $n$ . This condition aims to capture the strong shock.

From Fig. (5.9), the AMR simulation agrees with the uniform-grid simulation on the large-scale structure . To see how well our schemes capture three dimensional shocks and discontinuity, we show profiles of lines penetrating through the equator and along the symmetric axis in Figures (5.10) and (5.11), respectively. The profile through the equator reveals shocks are captured by 1 to 2 cells and the contact discontinuity by 4 to 5 cells. Weak shocks are produced in the region between the contact discontinuity and the strong shock. They arise from the oscillating contact discontinuity emitting a wave train and these waves steepen to become shocks. Note that shocks along the equator are fast shocks.

The profile of a line along the symmetric axis is showed in Fig. (5.11). The contact discontinuity is located at about  $r = \pm 5.4r_0$  and captured by 4 – 5 cells. The contact discontinuity is mixed with a steep rarefaction wave, making it difficult to identify. The shock, located at about  $r = \pm 7.2r_0$ , is captured by 1-2 cells and it is a slow shock. However, this slow shock is not the same as the usual one-dimensional slow shock, for which

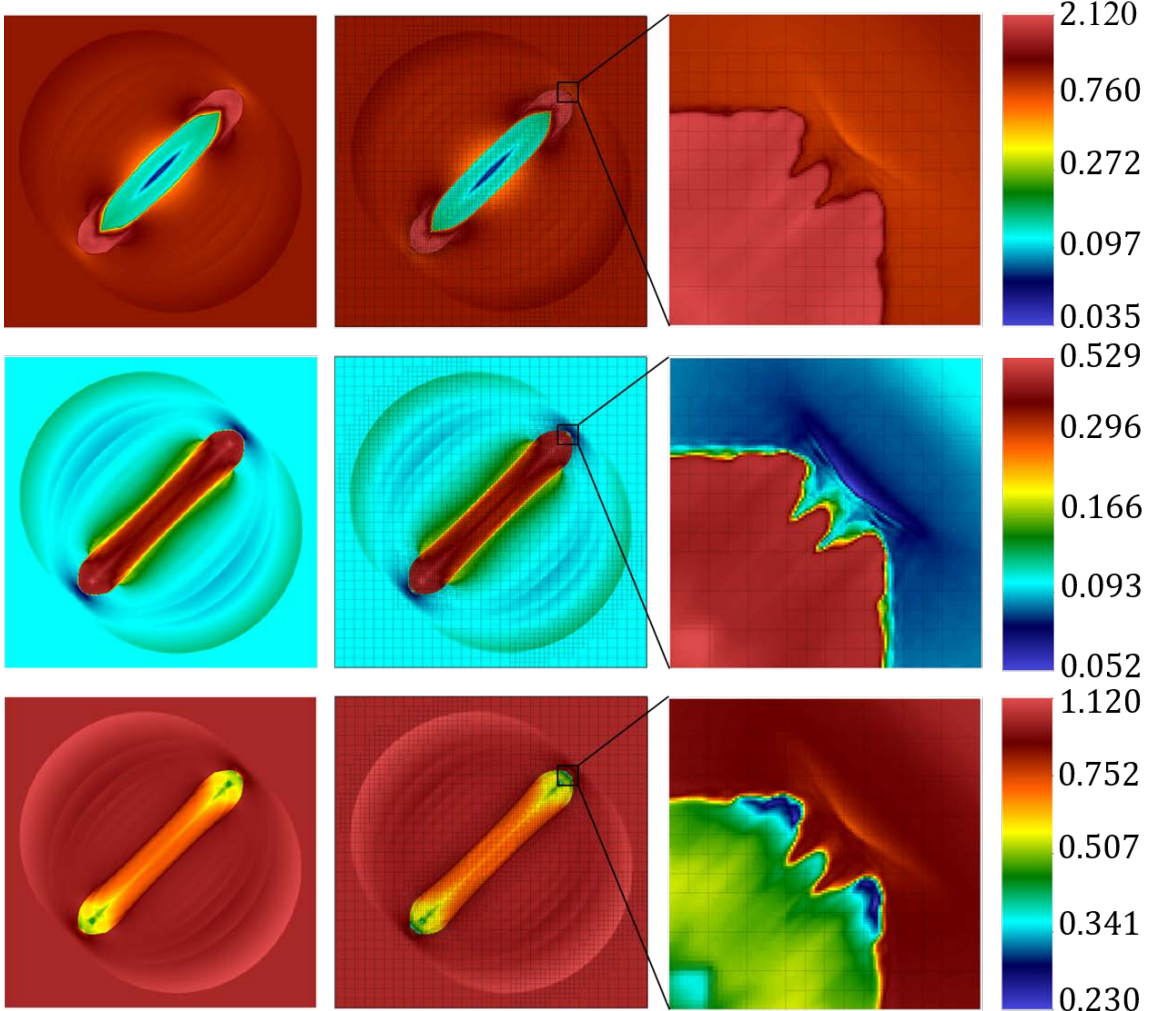


Figure 5.9: The  $xy$  slice image which passes through the box center at  $t = 6r_0/C_A$ . This image has a side  $20r_0$ . The left column is the uniform grid result and the middle is AMR result. The uniform grid resolution and the AMR simulation setup are described in the text. Quantities from the top row to the bottom are the density (normalized by  $\rho_0$ ), pressure (normalized by  $B_0^2$ ) and magnetic field magnitude (normalized by  $B_0$ ), respectively. We also draw the patch structure of AMR with each square representing a patch. (consisting of  $8^3$  cells here) The patch structure catches the shock very well. The AMR result is similar to the uniform-grid case. The AMR result has the "finger" structure in the shock nose along the magnetic axis.

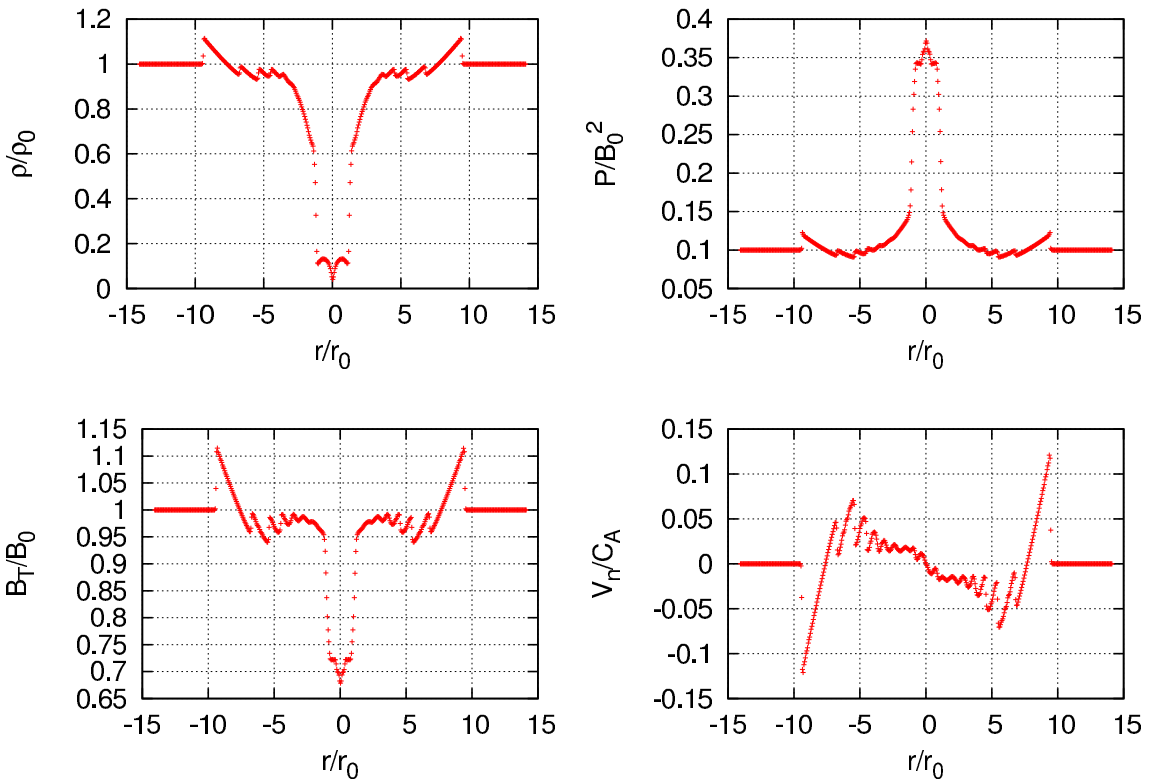


Figure 5.10: The profile of a line to the box center on the equatorial plane at  $t = 6r_0/C_A$ . The four panels are the density in the top left panel, the pressure in top right, the transverse component of magnetic field in bottom left, and the normal component of the velocity field in bottom right. The normal component of the magnetic field and the transverse component of the velocity field are almost zero. The shock are captured by 1 to 2 cells and the contact discontinuity by 4 – 5 cells. Oscillation of the contact discontinuity emit waves, which are steepen to become shocks behind the strongest shock. All shocks are fast shocks.

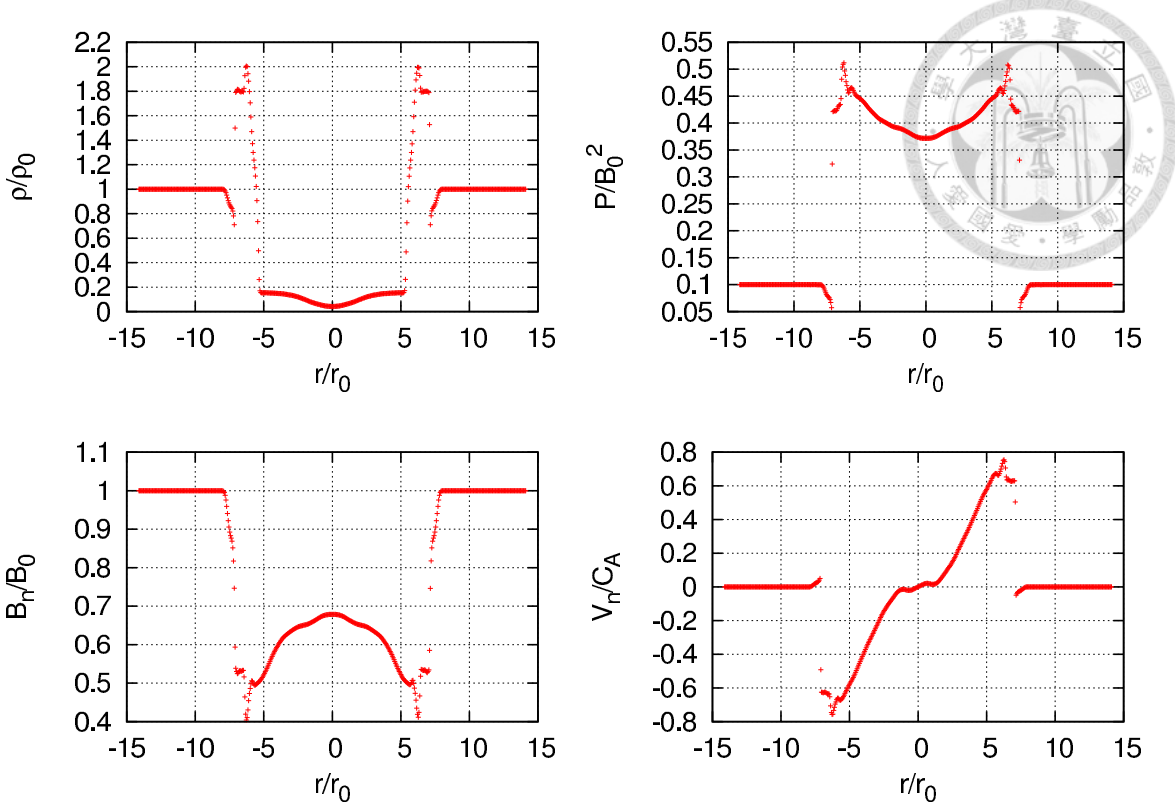


Figure 5.11: The profile along the symmetric axis at  $t = 6r_0/C_A$ . The four panels are same as Fig. (5.10), except for  $B_n$  replacing  $B_T$ . The contact discontinuity is located at  $r = \pm 5.4r_0$  and mixed with the rarefaction wave. The shock is located at  $r = \pm 7.2r_0$ , a slow shock.

only the "transverse component" of the magnetic field changes across the shock. Instead, we find the "normal component" of the magnetic field changes across the shock (c.f. Fig. (5.11)). The suppression of the normal component is due to the fact that upstream magnetic field lines suddenly fan out away from the axis into the downstream region across the shock, and hence the normal component of the magnetic field along the axis must decrease. Finally, upstream of the slow shock is different from the ambient plasma because the oblique fast shock near the axis emits fast waves downstream and influences the upstream region of the slow shock, which can be obviously seen in Figs. (5.9) and (5.11) with a density depression on the axis immediately upstream of the slow shock.

However, a subtle feature is not captured in the uniform-grid simulation. The small-scale "finger" pattern appears at the slow shock noses near the axis, as shown at the rightest column in Fig. (5.9), zoom-in images of at the nose. To demonstrate that this is a physical, and not a numerical, instability, we also rotate the magnetic axis to a different orientation, for which grid structures are different. Indeed if no control noise is added to the system,

the errors of the second order accuracy in our numerical scheme can produce different unstable patterns. In the control test, we inject a control density noise pattern into a sphere of radius  $1.5r_0$ , large enough to enclose the blast wave. Runs of different magnetic field orientations see the same noise pattern if viewed from the magnetic axis. The density perturbation in the coordinate  $(x', y', z')$  has the following form,

$$\frac{\delta\rho}{\rho_0} = \left[ \sin\left(\frac{2\pi}{0.08r_0}x' + \frac{\pi}{4}\right) + \sin\left(\frac{2\pi}{0.10r_0}x'\right) + \sin\left(\frac{2\pi}{0.12r_0}x' - \frac{\pi}{4}\right) \right. \\ \left. \cos\left(\frac{2\pi}{0.08r_0}y' + \frac{\pi}{4}\right) + \cos\left(\frac{2\pi}{0.10r_0}y'\right) + \cos\left(\frac{2\pi}{0.12r_0}y' - \frac{\pi}{4}\right) \right] \times 2 \times 10^{-2}, \quad (5.2)$$

where the background magnetic field is along  $z'$ -axis.

To capture the perturbation wavelength, the resolution of the sphere is equivalent to resolution of refinement level 4 of the AMR simulation, corresponding to 16 cells per shortest noise wavelength. Finally, the initial magnetic field can be expressed as  $\mathbf{B}/B_0 = (\cos(\theta)\cos(\phi), \sin(\theta)\cos(\phi), \sin(\phi))$ . Figure (5.12) shows the pressure image at  $0.5r_0/C_A$  on the shock nose parallel to the ambient magnetic field line for the two different cases,  $(\theta, \phi) = (\pi/4, 17\pi/36)$  and  $(\pi/4, \tan^{-1}(\sqrt{2}))$ . The figure reveals similar patterns for these two cases and validates the dynamical instability, except for some very fine "ringing" pattern present in the case  $(\theta, \phi) = (\pi/4, 17\pi/36)$ , and the separation of fine rings is about  $2 - 3$  cells. By contrast, the grid structure for the other case  $((\theta, \phi) = (\pi/4, \tan^{-1}(\sqrt{2})))$  takes  $\sqrt{3}$  grids to resolve structures in the direction of the ringing pattern, and therefore becomes hardly able to resolve the ringing.

This small-scale feature on the shock noses likely arise from the instability similar to Rayleigh-Taylor type (Rayleigh, 1883; Taylor, 1950) in a decelerating shock. Comprehensive analysis for this feature will be made in a forthcoming work. At this stage, we simply show that the instability is a physical one and can be captured by our high-level AMR simulation.

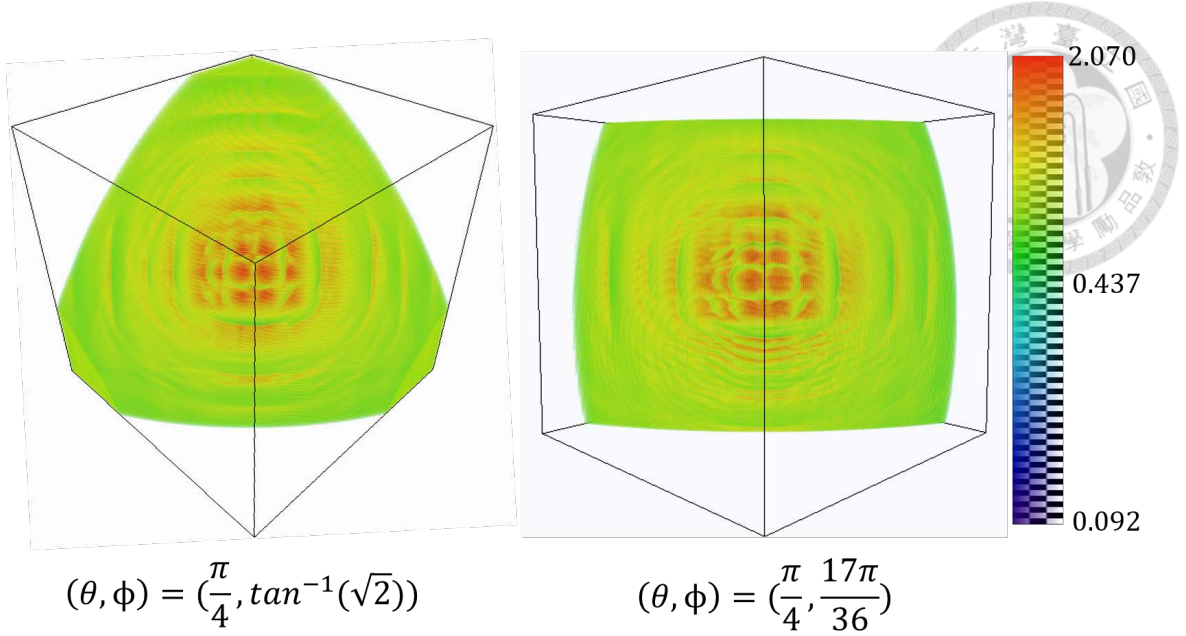


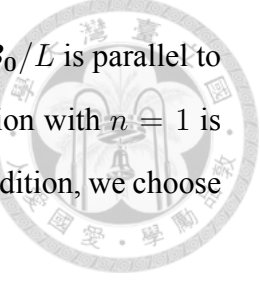
Figure 5.12: The pressure slices (normalized by  $B_0^2$ ) for two different orientations of ambient magnetic fields, which are oriented to  $(\theta, \phi) = (\pi/4, 17\pi/36)$  for the right and  $(\theta, \phi) = (\pi/4, \tan^{-1}(\sqrt{2}))$  for the left at  $t = 0.5r_0/C_A$ . The box size is the same with the size of the zoom-in image in Fig. (5.9). The initial density perturbation is given by Eq. (5.2). Small structures are similar for the two, except for the resolved ringing pattern in the lower middle region of the right panel that is not resolved in the left panel.

### 5.1.5 Magnetic field with ABC pattern

This is a new test problem demonstrating 3D relaxation process for a MHD system. Due to its intrinsic periodic boundary condition, this problem is also ideal for examining the weak scaling performance for a parallelized code. Inspired by the intriguing Arnold-Beltrami-Childress (ABC) flow, which is a three-dimensional incompressible flow (Arnold, 1965; Childress, 1970), we examine the turbulent relaxation of magnetic field with the ABC configuration in a uniform plasma with density  $\rho_0$  and pressure  $P_0$ . The magnetic field pattern is  $\mathbf{B}_0 (= (B_{x,0}, B_{y,0}, B_{z,0}))$  and

$$\begin{aligned}
 B_{x,0} &= A \sin\left(\frac{2\pi n}{L} z\right) + C \cos\left(\frac{2\pi n}{L} y\right), \\
 B_{y,0} &= B \sin\left(\frac{2\pi n}{L} x\right) + A \cos\left(\frac{2\pi n}{L} z\right), \\
 B_{z,0} &= C \sin\left(\frac{2\pi n}{L} y\right) + B \cos\left(\frac{2\pi n}{L} x\right),
 \end{aligned} \tag{5.3}$$

where the cubic box length  $L$  is set to unity,  $A$ ,  $B$  and  $C$  are constants and  $n$  is an integer governing the number of periods in the box. It is noted that this configuration is in a



force-free equilibrium since the current density  $\mathbf{J}_0 \equiv \nabla \times \mathbf{B}_0 = 2\pi n \mathbf{B}_0 / L$  is parallel to the magnetic field. As shown in Appendix A, one finds the configuration with  $n = 1$  is stable. Therefore, we choose  $n = 2$  state as the initial equilibrium. In addition, we choose  $A = B = C = \sqrt{P_0}$ , i.e., plasma  $\beta = 1$ .

We also let this plasma move with a SMALL uniform drift velocity along the diagonal direction, i.e., the drift velocity  $\mathbf{V}_0 = (V_{x,0}, V_{y,0}, V_{z,0})$  with  $V_{x,0} = V_{y,0} = V_{z,0}$  and  $V_{x,0} > 0$ . The magnitude of the drift velocity is  $8\sqrt{\gamma}$  times smaller than the sound speed  $C_s \equiv \sqrt{\gamma P_0 / \rho_0}$ . In principle, this uniform flow doesn't affect the stability due to the Galilean invariance of MHD equations. However, the static grids can weakly break the Galilean invariance, depending on numerical schemes, to favor a particular reference frame. When the plasma is static, there is an instability of long and thin (grid-scale) structures produced in the simulation. This instability still persists in the  $n = 1$  equilibrium state, which is proven to be ideal MHD stable, as shown in Appendix A. Similar structures are also produced in Athena code. The physics underlying these long and thin structures is interesting, and it may originate from resistive instability despite no resistivity is explicitly used in these codes. It is well known that fast resistive tearing mode instabilities can occur in an ideal MHD marginally stable plasma, e.g. Rosenbluth et al. (1973). We shall further investigate on this instability in a future work. For now, we find the uniform flow can numerically suppress these small-scale instabilities and yields only physical large-scale ideal MHD instabilities.

Finally, initial perturbations should be added on the equilibrium configuration to control the ideal MHD instability. In order to find appropriate perturbations, we start with the above initial configuration with no explicitly added noise in a low resolution simulation. An unstable  $n = 1$  perturbation then arises out of numerical noise. We analyze such a unstable magnetic field perturbation in the linearly regime and identify the largest four Fourier components of the unstable  $\delta \mathbf{B}$ , which is supposed to be the most unstable eigen-



mode:

$$\frac{\delta B_x}{\sqrt{P_0}} = \left\{ +2.37 \cos \left[ \frac{2\pi}{L} (x+y) \right] + 2.10 \sin \left[ \frac{2\pi}{L} (x+y) \right] \right. \\ - 3.48 \cos \left[ \frac{2\pi}{L} (x+z) \right] - 3.18 \sin \left[ \frac{2\pi}{L} (x+z) \right] \\ - 5.86 \cos \left[ \frac{2\pi}{L} (z-y) \right] + 5.60 \sin \left[ \frac{2\pi}{L} (z-y) \right] \\ \left. + 2.08 \cos \left[ \frac{2\pi}{L} (x-z) \right] + 1.94 \sin \left[ \frac{2\pi}{L} (x-z) \right] \right\} \times 10^{-2}, \quad (5.4)$$

$$\frac{\delta B_y}{\sqrt{P_0}} = \left\{ -2.37 \cos \left[ \frac{2\pi}{L} (x+y) \right] - 2.10 \sin \left[ \frac{2\pi}{L} (x+y) \right] \right. \\ - 4.90 \cos \left[ \frac{2\pi}{L} (x+z) \right] + 5.37 \sin \left[ \frac{2\pi}{L} (x+z) \right] \\ + 3.60 \cos \left[ \frac{2\pi}{L} (z-y) \right] + 3.80 \sin \left[ \frac{2\pi}{L} (z-y) \right] \\ \left. - 3.00 \cos \left[ \frac{2\pi}{L} (x-z) \right] + 3.22 \sin \left[ \frac{2\pi}{L} (x-z) \right] \right\} \times 10^{-2}, \quad (5.5)$$

$$\frac{\delta B_z}{\sqrt{P_0}} = \left\{ -3.23 \cos \left[ \frac{2\pi}{L} (x+y) \right] + 3.66 \sin \left[ \frac{2\pi}{L} (x+y) \right] \right. \\ + 3.48 \cos \left[ \frac{2\pi}{L} (x+z) \right] + 3.18 \sin \left[ \frac{2\pi}{L} (x+z) \right] \\ + 3.60 \cos \left[ \frac{2\pi}{L} (z-y) \right] + 3.80 \sin \left[ \frac{2\pi}{L} (z-y) \right] \\ \left. + 2.08 \cos \left[ \frac{2\pi}{L} (x-z) \right] + 1.94 \sin \left[ \frac{2\pi}{L} (x-z) \right] \right\} \times 10^{-2}. \quad (5.6)$$

Note that Eqs. (5.4), (5.5) and (5.6) yields a perturbed magnetic field also satisfying the divergence-free constraint, and that the wave numbers of the perturbation eigenmode rotate  $\pm 45$  degrees from those of the equilibrium field with  $\sqrt{2}$  longer wavelength. Finally, we add the magnetic field perturbation into the  $n = 2$  force-free equilibrium as the initial condition for high-resolution runs.

The numerical setup (data reconstruction, Riemann solver and floating-point precision) are the same as the previous blast wave problem. Periodic boundary condition is used.

Figure (5.13) is the 3-D image of the current density magnitude  $|\mathbf{J}|$  (normalized by  $\sqrt{P_0}/L$ ) at  $t = 1.3L/C_s$  (the upper row) and  $t = 2.0L/C_s$  (the lower row) with two different orientations. This image is constructed by AMR simulation with  $128^3$  grids at the base level and 4 refinement levels. The quantity  $|\mathbf{J}|/|\mathbf{B}|$  is the refinement criterion

and the grid with this quantity higher than  $24/\Delta h(k-1)$  is refined to level  $k$ , where  $k = 1, 2, 3$  and  $4$ , and  $\Delta h(k)$  is the  $k$ -th level grid size. Similar to the Orszag and Tang vortex test, this criterion aims to capture the magnetic reconnection.

Figure (5.13) reveals strong current densities occurring in very thin sheets, and the two adjacent current sheets merge together in less than one sound crossing time. The magnetic energy is found to decrease dramatically during the merging process (c.f. Fig. (5.15)). Therefore, the magnetic reconnection must occur at the appearance of strong current sheets. It is however difficult to quantify the local reconnection rate of such 3D reconnection, unlike Sweet-Parker or Petschek reconnection (Petschek, 1964) in 2D, since the strongest current densities appear in several relatively short-lived patches on the sheet. The patch reconnection occurs not at the magnetic nulls but in weak field regions. This result is at variant with the 3D separator reconnection proposed before (Parnell and Haynes, 2010), which is filament-like reconnection. It remains to be seen whether the patch reconnection is generic in 3D MHD.

We also examine the evolution of this unstable force-free equilibrium and find the system relaxes to another steady configuration. Figure (5.14) shows the time evolution of a slice image of the magnetic field magnitude. Over 31 sound crossing time ( $31L/C_s$ ), the system approached an  $n = 1$  equilibrium state which can be fitted by the following formula

$$\begin{aligned}\frac{B_x}{\sqrt{P_0}} &= 0.33 \sin \left[ \frac{2\pi}{L}(z - 0.68) \right] + 0.80 \cos \left[ \frac{2\pi}{L}(y - 0.50) \right], \\ \frac{B_y}{\sqrt{P_0}} &= 0.85 \sin \left[ \frac{2\pi}{L}(x - 0.36) \right] + 0.33 \cos \left[ \frac{2\pi}{L}(z - 0.68) \right], \\ \frac{B_z}{\sqrt{P_0}} &= 0.80 \sin \left[ \frac{2\pi}{L}(y - 0.50) \right] + 0.85 \cos \left[ \frac{2\pi}{L}(x - 0.36) \right].\end{aligned}\quad (5.7)$$

Eq. (5.7) reveals that the relaxed state is the ABC configuration with only one period.

The respective evolutions of total energy ( $E_T \equiv \int e d^3x$  with the total energy density  $e$  defined in Chapter (3)), magnetic energy ( $U_B \equiv \int |\mathbf{B}|^2/2d^3x$ ), flow energy ( $U_V \equiv \int \rho |\mathbf{V}|^2/2d^3x$ ) and magnetic helicity ( $H \equiv \int \mathbf{A} \cdot \mathbf{B} d^3x$  with the vector potential  $\mathbf{A}$ ) are shown in Fig. (5.15). As expected, the total energy remains constant to a high accuracy, due to the CTU scheme being a finite volume method. By contrast, the magnetic energy is monotonically decreasing, while the flow energy first increases dramatically and then

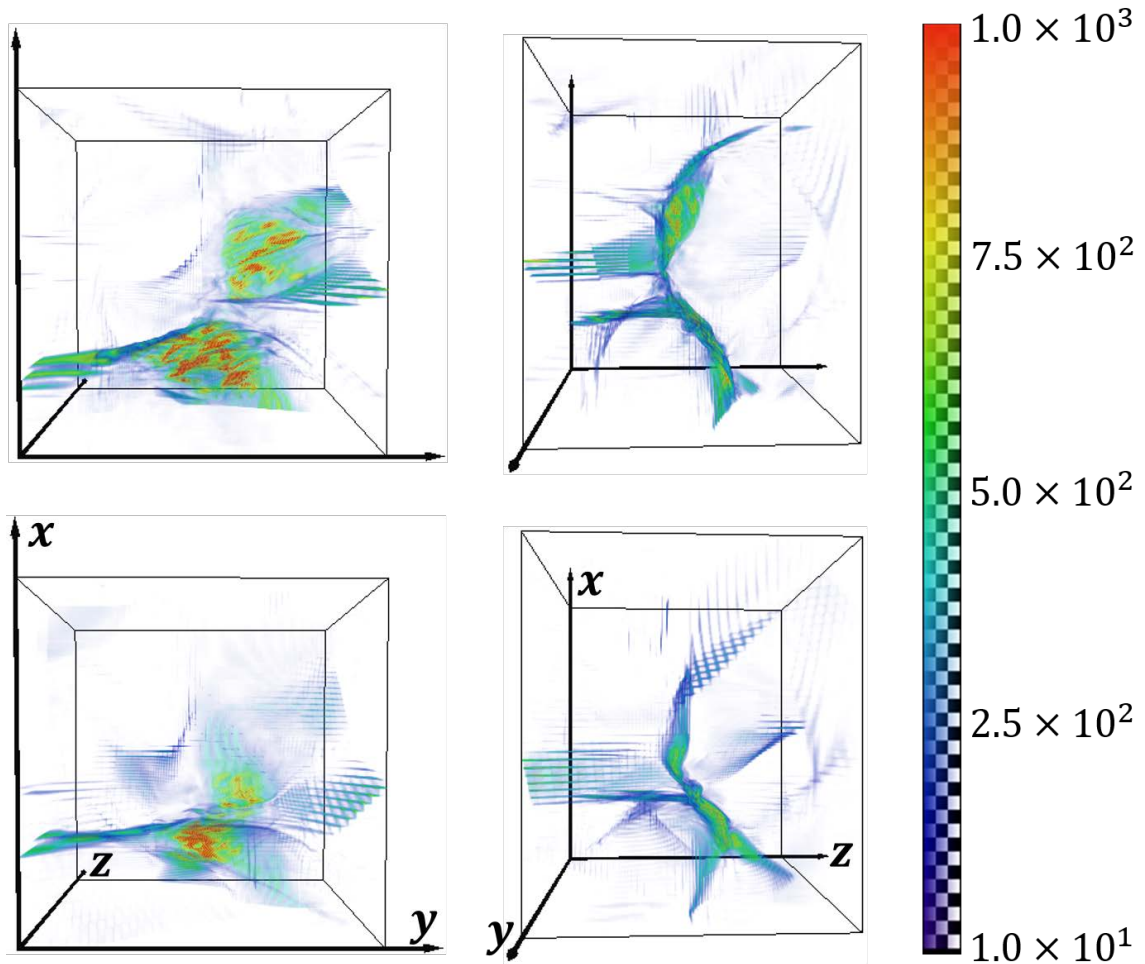


Figure 5.13: The 3D image of the current density magnitude normalized by  $\sqrt{P_0}/L$  at  $t = 1.3L/C_s$  (upper row) and  $t = 2.0L/C_s$  (lower row) with two different viewing angles. The domain of these images is  $[L/4, 5L/8] \times [0, 3L/8] \times [0, 5L/16]$  in the rest frame in which the background uniform flow becomes zero. Current sheets are produced shortly before  $t = 1.3L/C_s$  and two adjacent current sheets tend to merge together at  $t = 2.0L/C_s$ . The strongest current densities are distributed over several patches on the thin sheets.

oscillates. However, the flow energy decreases to zero in the end. On the other hand, the magnetic helicity, which is also a conserved quantity in ideal MHD and related to the linkage of magnetic field lines, only drops by about 2% up to 32 sound crossing times. Moreover, the magnetic energy for the final relaxed state is about twice smaller than the initial state. This can be derived from the conservation of the magnetic helicity.

Note that the initial and final state follow the ABC patterns. Straightforward calculations yield the magnetic energy and the magnetic helicity with the ABC field pattern to be  $U_B = (A^2 + B^2 + C^2)L^3/2$  and  $H = (A^2 + B^2 + C^2)L^4/(2\pi n) = U_BL/(\pi n)$ , respectively. Since the magnetic helicity is a constant, we conclude  $U_B \propto n$ , and hence the magnetic energy for the final state should be twice smaller than the initial state as  $n$  changes from 2 to 1. The above analysis confirms the Taylor's conjecture that unstable MHD systems tend to minimize magnetic energy subject to the constraint of a constant magnetic helicity (Taylor, 1986). The minimum-energy state is a force-free state with a uniform current-to-field ratio, and our final ABC configuration is such a minimum-energy state.

## 5.2 Performance Test

In this section, we demonstrate the performance of GAMER-MHD. This section will be divided into two parts. The performance of GPU computation is measured first and compares with the performance of CPU computation under the same coding algorithm. Second, the overall performance of the strong and weak scaling tests will be conducted. The PPM interface data reconstruction and the Roe Riemann solver will be adopted. Unlike the accuracy test, single precision is used in this section. Finally, the initial, boundary conditions, and AMR setups all follow Section 5.1.5.

### 5.2.1 GPU Performance

We adopt the number of cell-updates per second for quantifying the performance. We first measure the performance by simulating different resolutions of uniform grids with

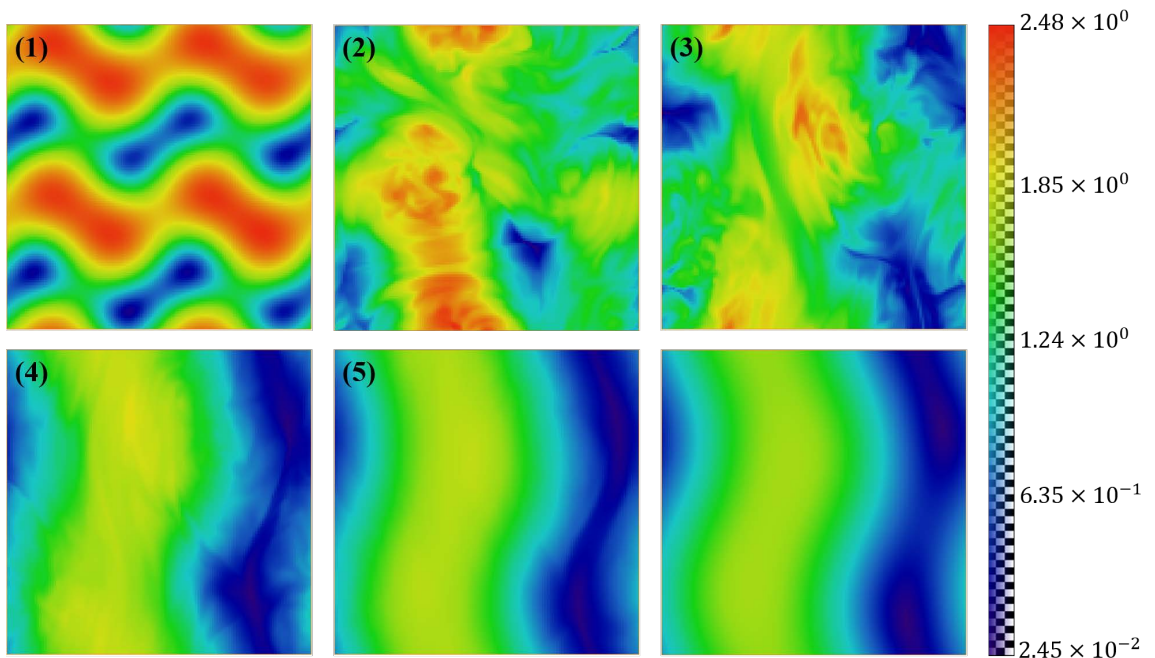


Figure 5.14: The time sequence of magnetic field magnitude  $xz$  slice images. These images are drawn at  $y = 0.77L$  in the rest frame in which the background uniform flow becomes zero. Numbers labeled in the figure stand for the chronological order and they are at  $t = 0, 3.9, 7.7, 15.5$  and  $31.0$ , respectively. Here time is normalized by  $L/C_s$ . The color stands for the magnetic magnitude. The rightest bottom image is constructed by Eq. (5.7), which is the one-period ABC-flow pattern configuration. The reconstructing image agrees with the 5-th image very well, and the system converges to a stable state.

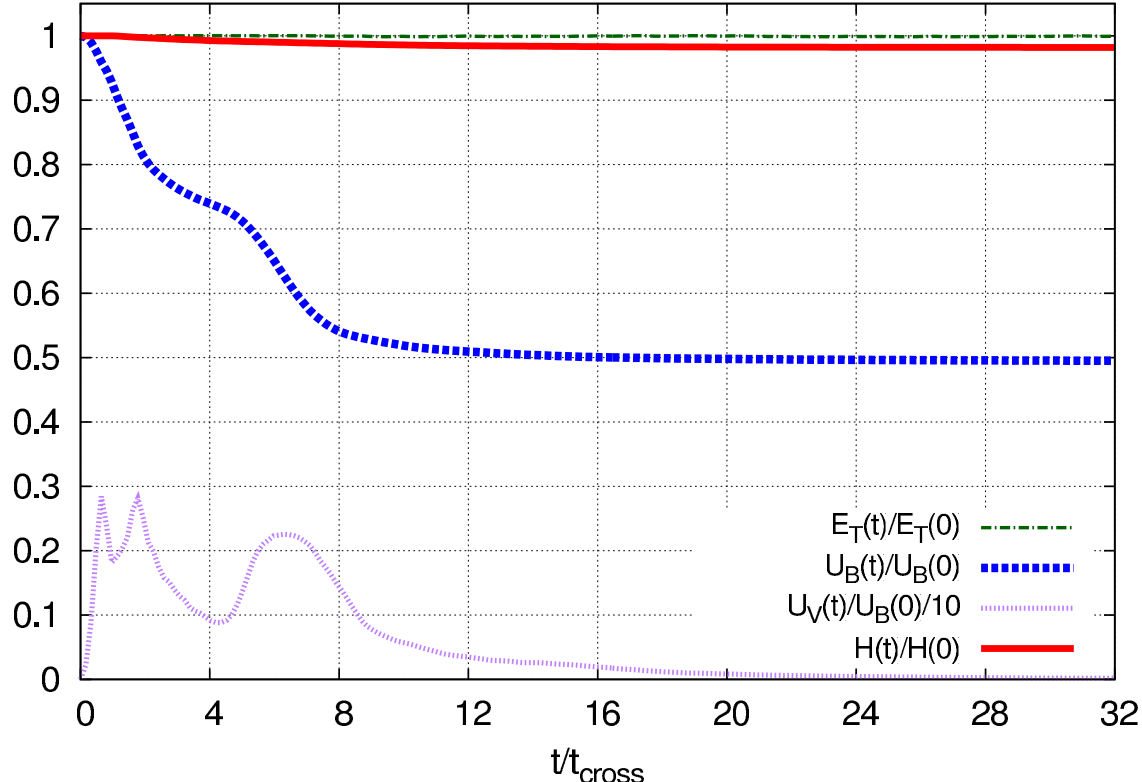


Figure 5.15: The evolution of the total energy ( $E_T$  with the dash-dotted line), the magnetic energy ( $U_B$  with the dashed line), the flow energy ( $U_V$  with the dotted line) and the magnetic helicity ( $H$  with the solid line). The horizontal axis is the time normalized to the sound crossing time ( $t_{cross} = L/C_s$ ). The total, magnetic energy and helicity are normalized to their corresponding initial values while the flow energy is normalized to  $U_B(0)/10$  with the initial magnetic energy  $U_B(0)$  for comparison. The total energy remains the same due to the finite-volume method. The magnetic energy decreases while the flow energy first increases and then oscillates. However, the flow energy decreases to zero in the end. Finally, our scheme maintains the magnetic helicity at least 98% up to 32 sound crossing time. This figure shows the consistency with Taylor's conjecture (Taylor, 1986).

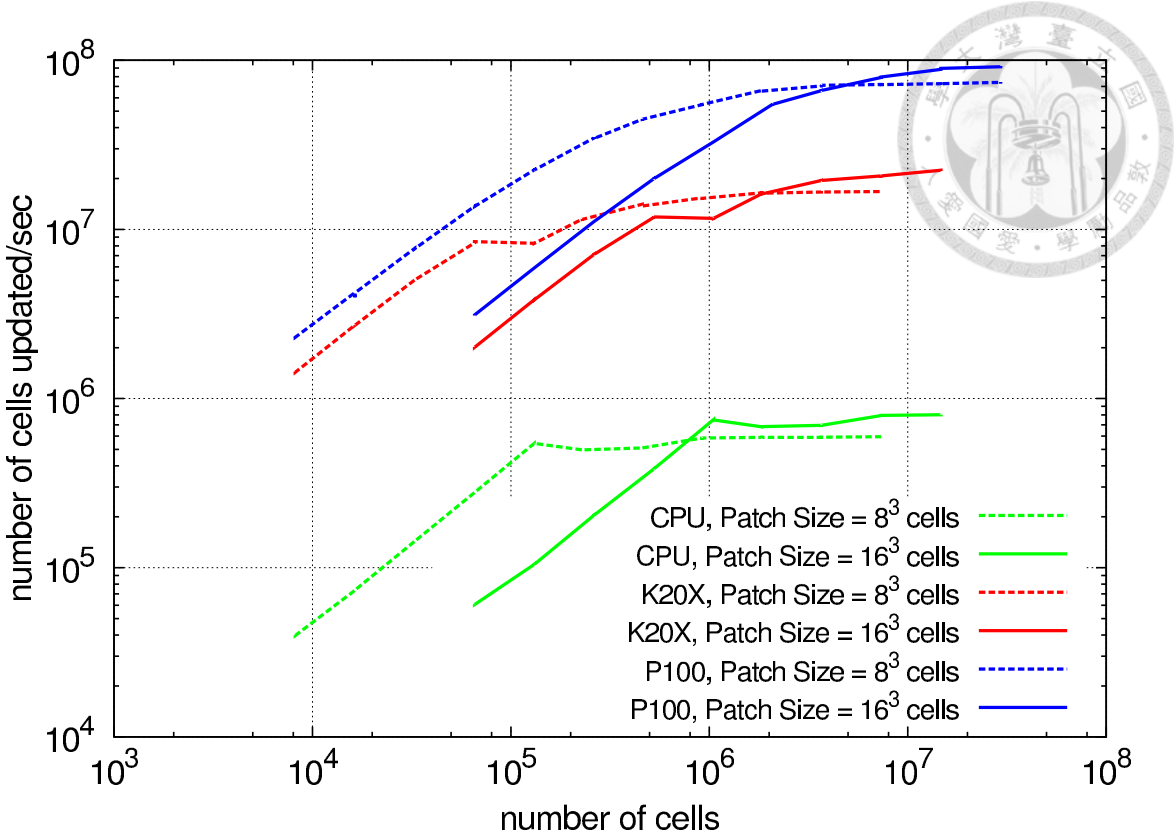


Figure 5.16: The number of cell-updates per second versus total simulation cells. We use two different sizes of the patch ( $8^3$  cells for dashed lines and  $16^3$  cells for solid lines) to measure the performance of two different GPUs, Tesla P100 (blue lines) and Tesla K20X (red lines). We also plot the CPU performance under the same coding structure for the numerical scheme. The speed up ratio (GPU performance over CPU one ) is at least 25.

only one GPU. Roe’s Riemann solver and PPM data reconstruction are adopted. The simulations are conducted on two different generations of GPUs, Tesla P100, newly released in 2016 and Tesla K20X, the previous generation released in 2012.

Figure (5.16) shows the single-GPU performance. We measure the performance of two different patch sizes,  $8^3$  and  $16^3$ . The performance is a monotonic function of the total cell numbers to be updated, and saturated when the cell number is sufficiently large. From Fig. (5.16), when the total cell number exceeds  $2 \times 10^6$ , saturation begins to be observed and they are saturated at about  $2 \times 10^7$  and  $9 \times 10^7$  cell-updates per second for K20X and P100, respectively. We also plot the CPU performance with the same numerical scheme as GPU. The CPU specification is AMD Opteron Processor 6276 with 16 processing cores. The CPU performance is saturated at about  $8.0 \times 10^5$  cell-updates per second. The speed-up ratio of GPU over CPU is 25 for K20X and  $\geq 100$  for P100.

Theoretically, P100 is about 2.4 times faster than K20X as P100 has 3584 GPU cores

with 1328 MHz clock frequency and K20X has 2688 cores with 732 MHz clock frequency. However, our result reveals higher performance for P100 by a factor 4.5. This is likely caused by about 2.8 higher number of registers per processor on P100, suggesting temporary memory space can have significant impacts to our sophisticated MHD solver.

The performance with  $16^3$  cells per patch is slightly better than  $8^3$ . This is due to that data are always decomposed in unit of patch groups (defined in Section 4.3). Given a patch group, the "ghost-grid" data are prepared for evolving grids next to the patch-group boundary. The ghost-grid size depends on numerical schemes (3 cells for each direction if PLM interpolation and 4 cells if PPM). Therefore, the ratio between the total ghost-grids data and the total updated data can vanish for a very large patch size. This limit is however not practical when the AMR is in use, and compromises must be found.

### 5.2.2 Overall Performance

To end this section, we perform the overall efficiency of GAMER MHD application with AMR simulation and hybrid MPI/OpenMP/GPU parallelization. Again, we measure the the number of cell-updates per second to quantify the performance efficiency. There are two standard MPI scaling tests, the strong scaling and weak scaling tests. The performance benchmarks are conducted in Blue Water cluster of NCSA at University of Illinois, where each computing node is equipped with a AMD Opteron Processor 6276 (16 processing cores) CPU and a Tesla K20X GPU.

The total number of cells is fixed in the strong scaling test. Ideally, the wall-clock time, the total simulating time, is twice smaller when twice number of computing nodes are in use. However, it is difficult to achieve ideal performance with a very larger number of computing nodes since as the work load becomes lighter, each GPU has less number of cells to execute leading to lower efficiency (see Fig. (5.16)). Moreover, the execution time of AMR operations (see Section 4.2) with OpenMP parallelization and MPI communications among different computing nodes will become non-negligible for a large node number; this will decrease the overall performance as well. Therefore, the strong scaling test is to find the sweet spot of the computing node number in GAMER application that

allows the computation to complete in a reasonable amount of time. Figure (5.17) shows the strong scaling overall performance. The overall performance deviates from the ideal scaling not significantly up to  $10^3$  computing nodes, but still have  $1.5 \times 10^{10}$  cell-updates in one second for 2048 computing nodes.

We stress that the ideal scaling for one node is about 0.82 times smaller than the GPU performance measured in part (i), i.e., the multi-node performance dropping by 18% from the single node. The AMR operations (c.f. Section 4.2) and MPI data communication time are about 9% and 6% of the wall-clock time when we analyze the time consumption of each operation for  $N = N_{min}$ . Thus the deviation from the GPU performance is from AMR operations and MPI data communication. This result demonstrates the nearly perfect overlap of GPU and CPU concurrent executions (c.f. Section 4.3).

Figure (5.18) shows the detailed quantitative analysis for the strong scaling test. Two quantities are introduced in this figure, parallel efficiency and doubling efficiency. The former marks the efficiency of  $N$  nodes compared with the minimum node number  $N_{min}$ , and the latter indicates the performance drop by increasing the node number by a factor of 2. While the former is the conventional measure of performance of a large node number, the latter is a new measure and more practical for users to determine the optimal node number for a given problem size as this is an indicator near the saturation end. The parallel efficiency is defined as  $[T(N_{min})/T(N)]/(N/N_{min})$ , in which  $N$  is the number of computing nodes,  $N_{min}$  is the minimum number of computing nodes adopted in the test and  $T(N)$  is the wall-clock time with  $N$  computing nodes. On the other hand, the doubling efficiency is defined as  $[T(N/2)/T(N)]/2$ .

Figure (5.18) shows 70% parallel efficiency and 78% doubling efficiency up to  $10^3$  computing nodes. The wall-clock time and the memory per computing node are deviated from the ideal scaling by 14% and 2% for 512 computing nodes, and by 45% and 25% for 1024 nodes, respectively. We also found the MPI data communicating time for 2048 nodes is only about 5 times smaller than 64 nodes and Refinement/Derefinement Operations in AMR (c.f. Section 4.2) for 2048 nodes is about 6 times smaller than 64 nodes. Above two operations don't obey the scaling law. Therefore, the drop of parallel efficiency may

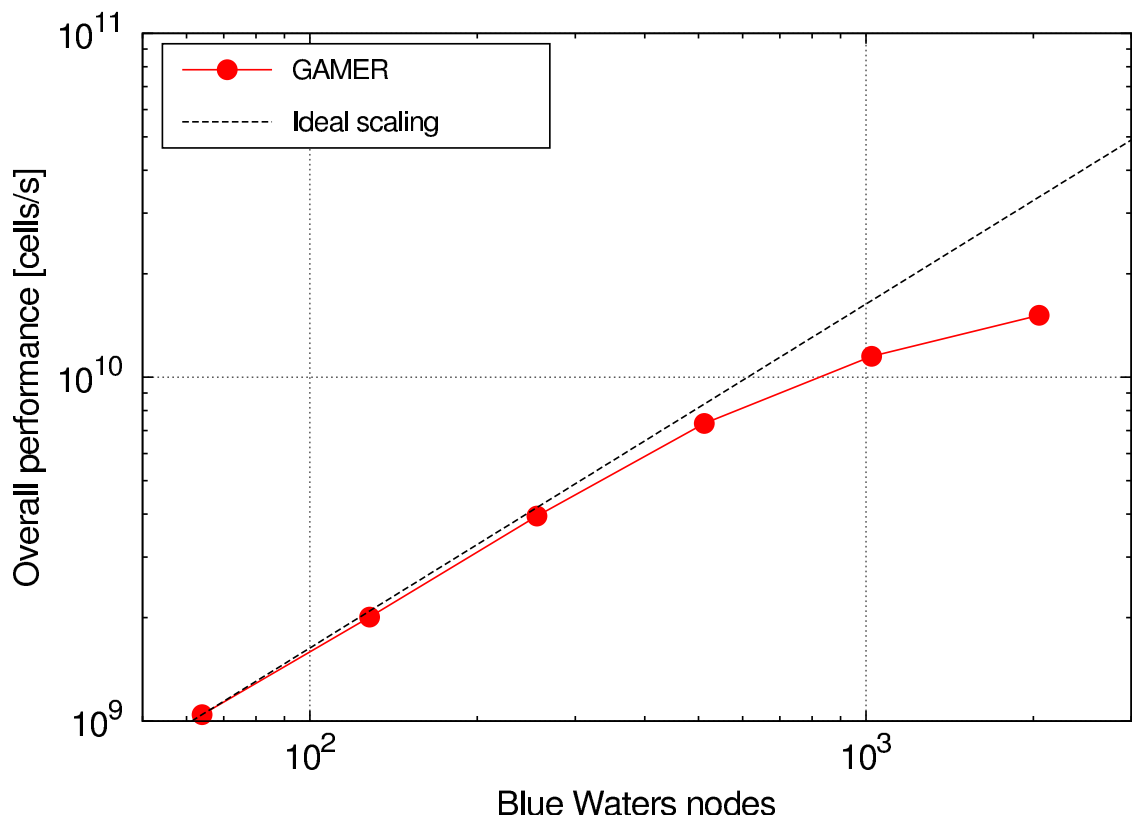


Figure 5.17: The overall performance for the strong scaling test. The horizontal axis is the number of computing nodes. The vertical axis is the number of cell-updates in one second. Filled circle points is GAMER's strong scaling test result and the dashed line is the ideal scaling.

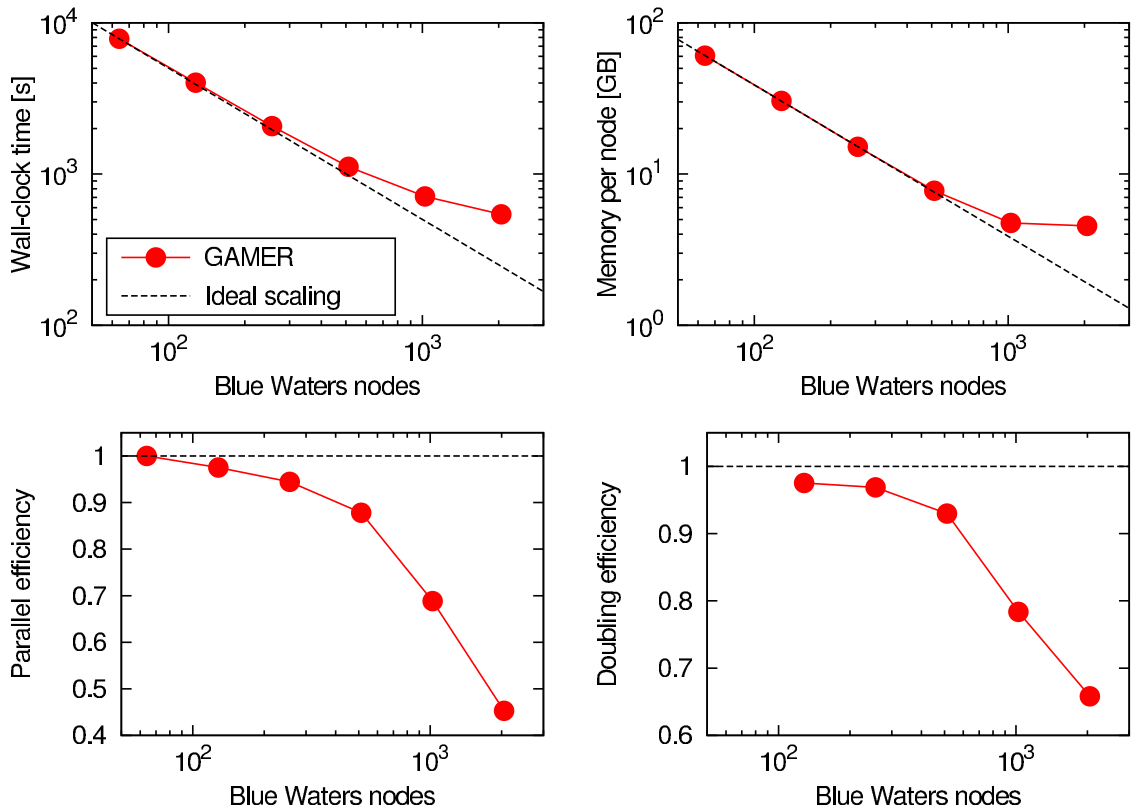


Figure 5.18: The quantitative analysis of the strong scaling test for GAMER application. The horizontal axis is the number of Blue water computing nodes. Four panels show different quantities and they are (1) wall-clock time in the left top panel, (2) memory per node in the right top panel, (3) parallel efficiency in the left bottom panel, and (4) doubling efficiency in the right bottom panel. Definitions of these quantities are in the main text. There are 70% parallel efficiency and 78% doubling efficiency up to  $10^3$  computing nodes.

be mainly due to the increasing time fraction in both MPI data communication and reconstructing the AMR tree structure, i.e. Refinement/Derefinement Operations in AMR.

The problem size, thus the total number of cells, is proportional to the number of computing nodes in the weak scaling test. Unlike to the strong scaling test, the wall-clock time is independent of the number of computing nodes ideally. Figure (5.19) shows the overall performance for the weak scaling test. Similar to the strong scaling result, the overall performance for the weak scaling is also not significantly deviated from the ideal scaling and can update  $5.0 \times 10^{10}$  cells in one second for 4096 computing nodes. The overall performance with the AMR application is almost the same with the uniform-grid simulation, revealing that the extra works in the AMR application take only an insignificantly small fraction of the computing time spent on the solver. The uniform-grid simulation has the effective  $8192^3$  cells when 4096 computing nodes are used.

Figure (5.20) reveals the detailed quantitative analysis for the weak scaling test. Here the parallel efficiency is defined as  $T(N_{min})/T(N)$ . It still has 70% parallel efficiency for about  $2.0 \times 10^{11}$  cell-updates by using  $10^3$  computing nodes, which is slightly better than the strong scaling result. In the weak scaling test, the MPI time fraction may be the indicator for non-ideal scaling efficiency. Figure (5.20) shows the sum of the MPI time fraction and the parallel efficiency is roughly equal to one. For example, the MPI time fraction is 25% and the parallel efficiency we measured is 67% in the AMR case for 4096 computing nodes.

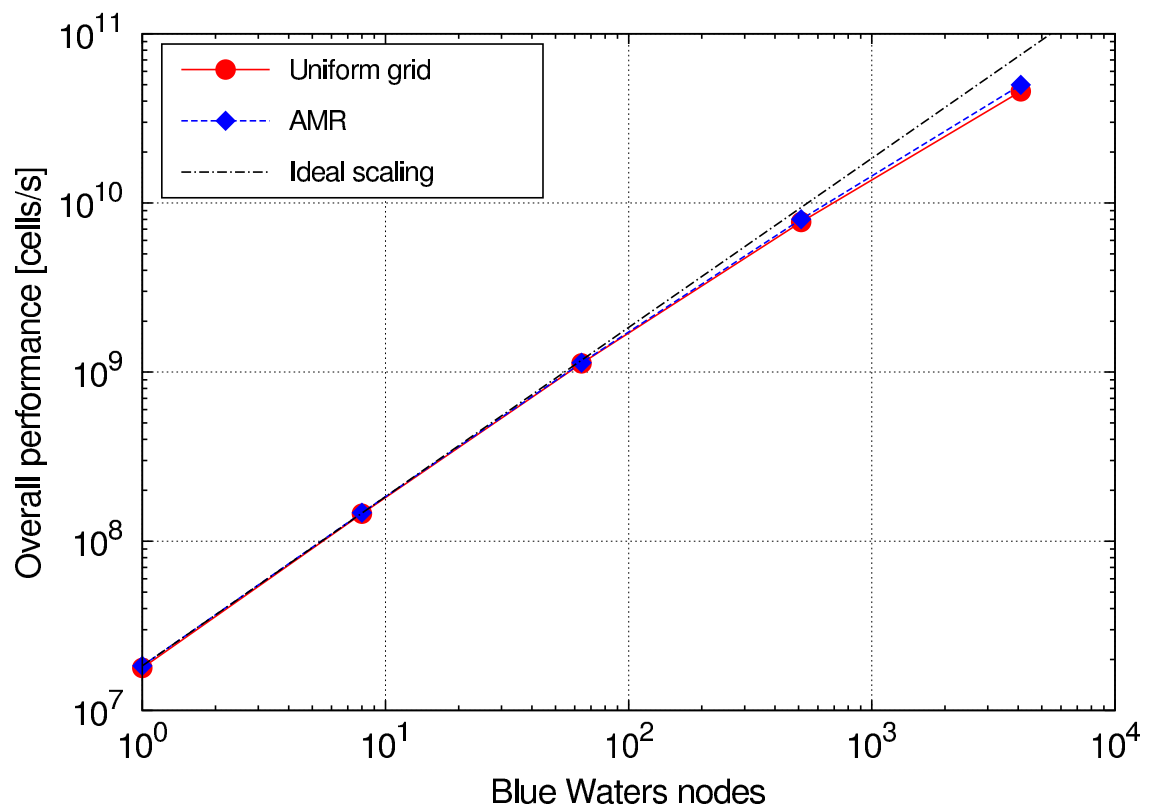


Figure 5.19: The overall performance for the weak scaling test. The horizontal and vertical axes are the same with Fig. (5.17). Filled circle points are the uniform application results and Filled diamond points are the AMR application. The dashed line is the ideal scaling.

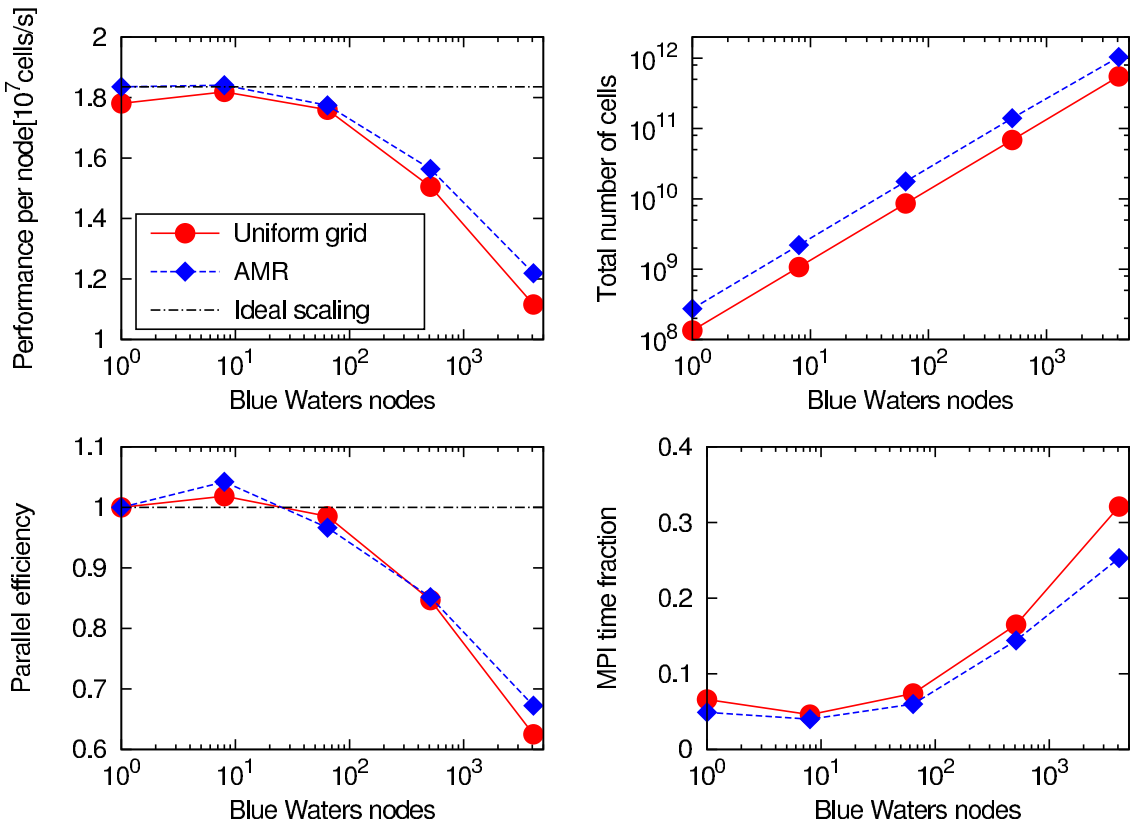


Figure 5.20: The quantitative analysis of weak scaling test for GAMER application. There are four panels in this figure and they are (1) performance per node (number of cells updated per second per node) in the left top panel, (2) total number of cells in the right top panel, (3) parallel efficiency in the left bottom panel, and (4) MPI time fraction in the right bottom panel. The AMR case has better parallel efficiency than the uniform one which is consistent with the MPI time fraction result.





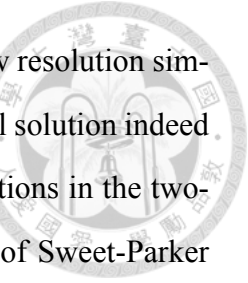
# Chapter 6

## Conclusions for Part I

In this work, we demonstrate successful implementation of the MHD scheme (CTU+CT) into GAMER. The Balsara’s method is also implemented in AMR to maintain the divergence-free constraint of the fine grid magnetic field. Under GAMER’s structure, the MHD scheme can be accelerated by GPU and AMR operations are executed parallel by multi-core CPU via OpenMP. The data transfer between CPU and GPU memory is overlapped by the MHD scheme execution via *CUDA stream*. The preparation and closing steps, performed in the multi-core CPU is concurrent with the GPU execution. Finally, GAMER-MHD can be executed by multi-nodes via MPI and the Hilbert curve decomposition is used to balance the computing loading each node.

Our performance test results show the following. The single GPU performance of the MHD solver can reach  $2 \times 10^7$  cell updates/sec for K20X and  $9 \times 10^7$  cell updates/sec for P100. With up to thousands of computing nodes, such a speed does not degrade due to the concurrency of GPU and CPU execution even with AMR, and due to the high efficiency of parallelization among nodes with at least 70% parallel efficiency.

We have adopted the linear wave and shock-tube tests to verify the correctness of the MHD solver implementation. The Orszag and Tang vortex and the blast wave aim to test AMR implementation, and we find the results can reproduce those with high-resolution uniform-grid simulations. Taking advantage of the AMR strategy, very high resolution simulations are easily achievable for these test problems with reasonable run times, in which interesting small-scale features, undetected before, are found. For example, in the



Torrilhon shock tube test the erroneous compound wave appearing in low resolution simulations can be eliminated by increasing the resolution, and the numerical solution indeed converges to the exact solution albeit at a slow rate; magnetic reconnections in the two-dimensional Orszag and Tang Vortex test are identified to be a variant of Sweet-Parker type; in the blast-wave test, weak three-dimensional small-scale instabilities are discovered near the slow shock front parallel to the magnetic field.



## Part II

# LINEAR WAVE DARK MATTER PERTURBATIONS





## Chapter 7

# Brief Review of Wave Dark Matter

A new form of dark matter, so-called  $\psi$ DM, wave dark matter or fuzzy dark matter, that consists of extremely light particles of typical particle mass,  $10^{-22}$ eV (Hu et al., 2000; Schive et al., 2014; Marsh and Pop, 2015; Calabrese and Spergel, 2016; Hui et al., 2017b), has been noted to exhibit nice, yet peculiar, features for explaining recent observational results. For example, it produces finite density cores for Milky Way dwarf spheroid galaxies to reside in (Lora and Magaña, 2014; Schive et al., 2014), an observational fact (Moore, 1994; Goerdt et al., 2006; Gilmore et al., 2007; Walke and Peñarrubia, 2011; Amorisco et al., 2013) that has been puzzling cold dark matter (CDM) proponents for some time. This core in the  $\psi$ DM scenario results from the uncertainty principle of these extremely light particles, which yields quantum pressure and avoids the central density singularity predicted by CDM (Navarro et al., 1997). Other peculiar features of  $\psi$ DM arise from the linear matter spectrum described below.

The  $\psi$ DM spectrum is known to be such that it resembles CDM spectrum in long wavelengths and becomes heavily suppressed in short wavelengths (Hu et al., 2000). The spectral suppression, due also to the quantum pressure, not only occurs already in the radiation-dominant era but occurs sharply at some transition wavenumber, much sharper than the suppression of the short-wavelength spectrum of warm dark matter (WDM) (Bode et al., 2001). This spectral feature on one hand leads to paucity of Milky Way satellite galaxies (Klypin et al., 1999; Moore et al., 1999), which is closely related to the too-big-to-fail problem(Boylan-Kolchin et al., 2011; Papastergis et al., 2015), and on the other

hand postpones first galaxy formation thereby resulting in delay reionization (Marsh and Silk, 2014; Schive et al., 2016). These nice features are not attainable for the WDM model (Macciò et al., 2012). The transition wavenumber, which we call the critical wave number  $k_c$ , is generally smaller than, but of the same order of, the slowly evolving Jeans wave number  $k_J$  of  $\psi$ DM in the matter-dominant era (Hu et al., 2000; Woo and Chiueh, 2009). It is therefore of importance to understand how such a spectral transition occurs dynamically and what makes the connection between  $k_c$  and  $k_J$ .

The evolution of the linear  $\psi$ DM perturbation in the matter-dominant era has been analyzed in (Woo and Chiueh, 2009), in which it gave insights as to why the long-wavelength power resembles to the CDM model and how the short-wave power is suppressed due to the presence of quantum Jeans length. While the perturbation dynamics of matter-dominant regime is straightforward, the dynamics in the radiation-dominant regime is much more complex and must be solved numerically (Hlozek et al., 2015; Marsh, 2016). Unfortunately, the numerical solution offers limited insights to the dynamics. A fluid approach (Marsh, 2016) for sub-horizon perturbations has also been explored, which can be simple enough to permit detailed analyses and sheds some lights on the perturbation dynamics. However, important dynamics that shapes the final spectrum turns out to occur when perturbations are super-horizon where the fluid approach fails. Hence the fluid approach can only partially answer the questions we intend to address.

Note that  $\psi$ DM consists of many free bosons condensed in a quantum ground state, a Bose-Einstein condensate, for which they remain phase coherent over an astronomical distance to share the same wave function. However, there is a problem. Lacking causal contacts, free bosons are not capable of achieving phase coherence. Nonlinearity is needed to make these bosons interact and become phase-locked. In this regard, the axion mechanism offers a plausible solution to the phase-locking problem, for example (Chiueh, 2014; Hui et al., 2017b). The axion model can provide strong boson coupling early on and sets free these bosons at a later time; in other words, the phase-lock mechanism takes place in the very early time and since then these bosons remain phase-coherent even after they become free. Due to this connection to the initial condition of  $\psi$ DM, it is also important

to extend the free-particle model of  $\psi$ DM and examine the axion model.

The axion model, being a nonlinear field model, introduces a second energy scale  $f$ , in addition to  $m$ , where  $f$  is the axion decay constant that is above the GUT scale to explain the cosmic background dark matter mass density to be so close to the cosmic critical density in a non-QCD axion model involving the dark sector(Chiueh, 2014; Davoudiasl and Murphy, 2017; Visinelli, 2017). Indeed, recent developments of string theories also favor extremely light axions with a large axion decay constant  $f$  much greater than the electroweak scale (Svrček and Witten, 2006; Arvanitaki et al., 2010; Diez-Tejedor and Marsh, 2017; Hui et al., 2017a).

However, there is one more free degree of freedom, i.e., the initial field amplitude, which is a dimensionless parameter not present in the field Lagrangian but is able to control the solution. Whether the initial field is located in a linear regime or in a nonlinear regime may make a difference in the solution space and affects the observable. In the context of cosmology, as the universe expands the field amplitude quickly decreases due to the Hubble friction, and soon the field samples only the quadratic part of the potential to become free particle. Hence the free-particle model ( $\psi$ DM) is the ultimate time asymptotic attractor for the axion model and for many other nonlinear scalar field models. One therefore hopes that the Hubble friction may erase the memory of the initial condition, and the solution converges to the free-particle solution.

We numerically investigate perturbations of the axion model to investigate the attractor aspect of the problem, and indeed found that the time-asymptotic solution depends very weakly on the initial angles, except when the axion field starts from very close to the top of the field potential, a highly nonlinear initial field. In such an extreme case, the perturbation begins to behave quite unexpectedly from when the field starts elsewhere. We call this singular case the extreme axion model. This narrow window of new degree of freedom is interesting, and may allows for accommodating the tension concerning the particle mass of  $\psi$ DM determined by the high-redshift Lyman- $\alpha$  forests (Armengaud et al., 2017; Iršič et al., 2017) and by the flat cores of nearby dwarf spheroid galaxies (Lora and Magaña, 2014; Calabrese and Spergel, 2016; Chen et al., 2017).

The organization of this part thesis is as follows. Chapter 8 introduces the relevant equations for later analyses. We also give the fluid formulation from field equations and show that it generally cannot be evolved. Chapter 9 sticks on the free-particle model and provides asymptotic solutions and some physical insights. We examine the axion model and identify its similarities to and differences from the free-particle model in Chapter 10. Conclusions are made in chapter 11. In Appendix B, we give full solution of passive evolution. In contrast to the main text in which we obtain solutions to the approximate equations in various asymptotic phases, we derive in Appendix B approximate solutions to the full solution for the four asymptotic phases. In Appendix C, we turn to addressing equations and analyses for the full treatment of perturbations, including neutrino, baryon and photon perturbations. The particle mass dependence of our results in the extreme axion model is discussed in Appendix D and the general dispersion relation with the Hubble friction is presented in Appendix E.

Throughout the thesis, the fiducial boson mass is chosen  $10^{-22}$  eV, and standard cosmological parameters of the concordance model are adopted, i.e.,  $H_0 = 70\text{km/sec/Mpc}$ ,  $\Omega_{DM} = 0.24$ ,  $\Omega_b = 0.06$ . We also set the speed of light  $c$  and the Planck constant  $\hbar$  equal to 1. Throughout the analysis we adopt the Newtonian gauge for perturbations.



# Chapter 8

## Governing Equations

Standard derivation of the governing equations is given in Appendix B. Here, we provide notations and essential equations to be used in this paper.

Let  $a_*$  and  $H_*$  be the scaling factor and Hubble parameter at some given epoch in the radiation era, and define  $d\tau = dt/a$  and the Hubble parameter  $H \equiv d \ln a / d\tau$ . Since  $H \propto a^{-1}$ , we have  $Ha = H_*a_*$ , a fixed constant, and it follows  $\tau = (H_*a_*)^{-1}a = H^{-1}$ .

Moreover, we decompose the  $\psi$ DM wave function into a time-dependent background  $\Psi(\tau)$  and a space-time dependent perturbation  $\psi$  as usual. The metric perturbation in the Newtonian gauge is denoted as  $\phi$ . The quantities  $\delta_\gamma$  and  $\theta_\gamma$  are the dimensionless energy density perturbation and the velocity potential of the photon fluid. These perturbed quantities in the comoving coordinate are Fourier transformed in space into plane-wave eigenmodes with the comoving wavenumber  $k$  as eigenvalues.

Denote the prime to be  $d/d\tau$ . The zeroth-order field  $\Psi$  obeys

$$\Psi'' + 2H\Psi' + a^2 \frac{dV}{d\psi} \Big|_{\Psi} = 0, \quad (8.1)$$

and the perturbed field  $\psi$  obeys

$$\psi'' + 2H\psi' + (k^2 + a^2 \frac{d^2V}{d\psi^2} \Big|_{\Psi})\psi = 4\Psi'\phi' - 2a^2 \frac{dV}{d\psi} \Big|_{\Psi} \phi. \quad (8.2)$$

Here  $V(\psi)$  is the scalar field potential. The radiation perturbation equations are

$$\delta'_\gamma - \frac{4}{3}(k^2\theta_\gamma + 3\phi') = 0, \quad (8.3)$$

and

$$\theta'_\gamma = -\frac{\delta_\gamma}{4} - \phi, \quad (8.4)$$

where  $\delta_\gamma \equiv \delta\epsilon_\gamma/\epsilon_\gamma$  with  $\epsilon_\gamma$  being the energy density of the radiation fluid, and  $\theta_\gamma$  is the perturbed velocity potential of the radiation fluid. Neutrinos can be regarded as a part of the radiation fluid for super-horizon perturbations. But upon entering horizon, neutrino perturbations die out sharply as a result of their collisionless nature where collisionless damping prevails. In Section 9.2 we have more discussions on this issue.

The equations for the metric perturbation  $\phi$  read

$$-k^2\phi - 3H(\phi' + H\phi) = 4\pi G\{\left[\Psi'\psi' + a^2\frac{dV}{d\psi}\right]_\Psi\psi - (\Psi')^2\phi\} + a^2\epsilon_\gamma\delta_\gamma, \quad (8.5)$$

and

$$\phi' + H\phi = 4\pi G[\Psi'\psi - a^2(\epsilon_\gamma + P_\gamma)\theta_\gamma]. \quad (8.6)$$

One can identify the perturbed energy density as

$$a^2\epsilon_\psi\delta_\psi = \Psi'\psi' + a^2\frac{dV}{d\psi}\Big|_\Psi\psi - (\Psi')^2\phi \quad (8.7)$$

on the right-hand side of Eq. (8.5), where

$$\epsilon_\psi \equiv [(\Psi')^2 + a^2V(\Psi)]/(2a^2). \quad (8.8)$$

One can further substitute Eq. (8.6) into Eq. (8.5) to obtain a simplified equation.

Recognizing the gauge covariant energy perturbation

$$\epsilon_\alpha\Delta_\alpha = \epsilon_\alpha\delta_\alpha - 3H(P_\alpha + \epsilon_\alpha)\theta_\alpha, \quad \alpha = \gamma, \psi, \quad (8.9)$$



and the momentum potential

$$\theta_\psi = -\frac{\Psi' \psi}{a^2(P_\psi + \epsilon_\psi)}, \quad (8.10)$$

with

$$P_\psi \equiv [(\Psi')^2 - a^2 V(\Psi)]/(2a^2), \quad (8.11)$$

it follows that Eq. (8.5) becomes

$$-k^2 \phi = 4\pi G a^2 (\epsilon_\psi \Delta_\psi + \epsilon_\gamma \Delta_\gamma). \quad (8.12)$$

The Poisson equation with gauge covariant sources is recovered.

Although the fluid description of  $\psi$ DM is not useful in general, it is illuminating to find out its difference from that of CDM. We multiply Eq. (8.2) by  $a\Psi'$  and add Eq. (8.1) multiplied by  $a\psi'$ . As the perturbed pressure as

$$\delta P_\psi = a^{-2} \Psi' \psi' - \frac{dV}{d\psi} \Big|_\Psi \psi - a^{-2} (\Psi')^2 \phi, \quad (8.13)$$

we find the perturbed energy equation

$$\delta'_\psi + [\ln(a^3 \epsilon_\psi)]' \delta_\psi + 3H \frac{\delta P_\psi}{\epsilon_\psi} - (1 + \frac{P_\psi}{\epsilon_\psi})(k^2 \theta_\psi + 3\phi') = 0. \quad (8.14)$$

For the perturbed momentum equation, we multiply Eq. (8.1) by  $\psi$  and obtain

$$\theta'_\psi + \{\ln[(P_\psi + \epsilon_\psi)a^4]\}' \theta_\psi = -\frac{\delta P_\psi}{P_\psi + \epsilon_\psi} - \phi. \quad (8.15)$$

Equations (8.14) and (8.15) are actually quite general and valid for any standard field potential. They become the radiation fluid perturbations when  $(\delta P, P) = (1/3)(\epsilon\delta, \epsilon)$  with  $\epsilon \propto a^{-4}$  and also the CDM perturbations when  $\delta P = P = 0$  with  $\epsilon \propto a^{-3}$ , where the " $\psi$ " index is replaced by the photon index and the CDM index, respectively. Note that Eqs. (8.14) and (8.15) need equations of state to relate  $P$  to  $\epsilon$  and  $\delta P$  to  $\epsilon\delta$ . These relations are readily available for standard fluids, but generally far from trivial here. In fact, one must solve the zero-order and perturbed field equations, Eqs. (8.1) and (8.2), to construct

$P_\psi$  and  $\delta P_\psi$  expressed in terms of  $\epsilon_\psi$  and  $\delta\epsilon_\psi$ . Therefore without solving for the field, the fluid description of the field is generally of no practical use.





# Chapter 9

## Free Particle Model

In this chapter, we stick on the scalar field potential with the quadratic form, i.e.,  $V(\psi) = m^2\psi^2/2$ . The scalar field with the quadratic potential is also called "Free particle model", in which there is no self-interaction among dark matter particles. This model is the simplest case and it can give some physical insight of the evolution process once the dark matter is described by this kind of the scalar field.

### 9.1 Passive Evolution and Asymptotic Solutions

Passive evolution of dark matter can be a good approximation of the dark matter dynamics in the radiation-dominant era, where the metric perturbation is governed entirely by the radiation fluid, which includes neutrinos. Neutrinos are actually collisionless particles, and their perturbations behave identical to radiation perturbations before entering horizon but die out rapidly once they enter horizon (Ma and Bertschinger, 1995). We approximate neutrinos always as a part of the radiation fluid for passive evolution, and will show in the next section that this crude treatment is still a good approximation for dark matter perturbations of main interest.

The right-hand side of Eq. (8.2) can thus be approximated as external sources independent of  $\psi$  for passive evolution. This assumption greatly simplifies the following asymptotic analyses, bringing out the details of the differences between the CDM perturbation and the  $\psi$ DM perturbation caused by the introduction of a finite particle mass  $m$ .

in Eq. (8.2). In the limit of  $m \rightarrow \infty$ , the  $\psi$ DM perturbation should recover the CDM result. With this approach, analytical expressions for source terms in Eq. (8.2) can actually be obtained and therefore the solution  $\psi$  can be integrated by the Green's function method. The full solution however involves confluent hypergeometric functions and is not illuminating to be given in the main text, and hence we present it in Appendix B.

Plotted in Fig. (9.1) is the passive time evolutions of two distinct modes with mode numbers  $k = 0.1k_c$  and  $k = 10k_c$ , where  $k_c$  is the wave number of the critical mode that enters horizon at the onset of mass oscillation. (More discussions on  $k_c$  are given in Section 9.3.) There exist four asymptotic phases of evolution as shown in Fig. (9.1), and this plot sets the stage for discussions to follow.

The evolution of  $\psi$ DM perturbations has a natural dividing line, the onset of mass oscillation. Prior to the mass oscillation,  $\psi$ DM is like an inflaton and after that,  $\psi$ DM is like CDM influenced to various degrees by the additional quantum pressure. Since the latter is closely resembled the familiar CDM, we shall discuss the second phase first. Little surprise arises in the second phase, given that we know the perturbed  $\psi$ DM dynamics in the matter-dominant era (Woo and Chiueh, 2009). The new features of  $\psi$ DM is actually given by the earlier phase prior to mass oscillation, resulting in a sharp transition of the  $\psi$ DM spectrum.

### 9.1.1 Phase (i): After mass oscillation $2H, k \ll ma$

For long wave ( $k \ll ma$ ) perturbations well after the onset of mass oscillation,  $ma \gg 2H$ , the dynamical system is like a driven damped oscillator near resonance, with the main frequency  $m$  and detuning frequency  $k$ . Equation (8.2) can be simplified by extracting the common mass oscillation factor in all terms and is approximated by a complex amplitude equation, for which the detuning frequency  $k$  appears in the equation. The simplification procedure goes as follows. Let  $\psi \equiv A\Psi_r + B\Psi_s$ , where  $\Psi_r$ , the regular solution of  $\Psi$ , and  $\Psi_s$ , the singular solution that diverges at  $\tau \rightarrow 0$ , are given in Appendix B,  $A$  and  $B$  are real fields with slow time variations, and the zero-order field  $\Psi = \Psi_r$ . To the accuracy of  $O(2H/ma)$ ,  $(\Psi_r, \Psi'_r/ma) \sim (2\epsilon_\psi/m^2)^{1/2}(\cos(mt - q + \alpha) + O(H^2/m^2a^2), -\sin(mt +$

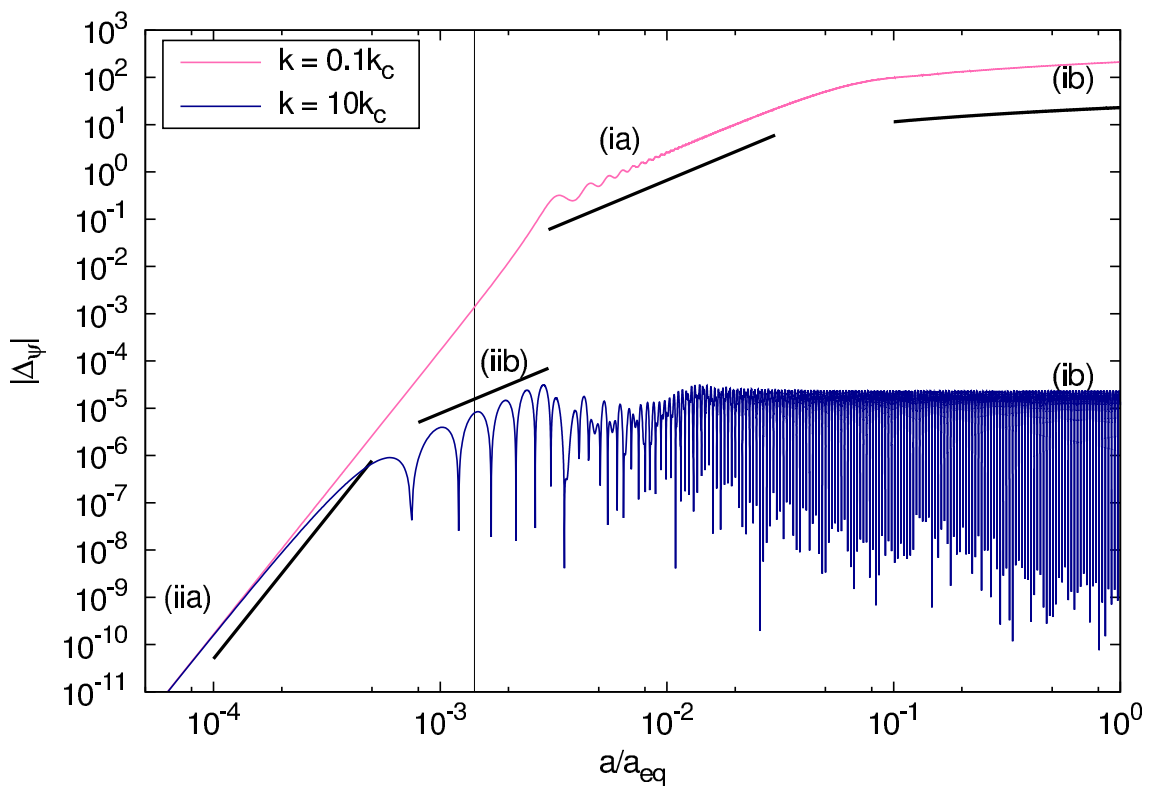


Figure 9.1: Two cases of gauge covariant  $\psi$ DM energy density perturbations  $\Delta_\psi$  with passive evolution for the very long and very short wave modes. The horizontal axis is  $a/a_{eq}$  where  $a_{eq}$  is the scale factor at radiation-matter equality, and the particle mass is chosen to be  $10^{-22}\text{eV}$ . There are four asymptotic phases as labeled. The vertical line marks the beginning of mass oscillation. The bold lines have log-slopes 6, 2,  $\sim 0$ , respectively from left to right.

$7q + \alpha) + O(H^2/m^2a^2)$ ), with  $\alpha$  being a constant phase and  $q = 3H/16ma \propto 1/t$ , and  $(\Psi_s, \Psi'_s/ma) \sim (2\epsilon_\psi/m^2)^{1/2}(\sin(mt - q + \alpha) + O(H^2/m^2a^2), \cos(mt + 7q + \alpha) + O(H^2/m^2a^2))$ . One may further define a complex  $\hat{\psi}$ , where  $\hat{\psi} = A + iB$ , and therefore  $\psi = \text{Re}[\hat{\psi}(\Psi_r - i\Psi_s)] \rightarrow (2\epsilon_\psi/m^2)^{1/2}\Re[\hat{\psi} \exp(-i(mt + \alpha))]$  in the limit  $H/ma \rightarrow 0$ .

The amplitude  $\hat{\psi}$  equation can be straightforwardly derived from Eq. (8.2),

$$-i\hat{\psi}' + \frac{k^2}{2ma}\hat{\psi} = -ma\phi. \quad (9.1)$$

This equation is the familiar linearized Schrödinger equation for the perturbed field.

Note that in order for Eq. (9.1) to be correctly derived, it is essential to keep the small  $q$  in  $\Psi_r$  and  $\Psi_s$ . Otherwise, there would be additional incorrect terms of order  $O(H^2\hat{\psi})$  appearing in Eq. (9.1), which would have otherwise given an erroneous solution for Phase (ia).

Eq. (9.1) is driven by a source proportional to  $\phi$ , and the solution consists of a particular integral and a homogeneous solution. The adiabatic perturbation, which is of interest to us, corresponds to the particular integral of the full equation, Eq. (8.2). For the asymptotic regimes to be discussed below, certain limits have been taken to simplify the full equation, but this simplification comes with a cost, in decomposing the particular integral of the full equation into the particular integral and the homogeneous solution of the simplified equation. The homogeneous solution can be regarded as the initial condition of the solution to the simplified equation and assumes a undetermined amplitude, which needs to be fixed by some means, for example, matching to the solution in the previous phase.

### Phase (ia): $k \ll 2H \ll ma$

In this regime, the term proportional to  $k^2$  in Eq. (9.1) can be ignored to the leading order. Now, as the super-horizon metrics perturbation  $\phi = \phi_0[1 - (1/30)(k/H)^2 + O(k^4/H^4)]$  where  $\phi_0$  is a constant (shown in Appendix B), the driving source in the real part of Eq. (9.1) grows as  $a$ . Thus the particular integral solution  $\Im[\hat{\psi}]_p = -(ma/2H)\phi_0 \propto a^2$ , and  $\Re[\hat{\psi}]_p = 0$ . On the other hand the homogeneous solution,  $\hat{\psi}_h$ , of Eq. (9.1) is a complex constant.



To the leading order, we have

$$\delta_\psi = 2\Re[\hat{\psi}] + \frac{3H}{ma}[2\sin^2(mt+\alpha) - 1]\Im[\hat{\psi}] \quad (9.2)$$

(c.f. Eq. (8.7)), where  $\Im[\hat{\psi}]' = -ma\phi_0$  has been used. The quantity  $\Re[\hat{\psi}]$  is an arbitrary homogeneous solution  $\Re[\hat{\psi}]_h$ , and  $\Im[\hat{\psi}]$  is a combination of the particular integral and a constant homogeneous solution. Finally, the covariant energy perturbation

$$\Delta_\psi = \delta_\psi - \frac{6H}{ma}\Im[\hat{\psi}]\sin^2(mt+\alpha) = 2\Re[\hat{\psi}] - \frac{3H}{ma}\Im[\hat{\psi}]. \quad (9.3)$$

Note that while the gauge-dependent  $\delta_\psi$  oscillates, the gauge-covariant  $\Delta_\psi$  manifestly does not.

It requires some guidance to fix the homogeneous solution  $\hat{\psi}_h$  in Eq. (9.3). Conventionally, matching of solutions in different asymptotic regimes can provide such guidance. However we adopt a different approach here. For super-horizon adiabatic perturbation,  $\delta_\psi$  obeys the relation:

$$\frac{\langle \delta_i \rangle}{\langle 1 + w_i \rangle} = \frac{\langle \delta_j \rangle}{\langle 1 + w_j \rangle} \quad (9.4)$$

for any species  $i$  and  $j$ , where we denote  $\langle \dots \rangle$  to represent a short-time average to filter out the fast mass oscillation. (However, see Section 9.4.) It follows  $\langle \delta_\psi \rangle = (3/4)\delta_\gamma$ . From Appendix B, we also know that  $\delta_\gamma \sim -2\phi_0$  and hence  $\langle \delta_\psi \rangle \sim -(3/2)\phi_0$ . Therefore the constant  $\Re[\hat{\psi}]_h = -(3/4)\phi_0$ . Given  $\Im[\hat{\psi}]_p = -(ma/2H)\phi_0$ , we find

$$\Delta_\psi = -\frac{3H}{ma}\Im[\hat{\psi}]_h. \quad (9.5)$$

The  $\phi$  dependence in  $\Delta_\psi$  cancels and only the arbitrary homogeneous solution  $\Im[\hat{\psi}]_h$  survives.

If  $\Im[\hat{\psi}]_h \sim O(\Re[\hat{\psi}]_h)$ , the remaining term of  $\Delta_\psi$  is a small quantity of order  $2H/ma$  and decays as  $a^{-2}$ , thus negligible. From the definition of  $\hat{\psi}$ , the imaginary part  $\Im[\hat{\psi}]$  is to be multiplied by  $\Psi_s$  and the real part  $\Re[\hat{\psi}]$  by  $\Psi_r$  to yield the original field  $\psi$ . The ratio  $\Psi_s/\Psi_r$  diverges in early epoches when  $2H/ma \rightarrow \infty$ , and the ratio  $\Im[\hat{\psi}]/\Re[\hat{\psi}]$  in early

time must approach zero. Therefore at the onset of mass oscillation  $2H = ma$  immediately before the perturbation enters the present phase, which is the main contribution of the homogeneous solution, the quantity  $\Im[\hat{\psi}]_h$  is at most of the same order of  $\Re[\hat{\psi}]_h$ . In Appendix B, we show that  $\Im[\hat{\psi}]_h$  is in fact of higher-order smallness compared to  $\Re[\hat{\psi}]_h$ . Therefore the gauge-covariant  $\Delta_\psi$  cancels itself to the leading order ( $O(1)\phi_0$ ), and we must consider the next-order contributions to  $\Delta_\psi$ .

In this phase, there are two types of high-order terms,  $O(2H/ma)$  and  $O((k/H)^2)$ . The former decays as  $a^{-2}$  and the latter grows as  $a^2$ . We shall consider the latter. The next order contributions to  $\Delta_\psi$  arise from all other terms in Eq. (8.2) but are neglected in Eq. (9.1).

A straightforward but lengthy calculation by keeping all terms of order  $O(k^2/H^2)$  in Eq. (8.2) reveals that  $\Re[\hat{\psi}]_p = -(7/40)(k/H)^2\phi_0$  and  $\Im[\hat{\psi}]_p = -(ma/2H)\phi_0(1 - (1/60)(k/H)^2)$ . The homogeneous solution  $\Re[\hat{\psi}]_h = -(3/4)\phi_0(1 + O((k/H)^2(H/ma)))$  and remains the same as before to the order in question; so is  $\Im[\hat{\psi}]_h$ . Substituting the above findings to the second equality of Eq. (9.3), we now have  $\Delta_\psi = -(3/8)(k/H)^2\phi_0 = (9/16)\Delta_\gamma \propto a^2$ , where the Poisson's equation (Eq. (8.12)) has been used to bring out  $\Delta_\gamma$ .

The  $\psi$ DM gauge-covariant energy perturbation in this phase is identical to the CDM counterpart, for which the growth is independent of the particle mass  $m$ . Note that the perturbed field goes through this phase only for sufficiently low- $k$  modes. Modes with sufficiently high- $k$  skip this phase and directly enter Phase (ib) to be discussed below.

### **Phase (ib): $2H \ll k \ll ma$**

In this regime, the pressure perturbation can be of dynamical importance despite  $\langle P_\psi \rangle = 0$ . Here,  $\langle \delta P_\psi \rangle = (\epsilon_\psi/ma)\Re[i\hat{\psi}' - ma\phi]$  from Eq. (8.13). Compared with the real part of Eq. (9.1), one readily recognizes that

$$\langle \delta P_\psi \rangle = \frac{k^2}{2m^2a^2}\epsilon_\psi(\Re[\hat{\psi}]) \approx \frac{k^2}{4m^2a^2}\epsilon_\psi\langle \delta_\psi \rangle. \quad (9.6)$$

The second equality of Eq. (9.6) holds because the term proportional to the metric perturbation  $\phi$  in  $\delta_\psi$  is a high-order term and can be ignored. Now that with  $\langle \delta P_\psi \rangle$  available, the

dynamics of perturbation in the sub-horizon regime can be described by fluid equations.

As  $\epsilon_\psi \langle \delta_\psi \rangle \gg \langle \delta P_\psi \rangle$ , we seem to recover CDM. But it is not so even when  $k^2 \ll m^2 a^2$ , since this inequality is only an indication of  $\psi$ DM becoming non-relativistic. Non-relativistic dark matter can nevertheless have sufficiently large pressure to counter the gravity for short waves. Hence only in the long wave limit of this regime  $k^2 \ll (m^2 a^2)(2H/m a)$  can  $\psi$ DM perturbations resemble CDM perturbations, as we shall see below.

In discussions to follow, we shall stick to the field equation for consistency, despite that the fluid equations are also well-defined. In this regime the metric perturbation  $\phi \sim \phi_0(H/k)^2 \cos(k(\tau - \tau_k)/\sqrt{3})$  as discussed in Appendix B, where  $\tau_k$  is the instant for mode  $k$  to enter horizon. Therefore the driving source ( $\propto \phi$ ) of Eq. (9.1) is of order  $O(a^{-1})$ . It is straightforward to find that the particular integrals  $\Re[\hat{\psi}]_p \sim \phi_0(3/2)(H/k)^2 \cos(k(\tau - \tau_k)/\sqrt{3})$  and  $\Im[\hat{\psi}]_p \sim -\phi_0(\sqrt{3}maH^2/k^3) \sin(k(\tau - \tau_k)/\sqrt{3})$ , which decay as  $a^{-2}$  and  $a^{-1}$ , respectively, and can be ignored.

On the other hand, the homogeneous solution derived below exhibits constant-amplitude oscillations and will dominate the particular integral. It is convenient to choose the reference epoch  $a_* = a_m$  and  $H_* = H_m$ , where  $a_m$  and  $H_m$  refer to the expansion factor and Hubble parameter at  $2H = ma$ , or  $H_m \equiv ma_m/2$ . Multiplying Eq. (9.1) by  $a$ , we can change the time variable to a dimensionless  $\eta = \ln(a/a_m) \equiv \ln(H_m \tau)$ . Equation (9.1) can be cast into

$$-i \frac{d\hat{\psi}_h}{d\eta} + \frac{k^2}{4H_m^2} \hat{\psi}_h = 0. \quad (9.7)$$

This equation admits the homogeneous solution  $\hat{\psi}_h = g \exp[i(k^2/4H_m^2)(\eta - \eta_k)]$  with  $g$  being a complex constant and  $\eta_k = \ln(a_k/a_m)$  denoting the duration between the onset of mass oscillation and when mode  $k$  enters horizon. The homogeneous solution is oscillating with a constant amplitude and dominates the particular integral for  $a \gg a_k$ . Thus the perturbed field  $\hat{\psi}$  decouples from the gravity in this regime and becomes a free matter wave with a constant frequency  $k^2/4H_m^2$  in the  $\eta$  space.

In the long-wave limit, where  $k^2/4H_m^2 \ll 1$ , we can estimate the complex constant  $g$  by matching the solution to Phase (ia), which has a constant  $\Re[\hat{\psi}] \sim O(1)\phi_0$  and a growing  $\Im[\hat{\psi}] \sim O(ma/H)\phi_0 (>> \Re[\hat{\psi}])$ . We therefore expect that in the limit of small  $\eta - \eta_k$  in the

present phase,  $\Re[\hat{\psi}] \ll \Im[\hat{\psi}]$ . This is only possible when  $\Re[\hat{\psi}] \propto \sin[(k^2/4H_m^2)(\eta - \eta_k)]$  and  $\Im[\hat{\psi}] \propto \cos[(k^2/4H_m^2)(\eta - \eta_k)]$ . That is,  $g$  is pure imaginary. Moreover, we can also estimate that  $|g| \sim O(H_m^2/k^2)\phi_0$ , obtained from the small argument expansion of  $\sin[(k^2/4H_m^2)(\eta - \eta_k)]$  for  $\Re[\hat{\psi}]$ . This estimate of  $|g|$  is also consistent with  $\Im[\hat{\psi}]$  at the end of Phase (ia) when  $k \rightarrow H$ , since the factor  $ma/H = maH/H^2 \rightarrow H_m^2/2k^2$ .

To fix the value of  $|g|$ , we use the CDM limit in Appendix B with  $H/ma \rightarrow 0$ . The CDM covariant energy perturbation is  $\Delta_{CDM} \rightarrow (c_1 - 9(\eta - \eta_k))\phi_0$ , when  $c_1$  is a constant of order unity. On the other hand, the expression of the covariant energy perturbation  $\Delta_\psi$  is the same as Eq. (9.3),

$$\Delta_\psi \sim |g| \left\{ 2 \sin \left[ \frac{k^2}{4H_m^2} (\eta - \eta_k) \right] + \frac{3H}{ma} \cos \left[ \frac{k^2}{4H_m^2} (\eta - \eta_k) \right] \right\}. \quad (9.8)$$

Matching  $\Delta_{CDM}$  and  $\Delta_\psi$  in the limit  $k^2/4H_m^2(\eta - \eta_k) \rightarrow 0$  but  $\eta - \eta_k \gg 1$ , we find that  $|g| = -18(H_m^2/k^2)\phi_0$  from the sine term of  $\Delta_\psi$ . We stress that this result is valid only for long waves, and for short waves  $g$  is generally complex.

Note that all modes, except for the very long-wavelength ones that have not yet entered horizon at the radiation-matter equality, must go through this final phase of the radiation era. Equation (9.1) is also valid in the matter era, and the solution characteristics deviates from the above description since the self-gravity of  $\psi$ DM becomes important. This equation in the matter era has been discussed previously and an analytical solution been obtained (Woo and Chiueh, 2009).

### 9.1.2 Phase (ii): Before mass oscillation

Before mass oscillation, the  $\psi$ DM energy perturbation is always much smaller than the radiation energy perturbation unless particle mass  $m > 10^{-28}$  eV, and hence passive evolution can always be a good approximation throughout this regime. In this regime,  $\Psi$  is almost a constant,  $\Psi' \sim -(m^2 a^2 / 5H)\Psi$ , and hence the equation of state of the zero-order field is like that of an inflaton with  $P_\psi \sim -\epsilon_\psi$ .

**Phase (iia):**  $k \ll 2H$



The super-horizon metric perturbation is again almost a constant, i.e.,  $\phi \sim \phi_0(1 - (1/30)(k^2/H^2) + O(k^4/H^4))$ . The perturbed field equation Eq. (8.2) can be approximated by:

$$\psi'' + 2H\psi' = -2m^2a^2\Psi\phi, \quad (9.9)$$

to the leading order. The three terms originally in Eq. (8.2) ignored in Eq. (9.9) are of order  $O(k^2/H^2)$  or  $O(m^2a^2/H^2)$  compared with other terms retained. Similar to Phase (ia), it turns out that the solution of Eq. (9.9) also yields a  $\Delta_\psi$  that cancels itself to the leading order.

To see the cancellation, we shall find the solution for Eq. (9.9). The particular integral can be easily obtained by substituting  $\psi' \propto (m^2a^2/H)\Psi\phi$  into Eq. (9.9) and it follows that  $\psi_p \sim -(m^2a^2/10H^2)\Psi\phi_0$ . The homogeneous solution decays as  $\psi' \sim a^{-2}$  or  $\psi' = 0$ , and can be ignored. The energy perturbation for the particular integral becomes  $\delta_\psi \sim (-3/25)(ma/H)^2\phi_0$ . On the other hand from Eq. (8.10),  $\Psi'\psi \sim (1/25H)(ma/H)^2(m^2a^2\Psi^2/2)\phi_0$ , and thus the gauge covariant energy perturbation  $\Delta_\psi$  exactly cancels to the leading order of  $a^4$ .

All corrections of to  $\psi_p$ , and therefore  $\Delta_\psi$ , are integer powers of  $(k/H)^2$  as only  $k^2$  appears in the original equation, Eq.(8.2). Thus,  $\Delta_\psi \sim O((k/H)^2\delta_\psi) \sim O((k/H)^2(ma \times H^{-1})^2\phi_0) \sim O((ma/H)^2)\Delta_\gamma \propto a^6$ . Here we have again employed the Poisson equation to relate  $\Delta_\psi$  to  $\Delta_\gamma$ .

The  $a^6$  rapid growth in this phase is drastically different from the CDM perturbation ( $\propto a^2$ ), and it is the main cause of the sharp cutoff in the matter power spectrum near a critical  $k$  to be discussed in the next section. Moreover, this  $a^6$  rapid growth occurs regardless of whether  $k > ma$  or  $ma > k$  and modes of all  $k$  must go through this initial phase.

**Phase (iib):**  $ma \ll 2H \ll k$

In this regime, the background field is still like an inflaton, where the background energy density is dominated by the field potential energy. Same as Phase (ib), the sub-horizon metric perturbation undergoes a damped oscillation, i.e.,  $\phi \sim \phi_0(H/k)^2 \cos(k(\tau - \tau_k)/\sqrt{3}) \propto a^{-2}$ . This source drives the perturbed field to also oscillate with the same frequency. However, unlike Phase (ia), the driving frequency  $k/\sqrt{3}$  is different from the natural frequency  $k$  of the  $\psi$ DM perturbation, resonance is impossible and hence the treatment is different from Phase (ia).

The source now is dominated by  $\Psi'\phi' \sim (k/5\sqrt{3}H)(m^2a^2)\Psi\phi_0 \sin(k(\tau - \tau_k)/\sqrt{3})$  and is  $\propto a$ . Hence the particular integral to the approximate equation

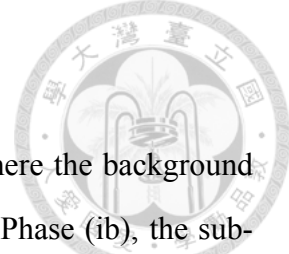
$$\psi'' + k^2\psi = 4\Psi'\phi' \quad (9.10)$$

is  $\psi_p \sim 6\Psi'\phi'/k^2 \sim O((m^2a^2/kH)\phi\Psi) \propto a \sin(k(\tau - \tau_k)/\sqrt{3})$ . The energy perturbation  $\delta_\psi \sim 2(\psi'\Psi' - (\Psi')^2\phi)/m^2a^2\Psi^2 \sim O((ma/H)^2\phi) \sim O((ma/k)^2\Delta_\gamma) \propto a^2$ . The gauge-covariant energy perturbation  $\Delta_\psi$  differs from  $\delta_\psi$  by a high-order term  $O(H/k)$  smaller, and therefore  $\Delta_\psi \sim \delta_\psi$ , growing as  $a^2$  in the oscillation amplitude.

Note that only for sufficiently large  $k$  can a mode enter Phase (iib), and after that it skips Phase (ia) to go directly to Phase (ib). For a mode of low  $k$ , it initially goes through Phase (iia) and skips this phase to enter Phase (ia) and then (ib).

## 9.2 Evolution of Perturbations in Full Treatment

Full treatment of perturbations in the radiation-dominated era must take into account several effects beyond the passive evolution, namely, the decoupling of neutrino after entering horizon, the relative drag between baryons and photons, the non-negligible baryon component in the photon fluid energy density, and the self-gravity of matter. The last three become significant only near the radiation-matter equality.





### 9.2.1 Neutrino Decoupling

After entering horizon  $k \geq 2H$ , photon fluid perturbations oscillate with a constant amplitude indefinitely until the effect of baryon-photon drag sets in. On the other hand, neutrino perturbations oscillate along with photon fluid perturbations in the first half cycle of oscillation, and after crossing the first null neutrino perturbations are abruptly damped out due to free streaming (Ma and Bertschinger, 1995). We therefore set neutrino density perturbations to zero immediately after its first oscillation null, as an approximation to solve for perturbations of the rest of surviving species. Thus, we let

$$\Delta_\nu = \begin{cases} \Delta_{ph}, & \tau \leq \tau_1, \\ 0, & \tau > \tau_1, \end{cases} \quad (9.11)$$

where  $\Delta_\gamma \equiv \Delta_{ph} + \Delta_\nu$ , and  $\Delta_\nu$  and  $\Delta_{ph}$  are neutrino and photon covariant perturbed energy densities, respectively;  $\tau_1$  is the conformal time of the first oscillation null of  $\Delta_\gamma$ .

### 9.2.2 Photon Fluid Equation of State

In between the end of radiation-dominant era,  $a = a_{eq}$ , and the onset of photon-electron decoupling,  $a \approx 3a_{eq}$ , baryons can be non-negligible in modifying the equation of state parameter for the photon fluid, i.e.,

$$w_{ph} \equiv \frac{P_{ph} + P_b}{\epsilon_{ph} + \epsilon_b} = \frac{a_{eq}}{3 \left( a_{eq} + a \frac{\Omega_b}{\Omega_m} \frac{\Omega_{ph} + \Omega_\nu}{\Omega_{ph}} \right)}. \quad (9.12)$$

According to the current values  $\Omega_b \approx 0.05$ ,  $\Omega_m = \Omega_{dm} + \Omega_b \approx 0.316$  and  $(\Omega_{ph} + \Omega_\nu)/\Omega_{ph} \approx 1.7$  (Ade et al., 2016), the value of  $w_{ph}$  approximately equals 20/77 and 20/111 when evaluated at the radiation-matter equality and at immediately before photon-electron decoupling, respectively.

In practice, we should not consider a single coupled photon+baryon fluid, but should keep track of photon and baryon perturbations separately for the reason given below. Their respective density equations and coupled momentum equations through Thomson scatter-



ing are

$$\delta'_{ph} - \frac{4}{3}(k^2\theta_{ph} + 3\phi') = 0, \quad (9.13)$$

$$\theta'_{ph} = -\frac{\delta P_{ph}}{\epsilon_{ph} + P_{ph}} - \phi + an_e\sigma_T(\theta_b - \theta_{ph}), \quad (9.14)$$

$$\delta'_b = k^2\theta_b + 3\phi', \quad (9.15)$$

and

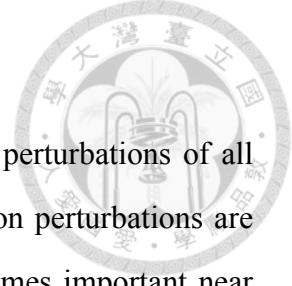
$$\theta'_b = -H\theta_b - \phi - \frac{4\epsilon_{ph}}{3\epsilon_b}an_e\sigma_T(\theta_b - \theta_{ph}). \quad (9.16)$$

Here  $n_e$  is the electron number density and  $\sigma_T$  is the Thomson scattering cross section.

### 9.2.3 Baryon-Photon Drag

Thomson scattering that couples photons and baryons can be characterized by a scattering mean-free-path  $l_T \equiv (n_e\sigma_T a)^{-1}$ . After the photon perturbation enters horizon, the wave number  $k$  becomes a relevant scale. Here, we can have a length ratio,  $kl_T \propto a^2$ . When  $kl_T \ll 1$ , the photon perturbation is efficiently coupled to baryons, and photons are well-described by a fluid. However, there is another length ratio  $(k/2H)(kl_T) \propto a^3$  that is larger than  $kl_T$  and becomes greater than unity earlier than  $kl_T$  does after perturbations entering horizon. The new length scale ratio characterizes when the phase lag between the oscillation of baryon and the oscillation of photon becomes so severe that both photon and baryon perturbations are rapidly damped when  $(k/H)(kl_T) > 1$ . Physically, photons undergo random walks due to Thomson scattering, and in a Hubble time  $H^{-1}$  the random walk distance is  $(l_T/H)^{1/2}$ . When this distance is larger than the wavelength, the drag damping can occur (Hu and Sugiyama, 1996). In the wave number range of interest to the present work,  $k \sim O(k_c)$ , we find  $(k/2H)(kl_T) \sim O(1)$  near the radiation-matter equality and the drag damping just begins to take effect. At this moment, we still have  $kl_T \ll 1$  and the photon fluid is a good description and it justifies the photon momentum equation Eq. (9.14).

### 9.2.4 Matter Self-Gravity



In the full treatment, the source of Poisson equation contains perturbations of all species, to be contrasted with passive evolution where only radiation perturbations are the only source of Poisson equation. The matter gravity only becomes important near the radiation-matter equality, where the self-gravity prolongs the matter-wave oscillation cycle and slightly modifies the  $\psi$ DM power spectrum.

A fourth order Runge-Kutta scheme is adopted for integrating the background equations (Eqs. (8.1) and Friedmann equations described in Appendix C, i.e., Eqs. (C.1) and (C.2), with equations of states) and the perturbed equations (Eqs. (8.2), (9.13), (9.14), (9.15), (9.16) and perturbed Einstein equations described in Appendix C, i.e., Eqs. (C.3) and (C.4), with the neutrino contribution given in Eqs. (C.5) and (C.6)). Plotted with dotted lines in Fig. (9.2) are the numerical solutions of the covariant energy perturbations  $\Delta_\psi$  for full treatment as functions of the scaling factor  $a/a_{eq}$  for particle mass  $m = 10^{-22}\text{eV}$ . We have chosen modes with  $k \gg k_c$  and  $k \ll k_c$  to illustrate the difference. The vertical solid line marks the onset of mass oscillations ( $a = a_m$ ). The three asymptotic phases discussed in the last section are clearly shown in Fig. (9.2) for the low- $k$  mode and the other three for higher- $k$  mode. Solutions of passive evolution are also plotted as solid lines in Fig. (9.2) for comparison. One notices that the full treatment and the passive evolution deviate from each other only near the radiation-matter equality, indicative of the slowing down of matter-wave oscillation due to the matter self-gravity. It is not surprising to find that treating neutrinos as a fluid for passive evolution does not differ from a more sophisticated approximation for neutrinos in the full treatment, as long as  $k$  is smaller than  $k_c$ . This is due to that sub-horizon perturbations of these low- $k$  modes are hardly coupled to metric perturbations (Phase(ib)). Noticeable differences occur only for  $k > k_c$  since these modes respond to photon oscillations driven by metric perturbations after entering horizon (Phase(iib)), and a decrement in the metric perturbation due to the vanishing neutrino contribution decreases the oscillation amplitude. These high- $k$  modes, however, have vanishingly small power at the radiation-matter equality and hence the differences

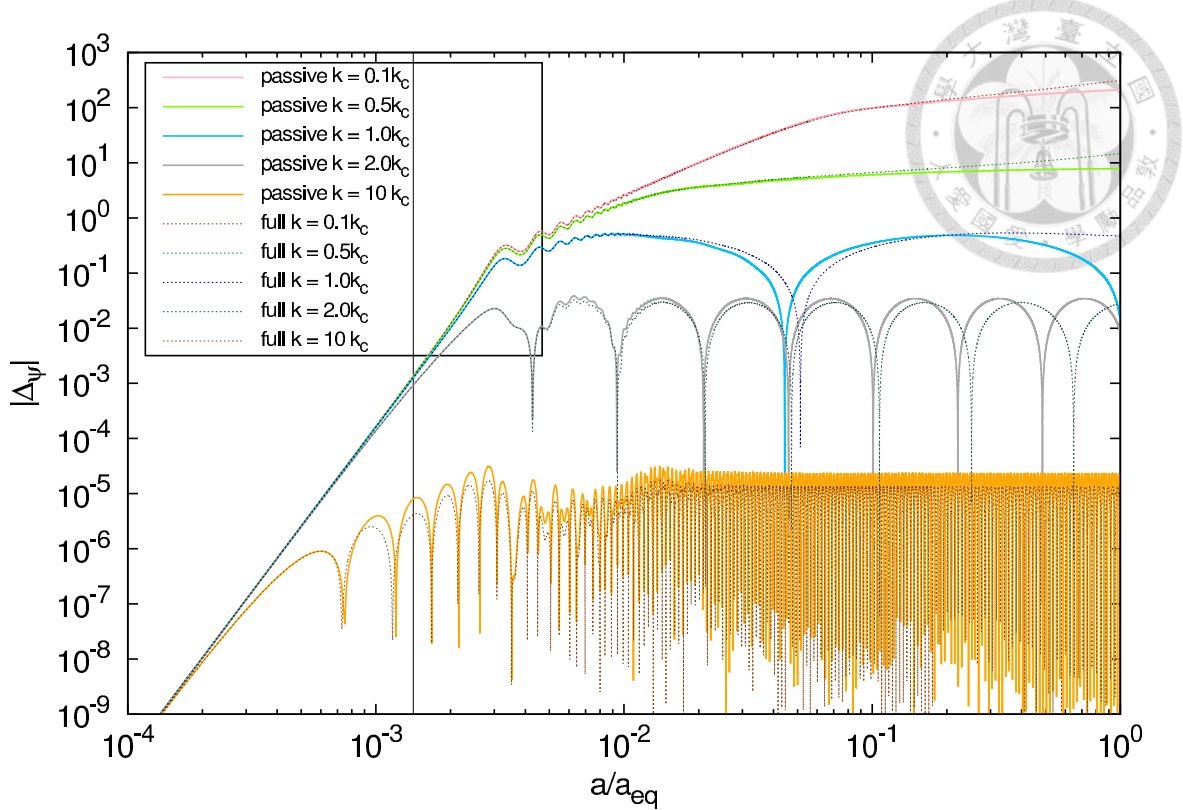


Figure 9.2: Passive evolution and full treatment of gauge covariant  $\psi$ DM energy density perturbations for several different  $k$ 's. The full treatments (dotted lines) deviate from the passive evolution (solid lines) only near the epoch of radiation-matter equality except for very high- $k$  modes, as explained in the text.

are insignificant for practical purposes.

In Appendix C, we show in detail how the photon fluid and the baryon fluid, coupled by the relative drag, evolve in the full treatment. To summarize, passive evolution of  $\psi$ DM captures most essential physics in the evolution of full treatment. Hence we shall continue to take advantage of the understanding gained from passive evolution for the following discussions.

### 9.3 Critical Mode, Matter Power Spectrum and Sub-Horizon Dynamics

We saw in the previous discussions that high- $k$  modes go through Phases (iia), (iib) and (ib), and low- $k$  modes go through Phase (iia), (ia) and (ib). In between the two, there exists a critical  $k_c$  mode crudely defined as  $k_c = ma_m = 2H_m = (2H_m m a_m)^{1/2} =$

$(2Hma)^{1/2}$ , a redshift-independent wave number, that characterizes a transition. This particular mode enters horizon at the moment when the mass oscillation starts, and so the mode can be viewed as having a wavelength equal to the Compton wavelength when  $\psi$ DM is crystallized into a real particle. For modes of  $k < k_c$ , they have wavelengths greater than the Compton length ever since the particle becomes real; for modes of  $k > k_c$ , there is a finite period after the particle becomes real where their wavelengths are smaller than the Compton length. One expects that structures smaller than the Compton length can hardly exist and hence must be suppressed. This is indeed what we saw in the drastically different dynamics for modes of  $k < k_c$  and  $k > k_c$ .

Plotted in Fig. (9.3) are the  $\psi$ DM transfer function in reference to CDM,  $(\Delta_\psi/\Delta_{CDM})^2$ , evaluated at  $a_{eq}$  as functions of  $k$  with particle mass,  $m = 10^{-22}\text{eV}$ . The solid line denotes the passive evolution and the dashed line the full treatment. Comparison of the two curves shows minor ( $< 10\%$ ) differences for  $k < k_c/2$ , demonstrating the passive evolution is a good approximation for the entire radiation-dominant era for these long waves. For  $k > k_c/2$ , our discussion about the mode suppression still holds and details are given below. In addition, Fig. (9.3) exhibits substantially different oscillation phases for the two (passive versus full treatment) evolutionary paths. This is caused by the self-gravity in full treatment that lowers the matter-wave oscillation frequency. But the self-gravity comes to play late in the evolution, and hence little affects our dynamical picture of Phase (ib).

In Fig. (9.3), we also provide the power spectrum evaluated at  $2.5a_{eq}$ , serving as the initial condition for any calculation starting in the matter-dominated era.

Below, we shall explain how the short-wave suppression occurs more quantitatively. All modes first follow the rapid  $a^6$  growth of phase (iia). Modes with  $k < k_c$  continue this growth until the mass oscillation starts at  $a = a_m$ , and then they follow the CDM growth before entering horizon. Modes with  $k > k_c$  exit the rapid growth of Phase (iia) early on when becoming sub-horizon and enter the slower  $a^2 \cos(k(\tau - \tau_k))$  growth of Phase (iib) before mass oscillation, and after mass oscillation, they enter Phase (ib) directly without going through the CDM phase, Phase (ia). Hence, these high- $k$  modes never have a chance to resemble CDM perturbations. The amplitudes differ roughly by  $(k_c/k)^4$  for modes with

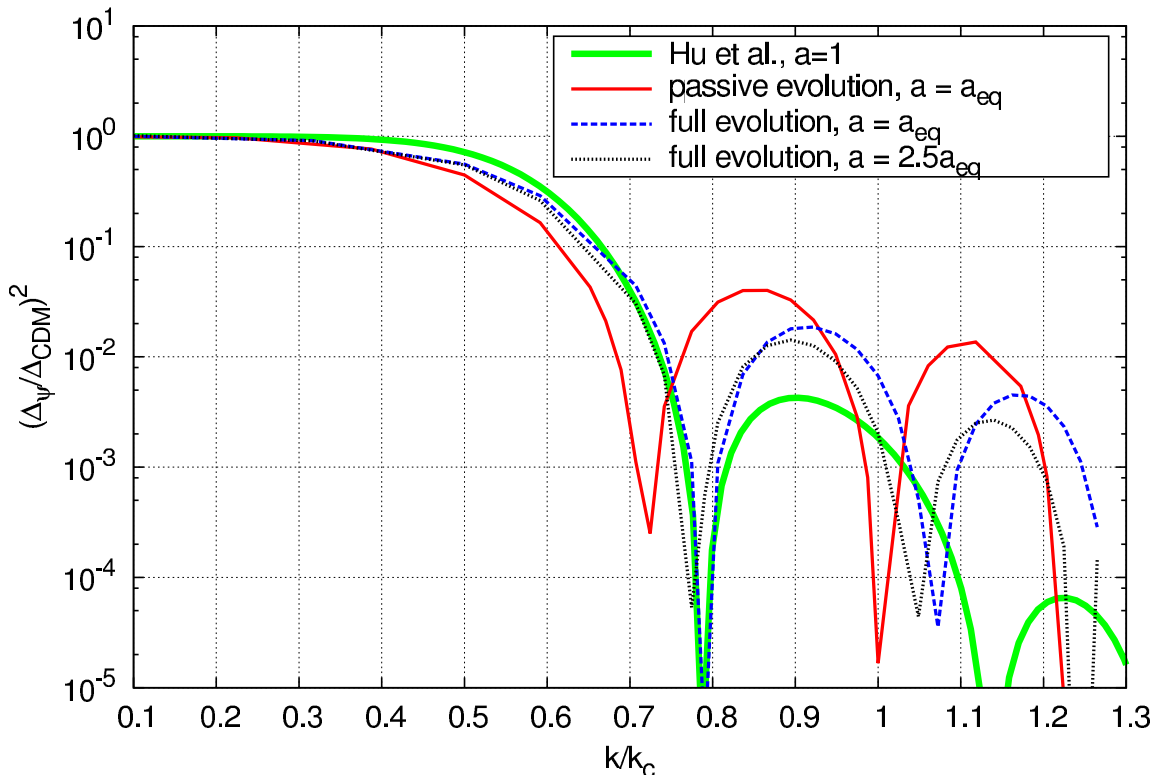


Figure 9.3: The  $\psi$ DM transfer function relative to CDM evaluated at  $a_{eq}$  and  $2.5a_{eq}$ . The horizontal axis is the wavenumber normalized to  $k_c$ . The solid line is for the passive evolution and the dashed line for the full treatment evaluated at  $a_{eq}$ . The dotted line is the full treatment evaluated at  $2.5a_{eq}$  where the plasma is still fully ionized. The particle mass is the same with Fig. (9.1). We see the passive evolution and the full treatment makes very little difference for  $k < 0.4k_c$ , and both follow the CDM power spectrum closely. But for  $k > 0.4k_c$ , the two begin to have noticeable differences, due primarily to slightly different frequencies in the matter-wave oscillation. The transfer function for the full treatment at  $a = a_{eq}$  also has little difference from that at  $a = 2.5a_{eq}$  for  $k < k_c$ . Above  $k_c$ , the wave function oscillates during this period. The bold line is the analytical fitting formula given by Hu et al. (2000) evaluated at the present, where further short-wave suppression well after  $a = a_{eq}$  is clearly seen.

wave numbers few times above  $k_c$  in comparison with the critical mode at the onset of mass oscillation. Thus, the sharp spectral transition has already been established when mass oscillation starts and real particles of finite mass  $m$  are crystalized.

Additional suppression also occurs in Phase (ib), which mostly affects modes near  $k_c$ . This suppression has nothing to do with the Compton length effect mentioned earlier, but something to do with the Jeans length. While the CDM mode still grows mildly as  $\ln(a/a_k)$ , the  $\psi$ DM mode in Phase (ib) oscillates with a constant amplitude, as  $\sin[A_k \ln(a \times a_k^{-1})]/A_k$ , leading to a  $k^{-2}$  suppression for shorter waves with  $A_k = k^2/2Hma$ . This Jeans suppression in the radiation-dominant regime is an extension of the more familiar counterpart in the matter-dominant regime.

Despite the formula given in the last paragraph for  $\psi$ DM modes was derived for  $k \ll k_c$ , it still roughly holds for  $k \sim k_c$ . Take the critical mode with particle mass  $m = 10^{-22}$  eV as an example. The mass oscillation begins around the photon temperature  $T_\gamma \sim 0.5$  keV, occurring 1/500 times smaller in  $a$  than that at the radiation-matter equality with  $T_\gamma \sim 1$  eV, and hence the oscillation amplitude of the critical mode is  $(\ln(a_{eq}/a_m))^{-1}$  smaller than that of the CDM mode of the same  $k$ . We thus have an oscillation amplitude suppression factor of about 6.2, pretty consistent with Fig.(9.3). In general, the oscillation amplitude suppression factor is approximately  $(\ln(500k/k_c))^{-1}(k_c/k)^2$  around  $k_c$ . This formula is still valid for a different particle mass  $m$ . For that purpose one simply replaces 500 by  $a_{eq}/a_m$ .

Accompanying the suppression of the high- $k$  power is the oscillation pattern for shorter waves in the power spectrum. There are two types of oscillations separately exhibited by modes of  $k \gg k_c$  and  $k \sim k_c$ . For longer waves, the oscillation pattern arises primarily from the matter-wave oscillation and for shorter waves from the photon fluid oscillation followed by the matter-wave oscillation. Although the oscillation pattern in the power spectrum for shorter waves is complicated, due to the mixture of two oscillations of different frequencies, the one for longer waves is predictable. The phase of the latter oscillation is given by  $(k/k_c)^2 \ln(a_{eq}/a_k)$  and hence the oscillation frequency in the power spectrum is  $[(k/k_c)^2(\ln(a_{eq}/a_m) + \ln(k_c/k))]^2$ . The transition between the two os-



cillation patterns for longer waves and for shorter waves is found roughly at  $k = 2.5k_c$  for  $m \sim 10^{-22}\text{eV}$ . (The power spectrum shown in Fig. (9.3) is hence not extended to cover such a short-wave regime.)

One can conveniently define  $k_{1/2}$  as the wavenumber for which the modal power is suppressed by 1/2 relative to CDM. Taking into account the phase and amplitude of the matter-wave oscillation, we find that  $k_{1/2}/k_c \sim (\alpha/\ln(m/m_{28}))^{1/2}$  for any  $m \gg m_{28}$  and  $\alpha \approx 1.3$  for passive evolution and  $\alpha \approx 1.7$  for active evolution, where  $m_{28} \equiv 10^{-28}\text{eV}$ . The mass dependence arises from that the onset of mass oscillations for a more massive particle occurs earlier ( $a_m \propto m^{-1/2}$ ), and therefore it has a more ample time to execute matter-wave oscillations before the radiation-matter equality.

Interestingly the Jeans wave number  $k_J$  in the matter dominated regime, for which modes with  $k < k_J$  grow like CDM and modes with  $k > k_J$  oscillate with constant amplitudes, is also  $\sqrt{2Hma}$ . Moreover in the matter-dominated regime,  $H \propto a^{-1/2}$  and hence the Jeans length  $k_J \propto a^{1/4}$ , mildly evolving toward shorter wavelengths. This explains why  $k_J$  is always larger than, but on the same order of,  $k_c$ . The oscillation pattern in the power spectrum near  $k_c$  is therefore frozen in the matter-dominant era and grows self-similarly as  $a^2$ .

It is relevant to also compute the phase  $S$  of  $\hat{\psi}$ , which, along with the power spectrum, can determine  $\psi$  used for simulations in the matter-dominant regime as the initial condition. The power spectrum  $\langle(\Re[\hat{\psi}])^2\rangle = \langle|\hat{\psi}|^2\rangle \cos^2(S)$  only provides a partial condition for this purpose. When  $\Re[\hat{\psi}]/|\hat{\psi}| = \cos(S)$  and  $\Im[\hat{\psi}]/|\hat{\psi}| = \sin(S)$  are available, one can construct  $\exp(iS)$  for each  $k$  mode. The amplitude  $|\hat{\psi}|$ , being a half-Gaussian random number, can be then fixed by constructing an exponential random number  $|\hat{\psi}|^2 \cos(S)^2$  and letting its average equal to the power spectrum. Figure (9.4) shows the ratio  $\Re[\hat{\psi}]/|\hat{\psi}|$  as functions of  $k$  at the matter-radiation equality ( $a = a_{eq}$ ) and at  $a = 2.5a_{eq}$  using the full treatment. The first thing brings to notice is  $\Im[\hat{\psi}] \gg \Re[\hat{\psi}]$  for long waves. This feature is apparent from the discussions of Phase (ib). Secondly,  $\Im[\hat{\psi}]$  grows substantially faster than  $\Re[\hat{\psi}]$  in between  $a = a_{eq}$  and  $a = 2.5a_{eq}$  due to the acceleration of self-gravity, and the ratio  $\Re[\hat{\psi}]/\Im[\hat{\psi}] \rightarrow 0$  from above for most  $k < k_c$  modes. These modes are purely

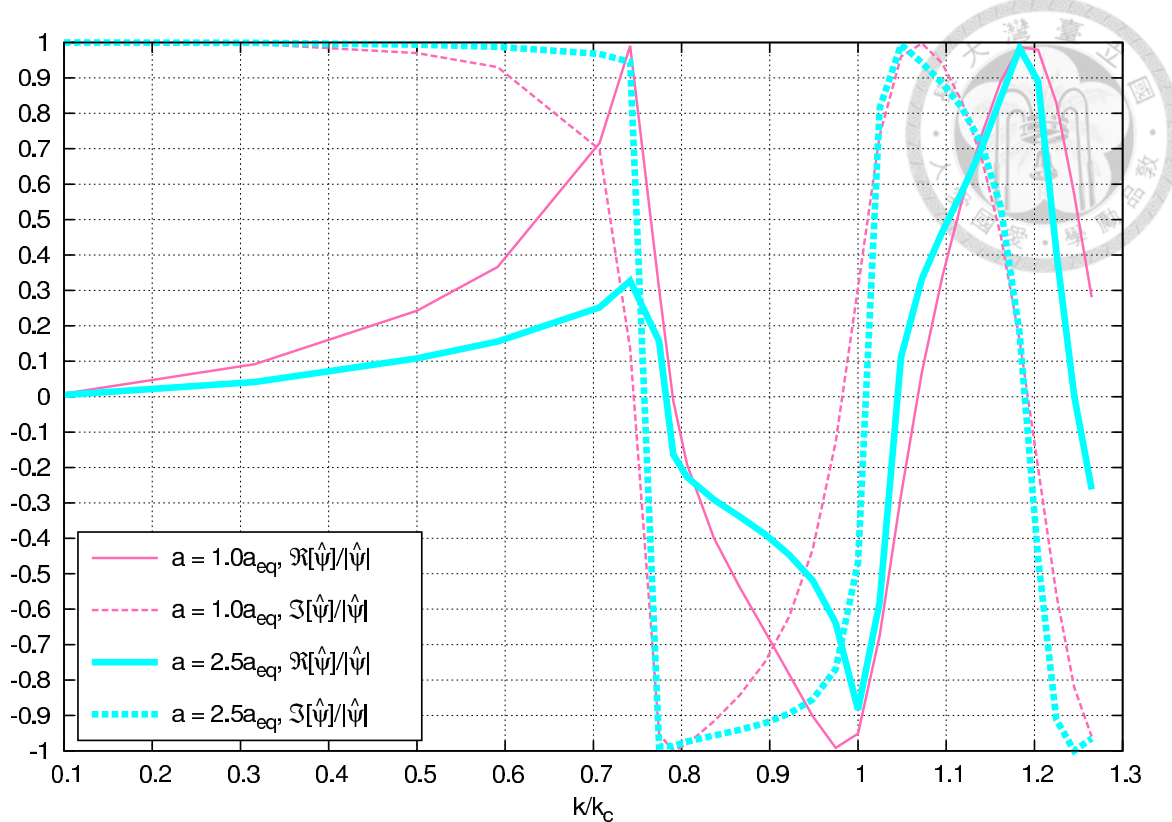


Figure 9.4: Phases of wave functions,  $\Re[\hat{\psi}]/|\hat{\psi}|$  and  $\Im[\hat{\psi}]/|\hat{\psi}|$ , evaluated at  $a = a_{eq}$  and  $a = 2.5a_{eq}$  as functions of  $k$ , and obtained by the full treatment. This plot also allows one to narrow down the value of Jeans length during this period as explained in the main text.

growing modes. For  $k > k_c$ , the wave function oscillates with a time-varying frequency, and in the range  $k_c < k < 1.3k_c$  plotted here, the oscillation frequency is nearly zero, indicative of that the wavenumber is close to the Jeans wavenumber  $k_J$ .

## 9.4 Adiabatic Perturbations for Superhorizon Modes

In the multi-fluid model, the condition for adiabatic perturbation is Eq. (9.4). Here  $\langle w \rangle$  is the short-time averaged equation of state parameter  $\langle w \rangle = \langle P/\epsilon \rangle$ .

Before the mass oscillation in Phase (iia), there is no fast mass oscillation and the equation of state for  $\psi$ DM is

$$1 + \langle w_\psi \rangle \sim 2 \left( \frac{ma}{5H} \right)^2 \rightarrow 0, \quad (9.17)$$

and in this phase  $\psi$ DM behaves similar to the dark energy. In Appendix B we see  $\delta_\gamma \sim$

$-2\phi$  in this phase, approximately a constant. Hence the adiabatic condition yields  $\delta_\psi = -(3/25)(m^2 a^2 / H^2)\phi$ , the same as we found by solving the approximate dynamical equation.

After mass oscillation in Phase (ia), we have used the adiabatic condition to pin down the value of the super-horizon energy perturbation, which involves an undetermined constant. In fact, one may question whether Eq. (9.4) in Phase (ia) really needs to take a short-time average. This question can be answered by examining Eq. (9.2) and the fact that  $1 + w_\psi \propto (\Psi')^2 \propto \sin^2(mt + \alpha)$ . Since  $\delta_\gamma/(1 + w_\gamma)$  has no mass oscillation but both  $\delta_\psi$  and  $w_\psi$  do, one should examine whether the respective oscillations of  $\delta_\psi$  and  $1 + w_\psi$  cancel. We had before  $\Re[\hat{\psi}] \sim -(3/4)\phi_0$ , and  $\Im[\hat{\psi}]_p = -(ma/2H)\phi_0$ . Upon substituting them into Eq. (9.2), we find  $\delta_\psi$  is also proportional to  $\sin^2(mt + \alpha)$ , and  $\delta_\psi/(1 + w_\psi)$  indeed has no oscillation. Therefore the adiabatic condition holds instantaneously without the need to take a short-time averages over  $\delta_\psi$  and  $w_\psi$ , even though the perturbation has fast oscillations.

Next, one may wonder why the long-wavelength adiabatic perturbations of  $\psi$ DM and CDM should track each other so well after the mass oscillation. A rough answer is that since they are both adiabatic and when the equations of state are the same, the two must be identical when super-horizon. As we have seen, the average equation of state parameter  $\langle w_\psi \rangle = 0$  in Phase (ia), the same as that of CDM, which justifies the above statement. Further considerations show that once the mode enters Phase (ib), we also have the same fluid description for  $\psi$ DM as that for CDM in the long wave limit, since  $\delta P_\psi = O((k/ma)^2 \delta \epsilon_\psi) \rightarrow 0$  when  $k \rightarrow 0$ . Therefore, for sufficiently long waves,  $\psi$ DM and CDM become almost identical after mass oscillation, despite the two are very different before mass oscillation.



# Chapter 10

## Axion Model

Axion has a field potential  $V = (fm)^2(1 - \cos(\Psi/f))$ , where there appears a new energy scale, the axion decay constant  $f$ , believed to be close to the GUT scale or the Planck scale (Chiueh, 2014; Hui et al., 2017b). In the limit  $\Psi/f \rightarrow 0$ , the axion potential is reduced to the free-particle harmonic potential discussed previously. Normally without fine tuning, it is expected that the initial axion angle  $\theta (\equiv \Psi/f)$  is of order unity at the very early epoch. (Here we have taken a simple axion model for which the field potential has been established long before the mass oscillation.)

Unlike the free particle model, the zero-order field obeys a nonlinear equation:

$$\theta'' + 2H\theta' + m^2a^2 \sin(\theta) = 0. \quad (10.1)$$

Similar to Eq. (8.1),  $\theta$  can oscillate, but initially executing anharmonic oscillation. Subject to the Hubble friction,  $\theta$  declines in amplitude after a couple of oscillations where  $\sin(\theta) \rightarrow \theta$ , and Eq. (10.1) becomes Eq. (8.1). Thus, the axion model is a straightforward extension of the free-particle model, and can address the initial phase-lock problem of  $\psi$ DM explained in Chapter 7.

The perturbed field now obeys

$$\delta\theta'' + 2H\delta\theta' + k^2\delta\theta + m^2a^2 \cos(\theta)\delta\theta = 4\theta'\phi' - 2m^2a^2 \sin(\theta)\phi, \quad (10.2)$$

which recovers Eq. (8.2) when  $\theta \ll 1$ . The only difference of the axion model from the free-particle models occurs near the  $ma = 2H$  transition, and the one additional free parameter for the axion model is the initial  $\theta$ , which we denote as  $\theta_0$ .

We need also define one more quantity, the dimensionless gauge-covariant energy density of the perturbed field

$$\Delta_\theta \equiv \frac{\theta' \delta\theta' + m^2 a^2 \sin(\theta) \delta\theta - (\theta')^2 \phi + 3H\theta' \delta\theta}{(1/2)(\theta')^2 + m^2 a^2 [1 - \cos(\theta)]}, \quad (10.3)$$

which is the normalized physical energy density perturbation and the denominator is the background field density  $\epsilon_\theta$ .

In contrast to the free-particle model, the axion model has no analytical solutions for the zero-order field, and hence the analytical solution to the first-order field is not attainable even for passive evolution. We replace Eqs. (8.1) and (8.2) by Eq. (10.1) and Eq. (10.2) and numerically integrate the coupled equations of the axion model as we did for the full treatment of the free-particle model. The results are plotted in Fig. (10.1) for  $\theta_0 = \pi/16, \pi/2, 179\pi/180$ , where the  $\theta_0 = \pi/16$  case is essentially the free-particle model.

Perturbations of the axion model also roughly have the four asymptotic solutions corresponding to the four asymptotic phases of the free-particle model. This is actually not surprising since the major difference between the two models is just during the time near the onset of mass oscillation; for a difference in such a short time, the asymptotic phases are little affected. Generally speaking, the initial anharmonic oscillation of the axion model has longer periods than the harmonic oscillation of the free-particle model and would lead to some phase delay of mass oscillation. But solutions at  $a \gg a_m$  turn out not to be sensitive to such a moderate phase shift. Only in the extreme case when  $\theta_0 \rightarrow \pi$  which we call the extreme axion model, where the onset of mass oscillation is significantly delayed causing the axion's first cycle of matter-wave oscillation discussed in Phase (ib) to take a substantially longer period than that of the free particle, can it make an appreciable difference. When comparing  $\theta_0 = 179\pi/180$  and  $\pi/2$  cases, the first feature common to all wave numbers is (1) a steep rise in amplitude at the onset of mass oscillation for

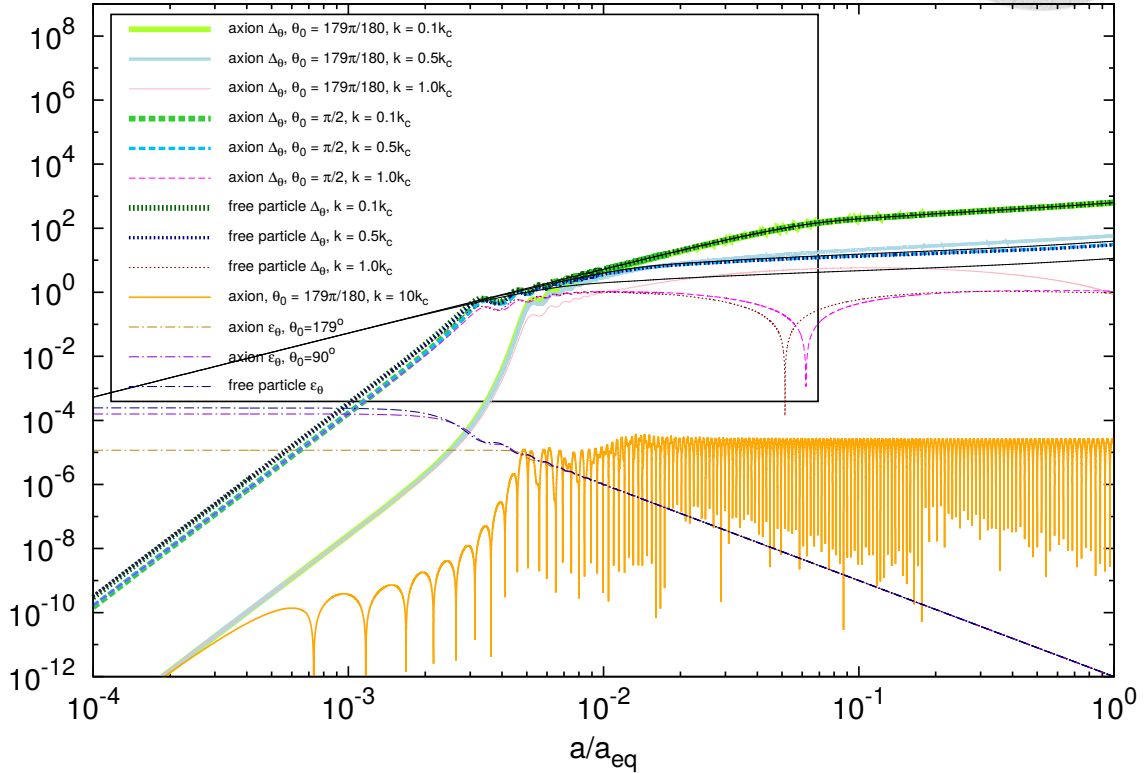


Figure 10.1: Full treatments of the axion model with three different initial angles  $\theta_0$ . The dotted line represents  $\theta_0 \ll 1$  (free-particle model), the dashed line  $\theta_0 = \pi/2$  and the solid line  $\theta_0 = 179\pi/180$ . We also plot three different wavenumbers,  $k \ll k_c$ ,  $k = 0.5k_c$  and  $k = k_c$ , for the above three  $\theta_0$ . For  $k \ll k_c$ , the initial angle  $\theta_0$  does not make any difference in covariant energy density perturbations  $\Delta_\theta$ . For  $k = 0.5k_c$ , some differences appear, particularly for the  $\theta_0 = 179\pi/180$  case, which has a higher amplitude. For  $k = k_c$ , the  $\theta_0 = 179\pi/180$  case becomes very different from the other two cases. For all three  $k$ 's, the  $\theta_0 \ll 1$  and  $\theta_0 = \pi/2$  cases have similar  $\Delta_\theta$ , indicative of that  $\Delta_\theta$  is insensitive to  $\theta_0$ , unless  $\theta_0$  assumes an extreme value very close to  $\pi$ . We also plot the short wavelength case ( $k = 10k_c$ ) for  $\theta_0 = 179\pi/180$  with the orange solid line and CDM model for  $k = k_c$ ,  $0.5k_c$  and  $0.1k_c$  with black solid lines to demonstrate three peculiar features of the extreme axion model. The background energy density  $\varepsilon_\theta$  which is normalized by  $(1/2)(\Omega_{DM}/(\Omega_{DM} + \Omega_b))\varepsilon_t^{eq} \times 10^{12}$  for the axion model with corresponding different initial angles  $\theta_0$  are also plotted with dot-dashed lines. Here  $\varepsilon_t^{eq}$  is the total energy density at the equality. The axion decay constant  $4\pi G f^2$  is  $4.64 \times 10^{-4}$  and  $1.71 \times 10^{-5}$  for  $\theta_0 = \pi/2$  and  $179\pi/180$ , respectively.

$\theta_0 = 179\pi/180$  not present for  $\theta_0 = \pi/2$ . A second feature of the  $\theta_0 = 179\pi/180$  case is (2) a substantially longer duration of the first half cycle of matter-wave oscillation for some  $k \sim k_c$  than that of the  $\theta_0 = \pi/2$  case for the same  $k$ . Associated with the second feature is a third feature that (3) the perturbation amplitude of the  $\theta_0 = 179\pi/180$  case is higher than that of the CDM model during a certain period also for some  $k \sim k_c$ , which has never been observed in the free-particle model. Clearly, these three features are not caused by ordinary nonlinear mass oscillation of  $\theta$ , but associated with the extreme condition where  $\theta_0 \rightarrow \pi$ . Note that the second and third features do not show up prominently for  $k \ll k_c$  and  $k \gg k_c$  in Fig. (10.1). This requires an explanation.

Figure (10.1) only shows full treatment results. However, the passive evolution indeed approximates the evolution of full treatment quite well till near the radiation-matter equality. The focus of our analysis in this work is placed upon after the onset of mass oscillation but still far away from the epoch of radiation-matter equality. Hence, passive evolution provides a fair simplification for understanding the above three features; however, our numerical solutions will include the full treatment. Also plotted in Fig. (10.1) are three background fields of different initial angles; their evolutionary tracks show that the three converge at the radiation-matter equality despite they start at three different initial amplitudes with different axion decay constants  $f$ .

We use the 4-th order Runge-Kutta scheme to solve the equations, where a sufficiently small time step is chosen so that one mass oscillation cycle takes about  $10^5$  time steps to resolve. We have checked the numerical convergence after  $\sim O(10^5)$  oscillation cycles at the radiation matter equality, and found the solution will not converge if we choose a time step one order of magnitude larger, especially for long waves.

## 10.1 Abrupt Growth of $\delta\theta$

Prior to the onset of mass oscillation, the perturbation grows as  $a^6$ , corresponding to the earliest phase (ii) in the evolution. When  $\theta_0$  is near the top of the field potential, it delays the mass oscillation, and substantial delay makes the friction  $2H\delta\theta'$  negligible in Eq. (10.2) at the onset of mass oscillation. This creates an almost frictionless background

for perturbed field dynamics. This rapid growth occurs only in a short time when  $\theta$  first rolls down from the potential top. The duration of exponential growth is independent of the exact location of the initial angle  $\theta_0$  from the potential top as long as  $\theta_0$  is close to the top. More importantly the abrupt growth is insensitive to wave number  $k$ , as evidenced from the same abrupt growth for  $k = 0.1k_c$  mode and  $k = 10k_c$  mode in the case of  $\theta_0 = 179\pi/180$  in Fig. (10.1). This provides a crucial clue for the growth mechanism.

The restoring forces of long-wave modes and short-wave modes are very different, with the former being negative and the latter being positive. Hence the same growth for all  $k$  modes indicates that the cause of the growth should be from the source, the right-hand side of Eq. (10.2). Unlike the free-particle model, well before the onset of nonlinear mass oscillation the source is almost zero, where  $\theta' \rightarrow 0$  and  $m^2 a^2 \sin(\theta) \rightarrow 0$  as  $\theta \rightarrow \pi$ . The weak constant source yields a small coefficient in the  $a^6$  growth (phase (ia)) before the abrupt growth, more so for  $\theta_0$  closer to the potential top, as opposed to a much larger coefficient due to a much larger source in the  $\theta_0 = \pi/2$  case. Just at the onset the source suddenly rises to its full strength when the field  $\theta$  rolls down the hill on its first pass. Such a drive is so abrupt that the perturbed field gets amplified regardless of the nature of its restoring force, since the restoring force has no time to respond. One may analogize this mechanism as the "direct current (DC)" drive, as opposed to the "alternative current (AC)" drive of the parametric instability to be discussed in the next section. After this short period of time, the source strength either stays in full strength or declines depending on whether the mode has entered horizon. For super-horizon modes, the source stays in full strength and the modes enter phase (ia) of a slow  $a^2$  growth, and for sub-horizon modes, they enter a new phase of parametric instability or matter-wave oscillation, phase (ib).

The exact location of  $\theta_0$  from the top would, however, affect the onset time of mass oscillation. For a given  $k$ , the more delay of the mass oscillation, the longer the duration of the  $a^6$  growth, and the perturbation can grow to a greater amplitude. On the other hand, the closer  $\theta_0$  is to the field potential top, the smaller is the source, and the smaller the coefficient of the  $a^6$  growth as mentioned above. These two opposite trends almost cancel, and by the end of the abrupt growth,  $\delta\theta$  is brought to nearly the same amplitude as the free-

particle model. An alternative way to understand this is that once the source becomes at its full strength, it drives the perturbed field to a level comparable to the photon perturbation before the perturbed field becomes decoupling from the source shortly after the onset of mass oscillation. Such a driving mechanism applies to all adiabatic perturbations.

## 10.2 Parametric Instability

Parametric instability refers to the presence of an oscillating restoring force of almost twice the natural frequency for an oscillator, described by Mathieu's equation (Abramowitz and Stegun, 1964):

$$\ddot{Q} + \omega_\theta^2 [1 + \eta + \epsilon \cos(2\omega_\theta t)] Q = 0, \quad (10.4)$$

where  $Q$  is the oscillator solution and the overdot denotes  $d/dt$ . The parameters  $\epsilon$  and  $\eta$  are the driver strength and the detuning squared frequency. The  $(\eta, \epsilon)$  phase diagram at small  $\epsilon$  and  $\eta$  marks the marginally stability curve as  $|\eta| = (1/2)|\epsilon|$ . In the limit  $\eta = 0$ , the oscillator is unconditionally unstable even for a tiny but finite  $\epsilon$ .

To make a comparison with Mathieu's equation, we change the variable of Eq. (10.2) from the scaling factor  $a$  to the ordinary time  $t$ . A straightforward algebra shows that Eq. (10.2), Taylor-expanded up to the first-order nonlinearity in  $\theta$ , can be cast into the equation:

$$\ddot{q} + \left\{ \frac{3}{4} \mathcal{H}^2 + \frac{k^2}{a^2} + m^2 \left[ 1 - \frac{\langle \theta^2 \rangle}{4} \left( 1 + \cos \left( 2 \int_{t_m}^t \omega_\theta dt \right) \right) \right] \right\} q = \frac{Sr}{a^{\frac{1}{2}}}, \quad (10.5)$$

where  $q \equiv \delta\theta / \sqrt{\epsilon_\theta}$  with  $\epsilon_\theta$  being the background energy density,  $\mathcal{H} = H/a$ ,  $t_m$  is the time for the onset of mass oscillation,  $\omega_\theta$  the frequency of  $\theta$  containing a nonlinear frequency shift, and  $Sr$  is the right-hand side of Eq. (10.2). The short-time average  $\langle \theta^2 \rangle$  decays as  $a^{-3}$ , which we model as  $\langle \theta^2 \rangle = (\theta_0^2/2)(t/t_m)^{-3/2}$ .

The frequency  $\omega_\theta$  of the nonlinear oscillation of  $\theta$  can be derived from Eq. (10.1), where the restoring force  $\sin(\theta) = \theta(1 - \theta^2/6) + O(\theta^5) \sim \theta_0(t/t_m)^{-3/4}[1 - (t/t_m)^{-3/2} \times (\theta_0^2/8)] \cos(\int \omega_\theta dt) - [\theta_0^3(t/t_m)^{-9/4}/24] \cos(3 \int \omega_\theta dt)$ , assuming  $\theta = \theta_0(t/t_m)^{-3/4} \times \cos(\int \omega_\theta dt)$ . Ignoring the triple frequency term and retaining the coefficient of  $\cos(\int \omega_\theta dt)$ ,



we have the driving frequency

$$\omega_\theta^2 = m^2 \left[ 1 - \frac{\theta_0^2}{8} \left( \frac{t}{t_m} \right)^{-\frac{3}{2}} \right]. \quad (10.6)$$

On the other hand, the perturbed field  $q$  has a natural frequency  $\omega_\delta$  different from the driving frequency  $\omega_\theta$  and related by

$$\omega_\delta^2 = \omega_\theta^2 \left[ 1 - \frac{\theta_0^2}{8} \left( \frac{t}{t_m} \right)^{-\frac{3}{2}} \right], \quad (10.7)$$

to the leading order.

We shall address the sub-horizon regime where  $k/a \gg \mathcal{H}$ . Hence we can ignore both the weak source term  $Sr$  as the driver  $\phi$  declines as  $a^{-2}$  and the  $\mathcal{H}^2$  term in Eq. (10.5), thus arriving at a simplified equation that describes the homogeneous solution of  $q$ ,

$$\ddot{q} + \left\{ \frac{k^2}{a^2} + \omega_\theta^2 \left[ 1 - \frac{\theta_0^2}{8} \left( \frac{t}{t_m} \right)^{-\frac{3}{2}} \left( 1 + 2\beta \cos \left( 2 \int_{t_m}^t \omega_\theta dt \right) \right) \right] \right\} q = 0, \quad (10.8)$$

with  $\beta = 1$ . An additional parameter  $\beta$  is introduced so as to make a close contact with the Mathieu's equation which has two parameters  $\epsilon$  and  $\eta$ . Due to the delayed mass oscillation negligence of the small  $\mathcal{H}^2$  term is critical to set the extreme axions apart from axions with initial fields at other locations of the field potential, since when  $\mathcal{H}^2$  is non-negligible this term will suppress the parametric instability. We shall avoid such a complexity by focusing on the extreme axion case in the wavenumber range  $k \leq O(k_c)$ . In this situation, the  $\mathcal{H}^2$  term can always be ignored. See Appendix E for a discussion of the general case.

Now, Eq. (10.8) is the Mathieu's equation with time-dependent coefficients, where the detuning squared frequency  $\eta = (k^2/a^2) - \delta\omega^2$  and the driver strength  $\epsilon = 2\delta\omega^2$  with  $\delta\omega^2 \equiv \omega_\theta^2(\theta_0^2/8)(t/t_m)^{-3/2}$ . Note that when  $(k/a)^2 \rightarrow 0$ , we have  $|\eta| = (1/2)|\epsilon|$  and it satisfies the marginally stable condition of Mathieu's equation. Worth noting is that the squared detuning frequency  $\eta$  has zero-crossing for a range of  $k$  and  $a$ , and these  $k$ -modes can temporarily be parametrically unstable. This provides a crude explanation as to why in some range of  $k$  the matter-wave oscillation appears to be amplified and has a relatively high amplitude, i.e., feature (3), but more details will follow.

Other than the aforementioned growth due to the parametric drive, the frequency of the solution of Eq. (10.8) actually deviates from its natural frequency and is locked to near half of the driving frequency for some period; therefore the solution becomes nearly phase locked to the driver during this period. We may let  $q = \Re[\hat{q} \exp(-i \int \omega_\theta dt)] = \Re[\hat{q}] \cos(\int \omega_\theta dt) + \Im[\hat{q}] \sin(\int \omega_\theta dt)$  while the background field  $\theta = \sqrt{\epsilon_\theta} \cos(\int \omega_\theta dt)$ , where  $\hat{q}$  is a slowly varying complex amplitude. When  $q$  and  $\theta$  are phase locked, the amplitudes of  $\Re[\hat{q}]$  and  $\Im[\hat{q}]$  will remain fixed and do not oscillate until the nonlinearity dies out, after which the perturbation assumes free-particle matter-wave oscillation. This picture provides a rough baseline as to why the first half cycle of matter-wave oscillation in  $\Delta_\theta$  has a long duration. Again, more details are to come.

We shall analyze an even more simplified version of Eq. (10.8) below, which bears more resemblance to Mathieu's equation, in order to bring out the aforementioned frequency locking and the amplitude excess in a quantitative manner. We assume the background field oscillates at a fixed frequency,  $\omega_\theta = m$ , ignoring the nonlinear contribution to the driving frequency which is a high-order effect for our purpose. Equation (10.8) thus becomes

$$\ddot{q} + \left\{ \frac{k^2}{a^2} + \omega_\theta^2 \left[ 1 - \frac{\theta_0^2}{8} \left( \frac{t}{t_m} \right)^{-\frac{3}{2}} \left( 1 + 2\beta \cos(2\omega_\theta(t - t_m)) \right) \right] \right\} q = 0, \quad (10.9)$$

Using this  $\hat{q}$  representation for sub-horizon modes after mass oscillation, one can show that the normalized energy density  $\Delta_\theta \approx 2\Re[\hat{q}]$ . Aside from the coefficient, the interaction ( $\beta$ ) term in Eq. (10.9) yields  $(\Re[\hat{q}]/2)[\cos(\omega_\theta(t - t_m)) + \cos(3\omega_\theta(t - t_m))] - (\Im[\hat{q}]/2)[\sin(\omega_\theta(t - t_m)) - \sin(3\omega_\theta(t - t_m))]$ . Again ignoring the triple frequency contribution, the interaction term is then proportional to  $(1/2)[\Re[\hat{q}] \cos(\omega_\theta(t - t_m)) - \Im[\hat{q}] \sin(\omega_\theta(t - t_m))] = (1/2)\Re[\hat{q}^* \exp(-i\omega_\theta(t - t_m))]$ . Substituting this result into Eq. (10.9), we have a reduced perturbation equation satisfying

$$i\dot{\hat{q}} = \frac{1}{2\omega_\theta} \left[ \left( \left( \frac{k}{a} \right)^2 - \alpha \right) \hat{q} - \beta \alpha \hat{q}^* \right], \quad (10.10)$$

where  $\alpha = \omega_\theta^2(\theta_0^2/8)(a_m/a)^3$ , and  $a_m$  is the scaling factor at the onset of nonlinear mass

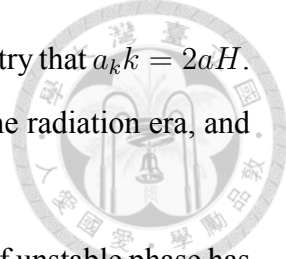
oscillation. Separating the real and imaginary parts of  $\hat{q}$ , one can straightforwardly show that the dispersion relation for this equation is  $\omega = (1/2\omega_\theta)[[(k/a)^2 - \alpha]^2 - (\beta\alpha)^2]^{1/2}$  with  $\omega$  being the matter-wave frequency. This dispersion relation yields the characteristics of parametric instability. For the  $\beta = 1$  axion case, the dispersion relation becomes

$$\omega = \frac{k}{2\omega_\theta a} \left[ \left( \frac{k}{a} \right)^2 - 2\alpha \right]^{1/2}, \quad (10.11)$$

and the mode is unstable when  $k^2/2a^2\alpha < 1$ , and stable with  $\omega \rightarrow k^2/2\omega_\theta a^2$  when  $k^2/2a^2\alpha \gg 1$ . This dispersion relation is valid even when  $\omega_\theta \neq m$  where Eq. (10.6) holds. For simplicity we shall continue to ignore the nonlinear correction to the driving frequency and assume  $\omega_\theta = m$ .

We first note the factor  $k^2/(2a^2\alpha) \propto k^2(a/a_m)(a_m)^{-2}$ , the greater  $a_m$  of nonlinear mass oscillation is, or the closer  $\theta_0$  is to  $\pi$ , the smaller the magnitude of this factor at a given  $a/a_m$ , thus mimicking a smaller  $k$  for the free-particle model that has a longer matter-wave oscillation period and accounts for feature (2). On the other hand, for a given  $\theta_0$  near  $\pi$  and in the limit  $k \rightarrow 0$ , the parametric instability is weak, as by the time when the mode enters horizon where Eq. (10.11) becomes valid, the nonlinearity is already small. So the only range of  $k$  exhibiting a strong parametric growth is when  $k$  is on the same order of  $k_c$ . This explains why the amplitude excess occurs for  $k$  on the same order of  $k_c$ , feature (3).

To put the above into quantitative perspectives, one readily sees from the dispersion relation, Eq. (10.11), that the frequency's being either imaginary and small compared with the free-particle frequency is to contribute to higher perturbation amplitudes and a longer duration in the first half cycle of matter-wave oscillation. The unstable phase takes place during a time interval  $\ln(a_0/a_{m0}) = 2\ln(\theta_0/2) + 3\ln(a_m/a_{m0}) + 2\ln(k_c/k)$  or  $\ln(a_0/a_k) = 2\ln(\theta_0/2) + 3\ln(a_m/a_{m0}) + \ln(k_c/k)$  depending on whether the mode has entered horizon or not, respectively, at the onset of nonlinear mass oscillation, where  $a_0$  is the scaling factor at the end of growth  $\omega = 0$ , and  $a_k$  that at the horizon entry  $k = 2H$ . Here  $a_{m0}$  corresponds to  $a$  at the onset of free-particle mass oscillation, i.e.,  $2H(a_{m0}) = ma_{m0}$ , and the critical wave number for the free particle model,  $k_c = (2maH)^{1/2} = ma_{m0}$ ; by the



same token, we have  $a_k/a_{m0} = k_c/k$  using the definition of horizon entry that  $a_k k = 2aH$ . (The quantity  $aH = a_{m0}H(a_{m0})$  since it is redshift-independent in the radiation era, and we thus have  $k_c \propto m^{1/2} \propto a_{m0}^{-1}$ .)

As a supplementary remark, the above estimate for the duration of unstable phase has taken into account that prior to this parametric growth, low- $k$  super-horizon mode must go through the  $a^2$  growth of phase (ia) even after the onset of nonlinear mass oscillation, where the driving source  $Sr$  is still strong and Eq. (10.8) is not valid; for such modes, only after horizon entry,  $a = a_k$ , does Eq. (10.8) become valid and hence the solution of this equation starts at  $a_k$ .

For these sub-horizon  $k$  modes subject to parametric instabilities, the amplitudes increase by a growth factor proportional to  $\exp[A(a_\kappa) - A(a)]$ , and the exponent of the growth factor at the end of parametric growth can be shown to be

$$A(a_\kappa) = \frac{2k^2}{k_c^2} \left\{ \left[ \frac{a_{m0}}{a_\kappa} \left( \frac{a_m}{a_{m0}} \right)^3 \frac{k_c^2 \pi^2}{k^2 \frac{4}{4}} - 1 \right]^{\frac{1}{2}} - \tan^{-1} \left[ \left( \frac{a_{m0}}{a_\kappa} \left( \frac{a_m}{a_{m0}} \right)^3 \frac{k_c^2 \pi^2}{k^2 \frac{4}{4}} - 1 \right)^{\frac{1}{2}} \right] \right\}, \quad (10.12)$$

using WKB approximation, where  $a_\kappa = a_k$  and  $a_\kappa = a_m$  correspond to  $a_k > a_m$  and  $a_k < a_m$ , respectively,  $A(a_0)$  is defined to be 0, and  $\theta_0$  takes the value  $\pi$ . (See Appendix D for derivation.) This growth factor is responsible for the power excess. When  $(a_m/a_\kappa)[(a_m/a_{m0})(k_c/k)(\pi/2)]^2 \gg 1$ , the growth factor  $\exp[A(a_\kappa)]$  becomes  $\exp[\pi(k \times k_c^{-1})(a_m/a_{m0})^{3/2}(a_{m0}/a_\kappa)^{1/2}]$ . Therefore for long waves we have small amplification,  $A(a_k) \propto (k/k_c)^{3/2}$  as  $a_{m0}/a_k = k/k_c$ . On the opposite limit for short waves,  $k > k_c(a_m/a_{m0})(\pi/2)$ , the parametric growth would never occur. This explains why we do not see the power excess for long waves and short waves in Fig. (10.1).

This unstable phase is followed by a matter-wave oscillation phase but with a lower frequency than normal. The solution in this phase has a form  $\sin(B(\eta) + \pi/4)$ , where the detail is also given in Appendix D using WKB approximation, and we have

$$B(\eta) = 2 \frac{k^2}{k_c^2} \left\{ -[1 - r \exp(-\eta)]^{1/2} + \frac{1}{2} \ln \left[ \frac{1 + [1 - r \exp(-\eta)]^{\frac{1}{2}}}{1 - [1 - r \exp(-\eta)]^{\frac{1}{2}}} \right] \right\}. \quad (10.13)$$

Here  $\eta \equiv \ln(a/a_m)$  and  $r = (k_c/k)^2(\pi^2/4)(a_m/a_{m0})^2$ . This oscillation has an initial

$B(\eta) = 0$  at  $\eta = \eta_0$  where  $\omega = 0$ , but otherwise  $B(\eta) \geq 0$  for  $\eta \geq \eta_0$ .

The peak of the power excess (feature 3) should be located in this oscillation phase since the solution  $\sin(B(\eta) + \pi/4)$  is still on the rise at  $\eta_0$ . If one is to assume that solutions have resumed free-particle matter-wave oscillations when they reach the peaks, i.e.,  $r \exp[-\eta] \ll 1$ , then one may find the timing  $\eta_{peak} (\equiv \ln(a_{peak}/a_{m0}))$  of the solution peaks as a function of  $k$ ,  $m$  and nonlinearity given by  $\sin[B(\eta_{peak}) + \pi/4] = 1$ , or  $B(\eta_{peak}) + \pi/4 = \pi/2$ . We thus have

$$\eta_{peak} = \frac{\pi}{4} \left( \frac{k_c}{k} \right)^2 + 2(1 - \ln(2)) + \left[ 2 \ln \left( \frac{k_c}{k} \right) + 3 \ln \left( \frac{a_m}{a_{m0}} \right) + 2 \ln \left( \frac{\pi}{2} \right) \right], \quad (10.14)$$

where terms in the squared bracket are contributed from the growing phase.

Subtracting  $\eta_{peak0}$  of the free-particle model from this  $\eta_{peak}$ , we can determine the total delay in the first quarter cycle of nonlinear mass oscillation. As shown in Appendix B, the free-particle model has a oscillating solution  $\propto \sin[(k/k_c)^2[\eta - \ln((\sqrt{3}/2)(a_\kappa/a_{m0}) + c_0(k))]]$  in phase (ib). Here, the phase  $c_0(k) = \cos^{-1}[1/((1 + (k/k_c)(\gamma - 0.5))^2)^{1/2}]$  with  $\gamma$  being the Euler number  $\sim 0.577$ , and thus  $c_0(k)$  is nearly 0 for a wide range of  $k/k_c$ . Now, using  $(k/k_c)^2(\eta_{peak0} - \ln((\sqrt{3}/2)(a_\kappa/a_{m0})) = \pi/2$  to fix  $\eta_{peak0}$ , we obtain the total delay  $\Delta\eta (= \eta_{peak} - \eta_{peak0})$  as

$$\Delta\eta_{peak} \approx -\frac{\pi}{4} \left( \frac{k_c}{k} \right)^2 + (1 + \kappa) \ln \left( \frac{k_c}{k} \right) + 3 \ln \left( \frac{a_m}{a_{m0}} \right) + 2 + 2 \ln \left( \frac{\pi}{4} \right) + \ln \left( \frac{2}{\sqrt{3}} \right), \quad (10.15)$$

where  $a_\kappa/a_{m0} = k_c/k$  has been used, and  $\kappa = 0$  for long waves where  $a_\kappa = a_k$  and  $\kappa = 1$  for short waves where  $a_\kappa = a_{m0}$ .

This is an interesting prediction, in that the strong negative  $(k_c/k)^2$  dependence of  $\Delta\eta_{peak}$  can make the delay be negative. The cause of the reverse effect is that the growing phase of parametric instability brings the amplitude to  $1/\sqrt{2}$  of the peak in a time weakly dependent on  $k_c/k$ . This period can be short compared to the free matter-wave oscillation to bring the amplitude to a similar level for long waves, which take a time  $\delta\eta \sim (4/\pi)(k_c/k)^2$ . The maximum  $\Delta\eta_{peak}$  can be found by taking a derivative of it with respect to  $k_c/k$  and the maximum delay is found to be near  $k/k_c \sim 1$ . This explains why

the delay in the first half cycle of nonlinear mass oscillation is prominent only around  $k \sim k_c$  in Fig. (10.1).

Finally, since our results above depend on  $a_m$ , it is useful to pin down the relation between  $\delta\theta_0 (\equiv \pi - \theta_0)$  and  $a_m$ . One can Taylor expand the field potential gradient near  $\theta_0 = \pi$  in Eq. (10.1) where  $\sin(\theta) \approx \theta - \pi = \delta\theta$ . Since the results, Eqs. (10.12), (10.14) and (10.15), are derived using Mathieu's equation, Eq. (10.9), to be consistent with these results, one should define  $a_m$  in accordance with the power-law-amplitude assumption. We extrapolate the asymptotic power-law solution,  $\langle \theta^2 \rangle \propto t^{-3/2}$ , backward in time till it intercepts the actual background solution at  $\pi^2$  to define the onset time  $t_m$ . In so doing, we find the following analytical formula provides the best fit:

$$\left( \frac{a_m}{a_{m0}} \right)^2 \approx 3.5 - \frac{2}{3} \ln \left( \frac{\delta\theta_0}{\delta\theta_{01}} \right), \quad (10.16)$$

where  $\delta\theta_{01} = 1^\circ$ . This expression works fairly fine; using it to compute  $\eta_{peak}$  of Eq. (10.14) gives  $< 10\%$  errors against the measured  $\eta_{peak}$ .

## 10.3 Numerical Solution and General Nonlinear Model

In Fig. (10.2), we plot  $\Delta_\theta$ 's constructed from the numerical solutions of Eq. (10.2) for passive evolution. The fiducial particle mass  $m = 10^{-22}$  eV is chosen. A comparison to  $\Delta_\theta$ 's constructed from Eq. (10.8) is also shown here, where we take  $\beta = 1$  and the metric fluctuation  $\phi = 0$ ; the initial solution slope is set to  $\dot{q}/q = [\omega_\theta^2(3\pi^2/8 - 1) - k^2/a_m^2]^{1/2}$  (c.f., Eq. (10.8)). Clearly seen in Fig. (10.2) is good agreement between the two solutions, except in the early time where our leading-order Taylor expansion of the nonlinearity fails. This plot demonstrates that peculiar features (2) and (3) appearing in the solution of Eq. (10.2) indeed arise from the parametric drive. These two features show strongly for  $k \sim k_c$  modes than for  $k \ll k_c$  modes as explained in the last section. In Fig. (10.2), we also plot a third solution of a fluid equation derived in Appendix D, we present the fluid equation, Eq. (D.1). This fluid equation filters out the high-frequency mass oscillation and is therefore an equation for the slowly varying amplitude. One can see that this third solution agrees

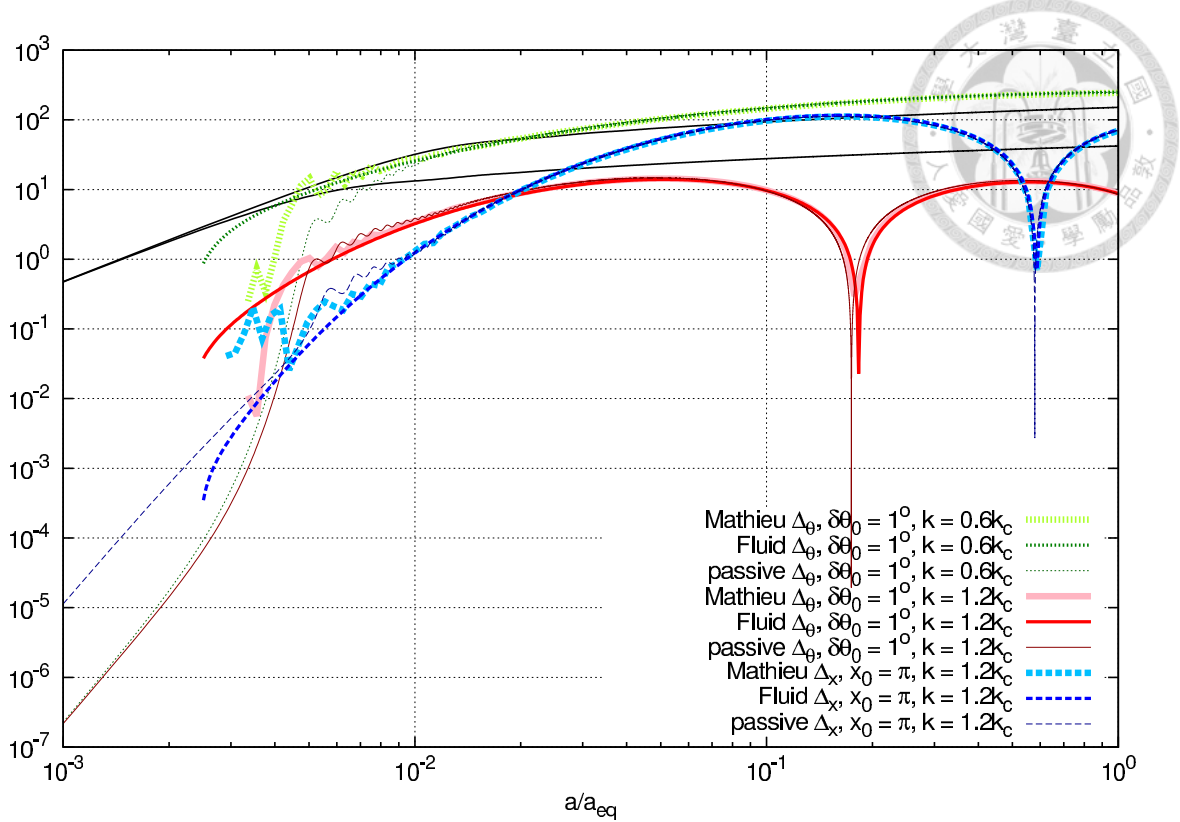


Figure 10.2: Comparison of  $\Delta_\theta$ 's constructed from passive evolution, Mathieu's equation, Eq. (10.8) and the fluid equation, Eq. (D.1). The solutions given by Mathieu's equation and fluid equation agree very well with those of passive evolution long after the onset of nonlinear mass oscillation. Plotted here are also solutions of passive evolution for another nonlinear scalar field model with a potential  $\propto 1 - \text{sech}(x)$  and of the corresponding Mathieu's equation and fluid equation for comparison, and excellent agreement is also found. Black lines are passive CDM perturbations for  $k = 0.6$  and  $1.2k_c$ . Particle mass  $m = 10^{-22}$  eV is assumed.

with the solution of Mathieu's equation, Eq. (10.8), extremely well.

To further demonstrate the general validity of Eq. (10.8) approximating the original perturbed field equation, we consider the potential  $(m^2 a^2)[1 - \text{sech}(x)]$ , where  $x$  is the field. We replace mass terms in the field equations, Eqs. (10.1) and (10.2), by  $(m^2 a^2) \tanh(x) \text{ sech}(x)$  and  $(m^2 a^2) \text{ sech}(x)[-1 + 2 \tanh^2(x)]\delta x$ , respectively, which yield  $\beta = 1$ ,  $\alpha = (5x_0^2/8)(t/t_m)^{-3/2}$  and  $\omega_x^2 = m^2 - \alpha$ . Here we also choose the initial field value  $x_0 = \pi$ . Plotted also in Fig. (10.2) is the comparison of  $\Delta_x$ 's constructed from the passive evolution and Eq. (10.8). Again, excellent agreement is found when  $t \gg t_m$ , reinforcing our claim for the parametric drive of the original perturbed field equation.

To end this section, we notice that  $\beta = 1$  is quite generic to all symmetric field potentials, and this can be shown as follows. Let the Taylor expansion of the field po-

tential be  $V(x) = (m^2 a^2/2)(x^2 - (b/2)x^4 + O(x^6))$ , and the potential gradient  $V' = (ma)^2(1 - bx^2)x \sim m^2(1 - (3b/4)x_0^2)x \equiv \omega_x^2 x$ , where  $x_0$  is the oscillation amplitude, and  $\omega_x$  is the nonlinear driving frequency adopting the technique used for the axion case. The coefficient of the restoring force in the perturbation equation is  $V'' = (ma)^2(1 - 3bx^2)$ , which can be reduced to  $\omega_x^2[1 - (3b/4)x_0^2(1 + 2\cos(2\omega_x t))]$ . In Section 10.2, we have parametrized the last factor as  $(1 + 2\beta \cos(2\omega_x t))$ , and hence  $\beta = 1$  for all nonlinear models with symmetric potentials with a finite mass.

The transfer function will be provided to end this chapter. The matter spectra not long after the radiation-matter equality is particularly interesting since by then the primary spectral feature can hardly evolve and is frozen throughout the later evolution. We plot in Fig. (10.3) the transfer function,  $|\Delta_\theta/\Delta_{cdm}|^2$ , of several initial field angles  $\Delta\theta_0$ 's at  $a = a_{eq}$ ,  $2.5a_{eq}$  and  $5a_{eq}$  using the full treatment, where  $a_{eq}$  is the scaling factor at the radiation-matter equality. One can clearly see the broad spectral bumps in all extreme initial angles. For  $k$  at and smaller than the spectral peak the transfer function barely evolves after  $a_{eq}$ , but are opposite for larger  $k$ . This is due to the Jeans wave number around  $a_{eq}$  is close to  $k_c$ ; above the Jeans wavelength, perturbations grow self-similarly as those of CDM but below, perturbations become neutrally stable oscillating matter waves (Hu et al., 2000; Woo and Chiueh, 2009).

In evolving toward  $a = 5a_{eq}$ , the photon-electron decoupling occurs around  $a = 3a_{eq}$  and the photon perturbation contributes very little to the metric perturbation since then. In Appendix C, we showed that the drag between baryons and photons already damps out the photon perturbation prior to photon-electron decoupling for  $k > k_c$ , and hence the metric perturbation indeed has no contribution from photons regardless of whether or not we have considered the electron-baryon recombination physics. But for  $k \ll k_c$ , the drag is ineffective and hence metric perturbations are affected by photons at  $a > 3a_{eq}$  if the silk damping is not properly accounted for, and can produce some errors in the matter power spectrum. Our full treatment does not take in to account the silk damping. However, this error for matter perturbations is practically small since matters are cold and photons are hot, and gravity responds to cold matter. Moreover, these small errors in both CDM

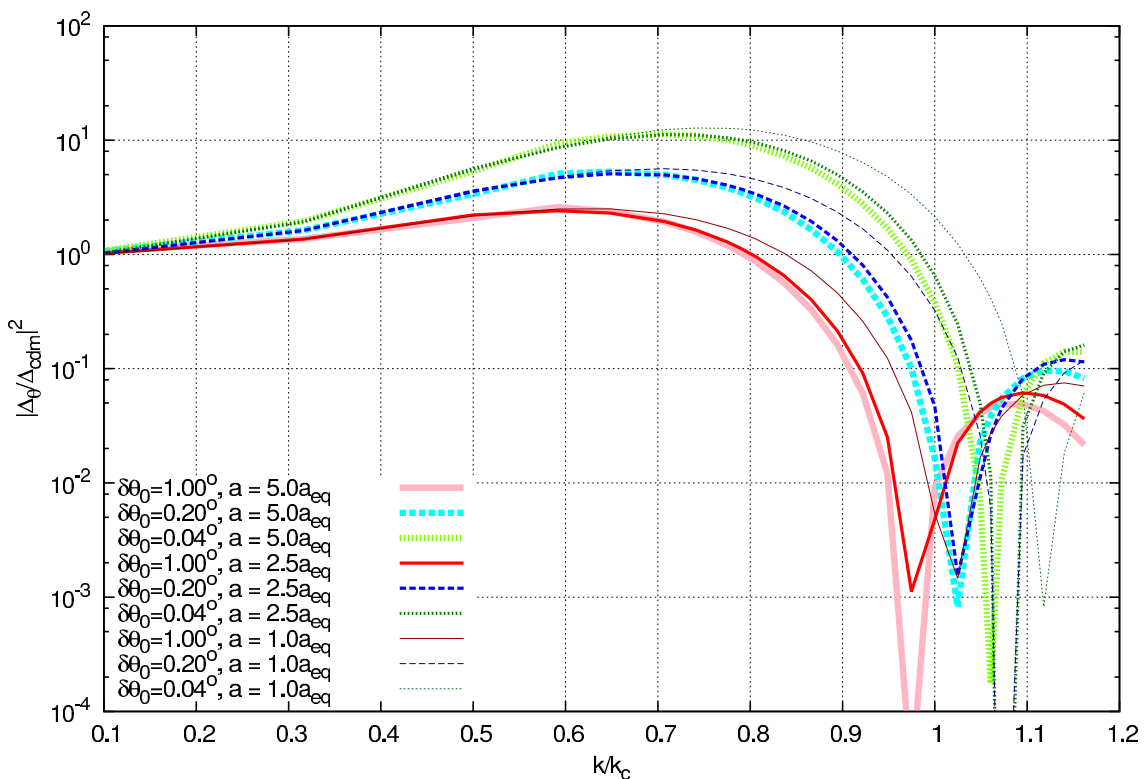


Figure 10.3: Transfer functions of the extreme axion model of  $m = 10^{-22}$  eV with different initial angles at  $a_{\text{eq}}$ ,  $2.5a_{\text{eq}}$  and  $5a_{\text{eq}}$ . Note that the quantity  $k_{\text{peak}}$  is almost frozen ever since  $a = a_{\text{eq}}$ . The three initial angles correspond to the axion field strengths,  $4\pi G f^2 = 1.71, 1.13, 0.821 \times 10^{-5}$  from large to small  $\delta\theta_0$ .

and axion perturbations are the same in our full treatment since at long waves the two perturbations are almost identical. Hence the transfer function is insensitive to such errors present in their respective spectra. It is based on this rationale the transfer functions at  $a = 5a_{eq}$  are presented in Fig. (10.3).

In Fig. (10.3), we have made sure that the dark matter energy density  $m^2 f^2 \theta^2$ , together with baryon energy density, equals the radiation energy density at  $a_{eq}$ . As  $\theta_0$  approaches  $\pi$  that delays the onset of nonlinear mass oscillation, the value of  $f$  must decrease to satisfy the above condition. Normally the field strength is characterized by a dimensionless parameter  $f^2/m_p^2 (\equiv 4\pi G f^2)$ , where  $m_p$  is the Planck mass. The free-particle case corresponds to  $f^2/m_p^2 \rightarrow \infty$ . The appropriate parameter regime for the extreme axion model has values  $f^2/m^2 \sim O(10^{-5})$ , and so  $f$  is on the order of GUT scale.



# Chapter 11

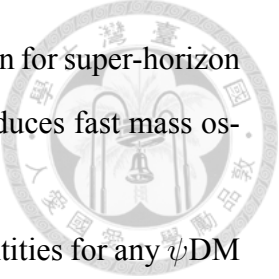
## Conclusions for Part II

Why the matter power spectrum at the end of radiation era exhibits a CDM-like spectrum for long waves and a highly suppressed spectrum for short waves and why the transition of these two types of spectra is sharp are fully explored. Physically the sharp power suppression is due to the smearing of fluctuations below the Compton length. Dynamically it is due to short waves prematurely entering horizon before mass oscillations, so that quantum pressure becomes so effective as to slow down the otherwise very rapid growth which long waves entertain.

To summarize, the following issues are addressed and results obtained:

(1) We elucidate four asymptotic phases with passive evolution—before mass oscillations, after mass oscillations, super-horizon wavelengths and sub-horizon wavelengths. The transition occurs at the intersection of the four asymptotic phases, i.e., at the onset of mass oscillations for the wavelength just beginning to enter the horizon, i.e.,  $k = 2H = ma$ . It defines a critical wavenumber  $k_c$  which coincides the transition of the two distinct behaviors in the  $\psi$ DM spectrum. This  $k_c$  is the predecessor in the radiation-dominant era of the Jeans wavenumber  $k_J$  in the matter-dominant era.

(2) We demonstrate passive evolution of  $\psi$ DM to be a good approximation of the full treatment, and we also address the details of the full treatment, including collisionless neutrinos and Thomson scattering coupled photons and baryons, through which numerical solutions are obtained.



(3) As a bonus of our analyses, we show that the adiabatic condition for super-horizon perturbations holds instantaneously even when the field potential produces fast mass oscillations.

(4) The phase and amplitude of the complex  $\hat{\psi}$  are important quantities for any  $\psi$ DM simulation to start the initial condition faithfully in the matter dominant era. For this reason, we extend our numerical solutions into the matter-dominant era and compute the phase of  $\hat{\psi}$  and the power spectrum beyond the radiation-matter equality.

(5) We also consider perturbations of the axion model, a plausible extension of the free-particle model of  $\psi$ DM. It is found that the evolution of axion perturbations is generally almost identical to that of free-particle perturbations, except for the extreme case, called the extreme axion mode, where the initial value of the axion angle is near the field potential top.

(6) Three unexpected features of the extreme axion model are explored. Among them, the parametric drive and amplification mechanism accounts for two non-trivial features. To illustrate of the mechanisms, we show that upon neglecting the Hubble friction, the original perturbed field equation can be made equivalent to Mathieu's equation, which is able to faithfully recover the two features.



# Chapter 12

## Discussion and Perspective

In Part I, we have explored a new test problem, a fully three-dimensional MHD equilibrium of the Arnold-Beltrami-Childress (ABC) force-free magnetic field configuration, for testing the scaling of overall computation performance. This study yields a physics result consistent with the Taylor’s conjecture that higher-energy MHD equilibrium unstable to instabilities can relax to a unique lowest-energy force-free state preserving the magnetic helicity. This unique configuration is attainable after a turbulent phase, through which small-scale linkages of tangled magnetic fields are broken via reconnection, and the system finally reaches a configuration with large-scale current-carrying force-free field, rather than a current-free potential field. This minimum energy state still carries current due to a global field line linkage constraint, i.e., a constant global magnetic helicity, which is a topological constraint that limits the minimum energy the system can assume. We also find a new 3D magnetic ”patch” reconnection during turbulent relaxation, a finding that is very different from the thin-tube reconnection associated with the magnetic separators (Parnell and Haynes, 2010), where the separator is a field line connecting two magnetic null points and itself has a weak field. Figure (5.13) reveals that our 3D reconnection indeed lies on two current sheets. Whether the sheet structure is generic in 3D magnetic reconnection remains to be investigated.

In Part II, the two nontrivial features, i.e., extension of spectral cutoff to higher wave number and spectral excess of the extreme axion model can have important impacts in structure formation of the high- $z$ , matter-dominant universe, due to the fact that most

first-generation galaxies formed out of perturbations near the spectral cutoff. The spectral cutoff is determined solely by particle mass in the free-particle model. Its extension to higher  $k$  for the extreme axion model mimics the effect of higher particles mass for free particle. Therefore, the high- $k$  power spectrum may not be a good indicator accurately reflecting the true particle mass in the extreme axion model. Recent simulations addressing the high-redshift Lyman- $\alpha$  absorption features indicate that substantially higher particle mass than  $10^{-22}$ eV is required or implied (Armengaud et al., 2017; Iršič et al., 2017). On the other hand, approximately  $10^{-22}$ eV particle mass is needed to account for the flat cores of dwarf spheroidal galaxies (Schive et al., 2014; Chen et al., 2017). The tension in particle mass may be lessened with the extreme axion model.

However we have found a limit to the high- $k$  spectral extensions, no matter how extreme a condition the initial angle assumes. The spectral extensions are all confined to wave numbers less than a factor 2 higher from that of the free-particle model, i.e., approximately  $< k_c$ . That is, the spectral excess peaks around  $0.6 - 0.8k_c$  and immediately following the spectral peak is a sharp cutoff. This spectral shape renders the first collapsed halo of mass  $[(4\pi/3)(\pi/k)^3]\rho_0 \sim 10^{10}M_\odot$ , where  $k$  is near the peak of the spectral excess and  $\rho_0$  is the background mass density. As a reference, the first galaxies in the free-particle axion model of  $m = 10^{-22}$  eV have masses several  $\times 10^{10}M_\odot$  (Schive et al., 2016).

The spectral excess is perhaps our most surprising finding, since conventional dark matter candidates proposed so far are unable to produce power excess over the CDM model across the perturbation spectrum. When  $\delta\theta_0 < 1$  degree, the spectral excess can be so distinct that may completely revise the standard scenario of first galaxy formation. First of all, the spectral excess leads to earlier formation of first generation galaxies and push the reionization epoch (Ade et al., 2016) earlier than the free-particle model (Schive et al., 2016). Second, taking the more extreme case  $\theta_0 = 0.2$  degree as an example, c.f., Fig. (10.3), the broad spectral peak yields first collapsed halo of mass  $10^9 - 10^{10}M_\odot$ , and frequent major of these over-abundant first halos than the conventional are to quickly build up more massive halos. Indeed, this is what happens shown in a very recent study (Schive and Chiueh, 2017). Furthermore, busy major mergers are prone to sustain intense

star bursts and even rapid super-massive black hole growths. Finding quasar at  $z = 7$  (Mortlock et al., 2011) and recent discovery of quiescent galaxies more massive than the Milky Way inferred to already form at  $z = 5 - 7$  (Glazebrook et al., 2017) have posed challenges for the CDM model. Given the aforementioned possible outcomes, the extreme axion model may stand a better chance to meet such a challenges. Whether successful or not, only future detailed hydrodynamical simulations can tell.

To place our results in a concrete ground, we provide a formula for the wave number of spectral peak  $k_{peak}$  and a procedure for the peak height to be calculated, as functions of the initial angle and the particle mass in Appendix D.





## Appendix A

# Linear Stability Analysis of the ABC Magnetic Field Configuration

In this appendix, the stability of a uniform plasma with the ABC-flow pattern of the magnetic field in a unit cube subjected to the periodic boundary condition will be derived. The magnetic field, denoted by  $\mathbf{B}_0 (= (Bx, By, Bz))$  has the following form,

$$\begin{aligned} Bx &= A \sin(2\pi nz) + C \cos(2\pi ny), \\ By &= B \sin(2\pi nx) + A \cos(2\pi nz), \\ Bz &= C \sin(2\pi ny) + B \cos(2\pi nx), \end{aligned} \tag{A.1}$$

where  $A$ ,  $B$  and  $C$  are constants. Here  $n$  is an integer and we have a period- $n$  magnetic field. The density  $\rho_0$  and Pressure  $P_0$  are uniform, and the plasma is at rest everywhere. Note that the current density  $\mathbf{J}_0 \equiv \nabla \times \mathbf{B}_0 = 2\pi n \mathbf{B}_0$ , meaning no Lorentz force and an equilibrium plasma.

The linear stability is revealed by applying time-domain Fourier transformation on linearized MHD equation, yielding the eigenvalue problem:

$$-\rho_0 \omega^2 \boldsymbol{\xi} = \gamma P_0 \nabla^2 \boldsymbol{\xi} + \alpha_n \mathbf{B}_0 \times [\nabla \times (\boldsymbol{\xi} \times \mathbf{B}_0)] + \{\nabla \times [\nabla \times (\boldsymbol{\xi} \times \mathbf{B}_0)]\} \times \mathbf{B}_0, \tag{A.2}$$

where  $\boldsymbol{\xi}$  is the displacement defined as  $-i\omega \boldsymbol{\xi} \equiv \boldsymbol{\delta v}$  with the perturbed velocity field  $\boldsymbol{\delta v}$ ,



and  $\alpha_n \equiv 2\pi n$ .

Note that the right hand side of Eq. (A.2) is a Hermitian operator respect to the eigenfunction  $\xi$ . Therefore, eigenvalues of Eq. (A.2) ( $\rho_0\omega^2$ ) are real and the corresponding eigenfunctions are orthonormal. The system is stable if and only if all eigenvalues are positive.

We shall use the variational (energy) principle to prove the stability. Multiplying  $\xi^*$ , the complex conjugate of  $\xi$ , on both sides of Eq. (A.2) and then integrating both sides with the whole domain, we come up with

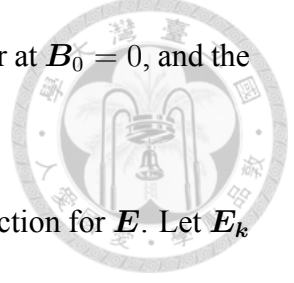
$$\begin{aligned} \rho_0\omega^2 \int_{\Omega} |\xi|^2 d^3x &= \gamma P_0 \int_{\Omega} |\nabla \cdot \xi|^2 d^3x + \\ &\quad \int_{\Omega} |\nabla \times (\xi \times \mathbf{B}_0)|^2 d^3x - \alpha_n \int_{\Omega} (\xi^* \times \mathbf{B}_0) \cdot [\nabla \times (\xi \times \mathbf{B}_0)] d^3x, \end{aligned} \quad (\text{A.3})$$

where  $\Omega$  is the whole domain. Here the boundary condition is applied to eliminate boundary integral terms. Hence the necessary and sufficient condition for stability becomes the right hand side of Eq. (A.3) to be positive definite for any displacement  $\xi$ .

In the following we shall first show that when the space is continuous and isotropic, a general result can be obtained. We then proceed to the restricted situation where the space is a periodic cube, a realistic situation for simulations.

We now examine the stability of the  $n = 1$  state, i.e.,  $\alpha_n = 2\pi$ . The first term on the right hand side of Eq. (A.3) is the compressional term and positive definite, and therefore we only need to examine the last two terms. We define  $\mathbf{E} \equiv \xi \times \mathbf{B}_0$ , where  $i\omega \mathbf{E}$  is the electric field. When only the last two terms on the right hand side of Eq. (A.3) are considered, they can be regarded as functionals of  $\mathbf{E}$ .

The trivial marginally stable perturbation is  $\mathbf{E} = 0$  and the displacement is parallel to the field. More generally the mode has a displacement  $\xi \times \mathbf{B}_0 = \mathbf{C}$  for some constant vector  $\mathbf{C}$ . When  $\mathbf{C} = 0$ , it implies a field-aligned displacement  $\xi = f(\mathbf{x})\mathbf{B}_0$  for some scalar function  $f(\mathbf{x})$ . Furthermore, if the displacement is incompressible, i.e.,  $\nabla \cdot \xi = 0$ , we can have a marginal stability. That is, the scalar function  $f(\mathbf{x})$  is to satisfy  $\mathbf{B}_0 \cdot \nabla f = 0$ , meaning that the value of  $f$  remains constant along any field line and different magnetic field lines may have different values of  $f$ . This ground state equilibrium  $\mathbf{B}_0$  has



8 points where the magnetic field vanishes, and if  $\mathbf{C} \neq 0$ ,  $\boldsymbol{\xi}$  is singular at  $B_0 = 0$ , and the compressional integral diverges and thus it becomes vastly stable.

The non-trivial solution is the plane wave, which is the eigenfunction for  $\mathbf{E}$ . Let  $\mathbf{E}_k$  be the Fourier components  $\mathbf{E}$ , and the integrand becomes

$$|\mathbf{k} \times \mathbf{E}_k|^2 + \alpha_n \Im[\mathbf{k} \cdot (\mathbf{E}_k^* \times \mathbf{E}_k)] = (\mathbf{k} \times \mathbf{A})^2 + (\mathbf{k} \times \mathbf{D})^2 + 2\alpha_n \mathbf{k} \cdot (\mathbf{A} \times \mathbf{D}), \quad (\text{A.4})$$

where  $\mathbf{A} = \Re[\mathbf{E}_k]$  and  $\mathbf{D} = \Im[\mathbf{E}_k]$ . Now we let  $\mathbf{A}$  and  $\mathbf{D}$  lie on the  $x - y$  plane and suspend an angle  $\theta$  from each other. That is, the first term is  $k_z^2(A^2 + D^2) + k_x^2(A_y^2 + D_y^2) + k_y^2(A_x^2 + D_x^2)$  and the second terms is  $2\alpha_n k_z A D \sin \theta$ , where  $A \equiv |\mathbf{A}|$  and  $D \equiv |\mathbf{D}|$ . Minimizing the two terms, we find the second term is most negative when (i)  $\theta = -\pi/2$  and (ii)  $k = k_z$ . Condition (ii) also minimizes the positive-definite first term. The remaining terms become

$$(kA + \alpha_n D)^2 + (k^2 - \alpha_n^2)2D^2. \quad (\text{A.5})$$

The marginally stable mode can thus be  $\alpha_n = \pm k$  and  $A = \mp D$ . This is a circularly polarized wave for the electric field.

There is in fact one more possible marginally stable eigen-mode. That is,  $\mathbf{k} \times \mathbf{A} = 0$  and  $\mathbf{k} \times \mathbf{D} = 0$ , meaning  $\mathbf{k}$ ,  $\mathbf{A}$  and  $\mathbf{D}$  are all parallel, and therefore all three terms in Eq. (A.4) separately vanish. It corresponds to the longitudinal electric field eigen-mode.

To address the compressional contribution to the remaining energy, we first consider the longitudinal electric field. We first sum up the Fourier components of  $\mathbf{E}_k$ . We let  $\mathbf{E}_k = i\mathbf{k}g_k$ , and the real-space electric field becomes

$$\mathbf{E}(\mathbf{x}) = \nabla g(\mathbf{x}), \quad (\text{A.6})$$

where  $g_k$  is the Fourier component of  $g(\mathbf{x}) = |\mathbf{B}_0|^2 h(\mathbf{x})$ . As the electric field is only determined by the perpendicular component of the displacement,  $\boldsymbol{\xi}_\perp(\mathbf{x})$ , we can thus relate

it to  $|\mathbf{B}_0|^2 h(\mathbf{x})$  via

$$\boldsymbol{\xi}_{\perp} = \mathbf{B}_0 \times \nabla h + 2h \mathbf{B}_0 \times \nabla \ln |\mathbf{B}_0|. \quad (\text{A.7})$$

Now,  $\nabla \cdot \boldsymbol{\xi} = \nabla \cdot (\boldsymbol{\xi}_{\perp} + \boldsymbol{\xi}_{\parallel})$  and the first term becomes

$$\nabla \cdot \boldsymbol{\xi}_{\perp} = \alpha_n (\mathbf{B}_0 \cdot \nabla h + h \mathbf{B}_0 \cdot \nabla \ln |\mathbf{B}_0|^2) + (\mathbf{B}_0 \times \nabla \ln |\mathbf{B}_0|^2) \cdot \nabla h. \quad (\text{A.8})$$

On the other hand, the second term, as before, is  $\nabla \cdot \boldsymbol{\xi}_{\parallel} = \mathbf{B}_0 \cdot \nabla f$ . To have zero compression, we must demand

$$\mathbf{B}_0 \cdot \nabla f + \alpha_n (\mathbf{B}_0 \cdot \nabla h + h \mathbf{B}_0 \cdot \nabla \ln |\mathbf{B}_0|^2) + (\mathbf{B}_0 \times \nabla \ln |\mathbf{B}_0|^2) \cdot \nabla h = 0. \quad (\text{A.9})$$

Having two degrees of freedom,  $f$  and  $h$ , the solution is unique and a solution can be obtain quite easily. For example, let  $h = \beta |\mathbf{B}_0|^2$ , where  $\beta$  is a constant, and we find

$$\mathbf{B}_0 \cdot \nabla f = -\mathbf{B}_0 \cdot \nabla (2\alpha_n \beta |\mathbf{B}_0|^2), \quad (\text{A.10})$$

yielding a regular solution  $f = -2\alpha_n \beta |\mathbf{B}_0|^2$ .

The minimum magnetic energy circular polarization electric field modes must have wavenumbers  $k = \pm \alpha_n$ , thus long-wavelength modes with wavenumbers on a spherical shell. These modes are likely unable to make displacements compression-free and become marginally stable, and we will leave it in a future work.

In sum, the marginally stable non-trivial eigen-modes are the longitudinal electric field and the trivial eigen-mode the field-aligned displacement. On the other hand, the condition for instability demands  $k^2 < \alpha_n^2$ , as it makes the magnetic energy negative by choosing a trial function, for example,  $A = -(\alpha_n/k)D$  with  $D \neq 0$ .

The above provides a general result. Next let's consider a restricted simulation space where the system is confined in a periodic cubic box,  $[0, 1] \times [0, 1] \times [0, 1]$ , and the space is discrete. Due to the periodic boundary condition, the quantity  $\mathbf{E}$  can be expanded as  $\sum_{j,l,m \in Z} \tilde{\mathbf{E}}_{j,l,m} \exp[i2\pi(jx + ly + mz)]$ , where  $Z$  is the set of all integer numbers. It





follows,

$$\begin{aligned} & \int_{\Omega} |\nabla \times (\boldsymbol{\xi} \times \mathbf{B}_0)|^2 d^3 \mathbf{x} - \alpha_n \int_{\Omega} (\boldsymbol{\xi}^* \times \mathbf{B}_0) \cdot [\nabla \times (\boldsymbol{\xi} \times \mathbf{B}_0)] d^3 \mathbf{x} \\ &= 4\pi^2 \sum_{j,l,m \in Z} [|\mathbf{k}_{j,l,m} \times \tilde{\mathbf{E}}_{j,l,m}|^2 - i(\mathbf{k}_{j,l,m} \times \tilde{\mathbf{E}}_{j,l,m}) \cdot \tilde{\mathbf{E}}_{j,l,m}^*] \equiv 4\pi^2 \sum_{j,l,m \in Z} A_{j,l,m}, \end{aligned} \quad (\text{A.11})$$

where  $A_{j,l,m} \equiv |\mathbf{k}_{j,l,m} \times \tilde{\mathbf{E}}_{j,l,m}|^2 - i(\mathbf{k}_{j,l,m} \times \tilde{\mathbf{E}}_{j,l,m}) \cdot \tilde{\mathbf{E}}_{j,l,m}^*$  and  $k_{j,l,m} \equiv (j, l, m)$ . Hereafter we will show  $A_{j,l,m} \geq 0$  for any  $(j, l, m)$  so the ground state ( $\alpha_n = 2\pi$ ) is stable.

Let  $\tilde{\mathbf{E}}_{j,l,m}$  be  $(e_1, e_2, e_3)$ , where  $e_1, e_2$  and  $e_3$  are complex and functions of  $(j, l, m)$ .

It follows

$$\begin{aligned} A_{j,l,m} = & |le_3 - me_2|^2 + |je_3 - me_1|^2 + |je_2 - le_1|^2 - \\ & i[j(e_2 e_3^* - e_2^* e_3) + l(e_3 e_1^* - e_3^* e_1) + m(e_1 e_2^* - e_1^* e_2)]. \end{aligned} \quad (\text{A.12})$$

We note that  $A_{j,l,m}$  is  $U(1)$  symmetric, i.e.,  $A_{j,l,m}$  remains the same under the transformation:  $e_1 \rightarrow e_1 \exp(i\theta)$ ,  $e_2 \rightarrow e_2 \exp(i\theta)$  and  $e_3 \rightarrow e_3 \exp(i\theta)$  with  $\theta \in [0, 2\pi]$ . This property will be used in the following argument.

We decompose  $(j, l, m)$  into following four cases.

(i)  $j = l = m = 0$

The quantity  $A_{j,l,m} = 0$  can minimize the magnetic energy and this trivial eigenfunction corresponds to the field-aligned displacement.

(ii) Only one of  $j, l$  and  $m$  is non-zero

Without loss of generality, we assume  $j \neq 0$  and  $l = m = 0$ . Therefore  $A_{j,l,m}$  becomes

$$A_{j,l,m} = j^2|e_2|^2 + j^2|e_3|^2 - i[j(e_2 e_3^* - e_2^* e_3)]. \quad (\text{A.13})$$

By the  $U(1)$  symmetry, we can let  $e_2 = |e_2|$  and  $e_3 = |e_3| \exp(i\theta_3)$  with  $\theta_3 \in [0, 2\pi]$ .



Hence Eq.(A.13) becomes

$$\begin{aligned}
A_{j,l,m} &= j^2|e_2|^2 + j^2|e_3|^2 - 2j|e_2||e_3|\sin(\theta_3) \\
&= j^2\left[|e_2|^2 + |e_3|^2 - \frac{2}{j}|e_2||e_3|\sin(\theta_3)\right] \\
&\geq j^2\left(|e_2|^2 + |e_3|^2 - \frac{2}{|j|}|e_2||e_3|\right) \\
&\geq j^2(|e_2|^2 + |e_3|^2 - 2|e_2||e_3|) \\
&= j^2(|e_2| - |e_3|)^2 \geq 0.
\end{aligned} \tag{A.14}$$

Here the first inequality is based on  $-1 \leq \sin(\theta_3) \leq 1$  and the second one is from  $|j| \geq 1$ . Therefore  $A_{j,l,m}$  is always greater than zero and hence the modes are stable.

The minimum magnetic energy modes can be attained in the following two situations. First, it is achieved by  $e_2 = e_3 = 0$  and  $e_1 \neq 0$ . This setting makes Eq. (A.14) be zero automatically. There is no constraints on the wavenumber  $j$  so this minimum magnetic energy state permits small scale fluctuations. Furthermore, since the only non-vanishing  $e_1$  is parallel to the wave propagation, it corresponds to a longitudinal electric field.

The second situation is followed by Eq. (A.14). The equality in Eq. (A.14) holds if and only if  $|e_2| = |e_3| \neq 0$  and  $j = 1$  for  $\theta_3 = \pi/2$  or  $j = -1$  for  $\theta_3 = -\pi/2$ . This situation only permits the longest wavelength mode, i.e.,  $|j| = 1$ . Due to the fact  $|\theta_3| = \pi/2$ , the condition leads to the right-handed circularly polarized waves ( $j = 1$  for  $\theta_3 = \pi/2$  or  $j = -1$  for  $\theta_3 = -\pi/2$ ). The minimum magnetic energy mode favors the right-handed circularly polarized wave is because the magnetic helicity of the background magnetic field is right-handed. If we trivially change the parameter  $\alpha_n \rightarrow -\alpha_n$ , everything will be left-handed.

(iii) One of  $j, l$  and  $m$  is zero.

Again, we can consider only the case of  $j = 0, l \neq 0$  and  $m \neq 0$ . As before, we now choose the phase angle such that  $e_1 = |e_1|$ . In order to simplify the notation, we rescale

$e_2$  by the factor  $m$  and  $e_3$  by the factor  $l$ , i.e.  $e_2 \rightarrow me_2$  and  $e_3 \rightarrow le_3$ . It follows

$$\begin{aligned}
A_{j,l,m} &= |e_2 - e_3|^2 + m^2|e_1|^2 + l^2|e_1|^2 - i(e_3e_1^* - e_3^*e_1 + e_1e_2^* - e_1^*e_2) \\
&= [\Re(e_2) - \Re(e_3)]^2 + [\Im(e_2) - \Im(e_3)]^2 + (m^2 + l^2)|e_1|^2 + 2\Im(e_3)|e_1| - 2\Im(e_2)|e_1| \\
&= [\Re(e_2) - \Re(e_3)]^2 + [\Im(e_2) - \Im(e_3) - |e_1|]^2 + (m^2 + l^2 - 1)|e_1|^2 \\
&\geq 0,
\end{aligned} \tag{A.15}$$

where  $\Re$  stands for the real part and  $\Im$  the imagine part. Here the last inequality arises from  $l, m \geq 1$ .

The minimum magnetic energy mode is achieved by letting  $e_1 = 0$  and  $me_2 = le_3$ . This makes  $\tilde{\mathbf{E}}_{j,l,m}$  parallel to the propagation direction ( $(e_2, e_3) = c(l, m)$  for some constant  $c$ ), which is the longitudinal electric field mode. On the other hand, the circular polarization eigen-mode in this case is not the minimum magnetic energy mode since  $l$  and  $m$  are non-zero and it is not the longest wavelength mode. Therefore this case does not have minimum magnetic energy mode.

(iv) All of  $j, l$  and  $m$  are non-zeros

In this case, we follow the convention in case (iii), i.e.,  $e_1 = |e_1|$ ,  $e_2 \rightarrow me_2$  and  $e_3 \rightarrow le_3$ . Therefore  $A_{j,l,m}$  becomes

$$A_{j,l,m} = X^T M X + 2|e_1|Q^T X + (m^2 + l^2)|e_1|^2, \tag{A.16}$$

where

$$X = \begin{bmatrix} \Re(e_2) \\ \Im(e_2) \\ \Re(e_3) \\ \Im(e_3) \end{bmatrix}, Q = \begin{bmatrix} -\frac{jl}{m} \\ -1 \\ -\frac{jm}{l} \\ 1 \end{bmatrix}, \tag{A.17}$$



and

$$M = \begin{bmatrix} 1 + \left(\frac{j}{m}\right)^2 & 0 & -1 & -\frac{j}{ml} \\ 0 & 1 + \left(\frac{j}{m}\right)^2 & \frac{j}{ml} & -1 \\ -1 & \frac{j}{ml} & 1 + \left(\frac{j}{l}\right)^2 & 0 \\ -\frac{j}{ml} & -1 & 0 & 1 + \left(\frac{j}{l}\right)^2 \end{bmatrix}. \quad (\text{A.18})$$

Here the superscript  $T$  is the transpose of a given matrix. Since the matrix  $M$  is symmetric, it can be diagonalized, i.e.,  $M = S\Lambda S^T$  with an unitary matrix  $S$  and a diagonal matrix  $\Lambda$ . Next we let  $\tilde{X}$  be  $S^T X$  and  $\tilde{Q}$  be  $S^T Q$ , Equation (A.16) becomes

$$A_{j,l,m} = (\tilde{X} + |e_1|\Lambda^{-1}\tilde{Q})^T \Lambda (\tilde{X} + |e_1|\Lambda^{-1}\tilde{Q}) + (m^2 + l^2 - Q^T M^{-1} Q)|e_1|^2. \quad (\text{A.19})$$

On the other hand, the matrix  $\Lambda$  has the following form

$$\Lambda = \begin{bmatrix} \lambda_+ & 0 & 0 & 0 \\ 0 & \lambda_+ & 0 & 0 \\ 0 & 0 & \lambda_- & 0 \\ 0 & 0 & 0 & \lambda_- \end{bmatrix}, \quad (\text{A.20})$$

with

$$\lambda_{\pm} = \frac{1}{2} \left[ 2 + \left(\frac{j}{m}\right)^2 + \left(\frac{j}{l}\right)^2 \pm \sqrt{4 + \left(\frac{j^2}{m^2} - \frac{j^2}{l^2}\right)^2 + \left(\frac{2j}{ml}\right)^2} \right]. \quad (\text{A.21})$$

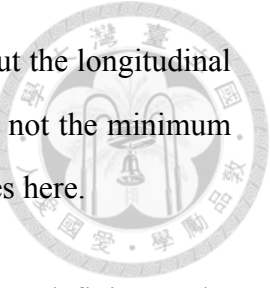
A straightforward calculation shows  $Q^T M^{-1} Q = m^2 + l^2$ , meaning that the second term in Eq. (A.19) is zero. Hence Eq. (A.19) becomes

$$A_{j,l,m} = (\tilde{X} + |e_1|\Lambda^{-1}\tilde{Q})^T \Lambda (\tilde{X} + |e_1|\Lambda^{-1}\tilde{Q}). \quad (\text{A.22})$$

It is noted that  $\lambda_+ \geq \lambda_- \geq 0$ . The positive  $\Lambda$  makes the right hand side of Eq. (A.22) positive definite. Therefore, the quantity  $A_{j,l,m}$  is always positive.

The minimal magnetic energy state can be obtained when  $\tilde{X} + |e_1|\Lambda^{-1}\tilde{Q} = 0$ . It is equivalent to  $X = -M^{-1}Q|e_1|$ . A straightforward calculation yields that  $\Im(e_2) =$

$\Im(e_3) = 0$ ,  $\Re(e_2) = (l/n)|e_1|$  and  $\Re(e_3) = (m/n)|e_1|$ . It is nothing but the longitudinal electric field mode. On the other hand, the circular-polarized mode is not the minimum magnetic energy mode, as the argument applied to case (iii) also applies here.



Combining all above cases, it follows that Eq. (A.11) is positive definite so the ground state ( $\alpha_n = 2\pi$ ) is stable. The only marginally stable mode that we have so far proved and that makes all terms in the energy integral vanishes is the trivial mode where the displacement is parallel to the equilibrium magnetic field. The longitudinal mode, with a suitable linear combination, may potentially become marginally stable, but we so far have no proof. Both modes can be of small scale. We suspect that the ideal MHD marginally stable mode may be most vulnerable to resistivity instability (Rosenbluth et al., 1973) in the presence of small numerical dissipation.





## Appendix B

### Passive Evolution

In this appendix, governing equations and analytic solutions for passive evolution are presented.

The action can be written as follows,

$$S = \int d^4x \sqrt{|g|} \left[ \frac{R}{16\pi G} + L_M \right], \quad (\text{B.1})$$

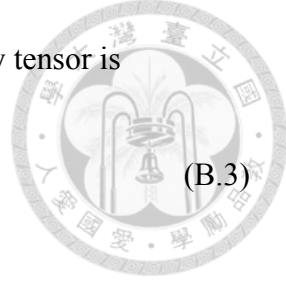
where  $g$  is the determinant of the metric  $g_{\mu\nu}$ ,  $R$  the scalar curvature,  $L_M$  the Lagrangian density of matter and  $G$  the gravitational constant. Here we choose the speed of light and the Planck constant  $\hbar$  to be 1.

The Lagrangian density  $L_M$  consists of two components, the radiation fluid and the dark matter. The radiation can be described as a perfect fluid with the equation of state  $P = \epsilon/3$ , where  $P$  is the pressure and  $\epsilon$  is the energy density. On the other hand, two different dark matter models, the cold dark matter (CDM) model and the  $\psi$  dark matter ( $\psi$ DM), will be introduced. CDM is a pressureless perfect fluid, and  $\psi$ DM is a spin-zero real scalar field with a Lagrangian density

$$L_\psi = \frac{1}{2} g^{\mu\nu} \partial_\mu \psi \partial_\nu \psi - V(\psi), \quad (\text{B.2})$$

where  $V$  is the scalar field potential. The corresponding stress-energy tensor is

$$T_{\mu\nu}^\psi = \frac{-2}{\sqrt{|g|}} \frac{\delta(\sqrt{|g|}L_\psi)}{\delta g^{\mu\nu}}. \quad (\text{B.3})$$



The metric is the flat Friedmann-Lemaitre-Robertson-Walker (FLRW) metric with the scalar metric perturbation, i.e.,

$$ds^2 = a^2(\tau) \{ [1 + 2\phi(x^i, \tau)] d\tau^2 - [1 - 2\phi(x^i, \tau)] \delta_{ij} dx^i dx^j \}, \quad (\text{B.4})$$

where  $\tau$  is the conformal time,  $x^i$  with  $i = 1, 2, 3$  is the comoving coordinate,  $\phi$  the metric perturbation,  $a$  the scale factor,  $\delta_{ij}$  the Kronecker delta function, and the Newtonian gauge has been chosen. Similarly, the energy-momentum stress tensor is also written as a uniform background with a small perturbation. Thus  $\psi$ DM field can be expressed as  $\Psi(\tau) + \psi(x^i, \tau)$  for calculating the corresponding stress-energy tensor.

Gathering the above and substituting into Eq. (B.1) and applying Euler-Lagrange equation, one obtains the Einstein equations and the conservation of energy and momentum.

The zeroth order equations are just Friedmann equations,

$$H^2 = \frac{8\pi G}{3} a^2 (\epsilon_\gamma + \epsilon_D), \quad (\text{B.5})$$

$$H' - H^2 = -4\pi G a^2 [(\epsilon_\gamma + P_\gamma) + (\epsilon_D + P_D)], \quad (\text{B.6})$$

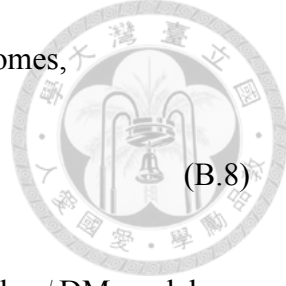
with the following conservation laws,

$$\dot{\epsilon}_\alpha + 3H(\epsilon_\alpha + P_\alpha) = 0, \quad \alpha = \gamma, D, \quad (\text{B.7})$$

where  $(\cdot)'$  is the derivative with respect to  $\tau$ ,  $H \equiv a'/a$  the Hubble parameter, and the subscript denotes different components. Here we use  $\gamma$  to denote the radiation fluid and  $D$  the dark matter.

For the CDM model, the pressure  $P_D$  is zero, and Eq. (B.7) becomes,

$$\epsilon_C' + 3H\epsilon_C = 0, \quad (\text{B.8})$$



where we have changed the subscript "D" to "C" to label CDM. For the  $\psi$ DM model, we have the following relations

$$\epsilon_\psi = \frac{1}{2} \frac{(\Psi')^2}{a^2} + V(\Psi), \quad (\text{B.9})$$

$$P_\psi = \frac{1}{2} \frac{(\Psi')^2}{a^2} - V(\Psi), \quad (\text{B.10})$$

where the subscript " $\psi$ " is used to replace "D". These relations can be obtained by Eq. (B.3). Substituting Eqs. (B.9) and (B.10) into Eq. (B.7), it follows that

$$\Psi'' + 2H\Psi' + a^2 \frac{dV}{d\Psi} \Big|_\Psi = 0. \quad (\text{B.11})$$

The first order perturbed equations consist of the perturbed Einstein equations

$$-k^2\phi - 3H(\phi' + H\phi) = 4\pi G a^2(\delta\epsilon_\gamma + \delta\epsilon_D), \quad (\text{B.12})$$

$$\phi' + H\phi = -4\pi G a^2[(\epsilon_\gamma + P_\gamma)\theta_\gamma + (\epsilon_D + P_D)\theta_D], \quad (\text{B.13})$$

the continuity equation

$$\delta_\alpha' + 3H\left(\frac{\delta P_\alpha}{\delta\epsilon_\alpha} - \frac{P_\alpha}{\epsilon_\alpha}\right)\delta_\alpha = \left(1 + \frac{P_\alpha}{\epsilon_\alpha}\right)(k^2\theta_\alpha + 3\phi'), \quad (\text{B.14})$$

$\alpha = \gamma, D,$

and the Euler equation

$$\theta_\alpha' + 3H\left(\frac{1}{3} - \frac{P'_\alpha}{\epsilon'_\alpha}\right)\theta_\alpha = -\frac{\delta P_\alpha}{\epsilon_\alpha + P_\alpha} - \phi, \quad \alpha = \gamma, D. \quad (\text{B.15})$$

Here  $\delta\epsilon_\alpha$ ,  $\delta P_\alpha$  and  $\theta_\alpha$  are the energy density perturbation, the pressure perturbation and the velocity potential of the  $\alpha$  species, respectively. The quantity  $\delta_\alpha$  is the fractional over-density of the  $\alpha$  species defined as  $\delta_\alpha \equiv \delta\epsilon_\alpha/\epsilon_\alpha$ . The spatial Fourier transformation has

been applied in the comoving coordinate on Eqs. (B.12), (B.13), (B.14) and (B.15).

For the CDM model,  $P_D = \delta P_D = 0$ , Eqs. (B.14) and (B.15) become

$$\delta'_C = k^2 \theta_C + 3\phi', \quad (\text{B.16})$$

$$\theta'_C + H\theta_C = -\phi. \quad (\text{B.17})$$

On the other hand for  $\psi$ DM, from Eq. (B.3), the quantities  $\delta\epsilon_D$ ,  $\delta P_D$  and  $\theta_D$  can be expressed as

$$\delta\epsilon_\psi = \frac{\Psi'\psi'}{a^2} + \frac{dV}{d\psi}\Big|_\Psi \psi - \frac{(\Psi')^2\phi}{a^2}, \quad (\text{B.18})$$

$$\delta P_\psi = \frac{\Psi'\psi'}{a^2} - \frac{dV}{d\psi}\Big|_\Psi \psi - \frac{(\Psi')^2\phi}{a^2}, \quad (\text{B.19})$$

$$\Psi'\theta_\psi = -\psi. \quad (\text{B.20})$$

Substituting Eqs. (B.18), (B.19) and (B.20) into Eq. (B.14), it follows that,

$$\psi'' + 2H\psi' + \left(k^2 + a^2 \frac{d^2V}{d\psi^2}\Big|_\Psi\right)\psi = 4\Psi'\phi' - 2a^2 \frac{dV}{d\psi}\Big|_\Psi \phi. \quad (\text{B.21})$$

In addition, the Euler equation (Eq. (B.15)) is reduced to Eq. (B.11), as shown in Chapter 8.

In the radiation-dominant era, the dark matter energy density is much smaller than the radiation energy density, so are the perturbed quantities. Under this condition, dark matter can be treated as passive particles (fields) tracing the geometry of universe that is determined by radiation, and therefore the dark matter contribution in Friedmann equations (Eq. (B.5) and (B.6)) and perturbed Einstein equations (Eqs. (B.12) and (B.13)) can be ignored.

The form of scalar field potential  $V(\psi)$  should be specified. For a non-self-interacting free field, we have  $V(\psi) = m^2\psi^2/2$ , where  $m$  is the mass of the dark matter particle.

First, we should solve the zeroth order equations. From Eq. (B.7) for the photon fluid, the photon energy density  $\epsilon_\gamma \propto a^{-4}$  due to  $3P_\gamma = \epsilon_\gamma$ . Substituting the above relation into Friedmann's equations, we find  $a \propto \tau$  and  $H \propto a^{-1}$ .

When the CDM model is considered, it is straightforward to find the energy density  $\epsilon_C \propto a^{-3}$ . For the  $\psi$ DM model, substituting above scalar potential  $V(\psi)$  into Eq. (B.11), Eq. (8.1) follows. It is natural to define a dimensionless quantity  $u_m = ma/2H$  which normalizes the time to the onset of mass oscillation. With above relations, Eq. (8.1) becomes

$$\frac{d^2\Psi}{du_m^2} + \frac{3}{2u_m} \frac{d\Psi}{du_m} + \Psi = 0. \quad (\text{B.22})$$

Equation (B.22) has following solution,

$$\Psi(u_m) = C_r^\Psi \Psi_r(u_m) + C_s^\Psi \Psi_s(u_m), \quad (\text{B.23})$$

where  $C_r^\Psi$  and  $C_s^\Psi$  are constants, and  $\Psi_r$  and  $\Psi_s$  are

$$\Psi_r(u_m) = 2^{\frac{1}{4}} \Gamma\left(\frac{5}{4}\right) \frac{J_{\frac{1}{4}}(u_m)}{u_m^{\frac{1}{4}}}, \quad (\text{B.24})$$

$$\Psi_s(u_m) = 2^{\frac{1}{4}} \Gamma\left(\frac{5}{4}\right) \frac{Y_{\frac{1}{4}}(u_m)}{u_m^{\frac{1}{4}}}, \quad (\text{B.25})$$

where  $\Gamma$  is the gamma function,  $J$  and  $Y$  are Bessel function of the first and second kind, respectively, which are orthogonal to each other. It is noted that  $\Psi_s$  has a singularity as  $u_m \rightarrow 0$  while  $\Psi_r$  remains regular, and hence only  $\Psi_r$  is the valid zero-order field.

When  $u_m \gg 1$ , the energy density  $\propto u_m^{-3/2} \propto a^{-3}$ . This means the energy density of  $\psi$ DM follows CDM after the mass oscillation. We further define  $\Psi_0 \equiv C_r^\Psi \Psi_r(0) = C_r^\Psi$ . In the following,  $C_r^\Psi$  will be replaced by  $\Psi_0$ .

Next, we turn to the first order perturbed equations. The metric perturbation  $\phi$  should be obtained first. To solve  $\phi$ , it is natural to define a dimensionless quantity  $u_k \equiv k/\sqrt{3}H$ . This quantity approximately measures the epoch of the horizon entry. Using the chain rule, Eq. (B.13) becomes

$$\frac{d\phi}{du_k} + \frac{\phi}{u_k} + \frac{g_\gamma}{2u_k} = 0, \quad (\text{B.26})$$

where  $g_\gamma \equiv 4H\theta_\gamma$ . On the other hand, from Eqs. (B.5), (B.6), (B.12), (B.13), (B.14) and (B.15) with the radiation fluid's equation of state  $P_\gamma = \epsilon_\gamma/3$  and  $\delta P_\gamma = \delta\epsilon_\gamma/3$ ,  $g_\gamma$  obeys



the following equation

$$\frac{dg_\gamma}{du_k} = \left(2u_k - \frac{4}{u_k}\right)\phi - \frac{2}{u_k}g_\gamma. \quad (\text{B.27})$$

Combining Eq. (B.26) and (B.27), one finds  $\phi$  satisfies the following second order equation

$$\frac{d^2\phi}{du_k^2} + \frac{4}{u_k} \frac{d\phi}{du_k} + \phi = 0. \quad (\text{B.28})$$

Equation (B.28) has a solution:

$$\phi = C_r^\phi \phi_r(u_k) + C_s^\phi \phi_s(u_k), \quad (\text{B.29})$$

where  $C_r^\phi$  and  $C_s^\phi$  are constants, and

$$\phi_r(u_k) = 3 \left[ -\frac{\cos(u_k)}{u_k^2} + \frac{\sin(u_k)}{u_k^3} \right], \quad (\text{B.30})$$

$$\phi_s(u_k) = 3 \left[ -\frac{\sin(u_k)}{u_k^2} - \frac{\cos(u_k)}{u_k^3} \right]. \quad (\text{B.31})$$

From Eqs. (B.14) and (B.15), the radiation energy perturbation  $\delta_\gamma$  becomes,

$$\delta_\gamma = C_r^\phi \delta_\gamma^r(u_k) + C_s^\phi \delta_\gamma^s(u_k), \quad (\text{B.32})$$

with

$$\delta_\gamma^r(u_k) = 3 \left[ 2\cos(u_k) - 4\frac{\sin(u_k)}{u_k} - 4\frac{\cos(u_k)}{u_k^2} + 4\frac{\sin(u_k)}{u_k^3} \right], \quad (\text{B.33})$$

$$\delta_\gamma^s(u_k) = 3 \left[ 2\sin(u_k) + 4\frac{\cos(u_k)}{u_k} - 4\frac{\sin(u_k)}{u_k^2} - 4\frac{\cos(u_k)}{u_k^3} \right]. \quad (\text{B.34})$$

Since  $\phi_s$  and  $\delta_\gamma^s$  have a singularity at  $u_k = 0$ , only the regular modes,  $\phi_r$  and  $\delta_\gamma^r$ , are retained. Similar to the  $\psi$ DM background field case, we can define  $\phi_0 \equiv C_r^\phi \phi_r(0) = C_r^\phi$ . In the following,  $C_r^\phi$  will be replaced by  $\phi_0$ .

It is noted that  $\phi(u_k) = \phi_0(1 + O(u_k^2))$ , dominated by a constant  $\phi_0$ . On the other hand, from Eq. (8.12) ignoring the dark matter contribution, the gauge covariant photon energy density perturbation grows as  $\Delta_\gamma \propto u_k^2 \propto a^2$  before entering horizon.

Moreover, from Eq. (B.33),  $\delta_\gamma(u_k) = \phi_0(-2 + O(u_k^2))$ , when  $u_k \ll 1$ . This relation

is used in the discussion of phase (ia) in Section 9.1.



The perturbed dark matter equations are solvable once the background solution and the metric perturbation are given. For CDM model, Eqs. (B.16) and (B.17) become

$$\frac{d\delta_C}{du_k} = u_k g_C + 3 \frac{d\phi}{du_k}, \quad (\text{B.35})$$

$$\frac{dg_C}{du_k} + 2 \frac{g_C}{u_k} = -3 \frac{\phi}{u_k}, \quad (\text{B.36})$$

where  $g_C \equiv 3H\theta_C$  and the metric perturbation  $\phi = \phi_0\phi_r(u_k)$ . It is straightforward to solve Eq. (B.36) for the solution of  $g_C$ , as

$$g_C(u_k) = -9\phi_0 \left[ \frac{1}{u_k^2} - \frac{\sin(u_k)}{u_k^3} \right]. \quad (\text{B.37})$$

Here the homogeneous solution of  $g_C$  has been dropped since it has the singularity at  $u_k = 0$ . Substituting Eq. (B.37) into Eq. (B.35) and integrating on both sides, one obtains

$$\delta_C(u_k) = -9\phi_0 \left[ \frac{\sin(u_k)}{u_k} + \frac{\cos(u_k)}{u_k^2} - \frac{\sin(u_k)}{u_k^3} + \ln(u_k) - Ci(u_k) + \gamma - \frac{1}{2} \right], \quad (\text{B.38})$$

where  $Ci(u_k)$  is the cosine integral function and  $\gamma$  is the Euler-Mascheroni constant. The last term,  $1/2$ , is fixed by the adiabatic condition (Eq. (9.4)). Finally, the gauge covariant energy perturbation  $\Delta_C$  is obtained to be

$$\Delta_C = \delta_C - g_C = -9\phi_0 \left[ \frac{\sin(u_k)}{u_k} + \frac{\cos(u_k) - 1}{u_k^2} + \ln(u_k) - Ci(u_k) + \gamma - \frac{1}{2} \right]. \quad (\text{B.39})$$

For  $\psi$ DM model, Eq. (B.21) becomes Eq. (8.2) for free particle. Using  $u_m$  as the argument, Eq. (8.2) further becomes

$$\frac{d^2\psi}{du_m^2} + \frac{3}{2u_m} \frac{d\psi}{du_m} + \left(1 + \frac{A_k}{u_m}\right)\psi = 2 \left[ \frac{u_k}{u_m} \frac{d\phi}{du_k} \frac{d\Psi}{du_m} - \phi\Psi \right] \equiv S(u_m), \quad (\text{B.40})$$

where  $A_k = k^2/(2maH)$ , a dimensionless constant, and  $S$  is the driving source. We note



that  $u_k^2 = 4A_k u_m / 3$ . Equation (B.40) has following solution,

$$\psi = C_r^\psi \psi_r(u_m) + C_s^\psi \psi_s(u_m) + \psi_p(u_m). \quad (\text{B.41})$$

Here  $C_r^\psi$  and  $C_s^\psi$  are constants,  $\psi_r$  and  $\psi_s$  are the homogeneous solutions of Eq. (B.40) with the following forms,

$$\psi_r(u_m) = e^{-iu_m} M\left(\frac{3}{4} + \frac{A_k}{2}i, \frac{3}{2}, i2u_m\right), \quad (\text{B.42})$$

$$\psi_s(u_m) = e^{-iu_m} \frac{M\left(\frac{1}{4} + \frac{A_k}{2}i, \frac{1}{2}, i2u_m\right)}{\sqrt{u_m}}, \quad (\text{B.43})$$

where  $M$  is the Kummer's function, and

$$\psi_p(u_m) = \int_0^{u_m} \frac{\psi_r(x)\psi_s(u_m) - \psi_r(u_m)\psi_s(x)}{W(\psi_r, \psi_s)(x)} S(x) dx, \quad (\text{B.44})$$

the particular integral of Eq.(B.40) with initial conditions  $\psi_p(0) = d\psi_p/du_m(0) = 0$ . Here  $W(\psi_r, \psi_s)(u_m) = \psi_r d\psi_s/du_m - \psi_s d\psi_r/du_m = -u_m^{-3/2}/2$ , the Wronskian of  $\psi_r$  and  $\psi_s$ .

Again, the constants,  $C_r^\psi$  and  $C_s^\psi$ , can be determined by the adiabatic condition for the super-horizon mode. Particularly, these two constants must be zero if only regular mode of metric perturbation is considered. Therefore  $\psi = \psi_p$ , representing the adiabatic perturbation.

Once the perturbed field's solution is obtained, the gauge covariant energy density perturbation follows from Eq. (8.9), and becomes

$$\Delta_\psi = \frac{\frac{d\Psi}{du_m} \frac{d\psi_p}{du_m} + \Psi \psi_p - \left(\frac{d\Psi}{du_m}\right)^2 \phi + \frac{3}{2} \frac{d\Psi}{du_m} \psi_p}{\frac{1}{2} \left[ \left(\frac{d\Psi}{du_m}\right)^2 + \Psi^2 \right]}. \quad (\text{B.45})$$

In the following, the asymptotic behavior of the gauge covariant dark matter energy density perturbation is to be derived. The CDM model is considered first. From Eq.



(B.39), it is straightforward to find

$$\Delta_C = -9\phi_0 \begin{cases} \frac{u_k^2}{8} + O(u_k^4), & \text{if } u_k \ll 1 \\ \ln(u_k) + O(1), & \text{if } u_k \gg 1. \end{cases} \quad (\text{B.46})$$

For  $\psi$ DM model, it is more complicated and has four different phases as discussed in Chapter 9.1, which are to be verified from Eqs. (B.41) to (B.44). In the following presentation, we will organize the four phases in the chronological order. The phases before mass oscillation (phase (ii) in Chapter 9.1) are dealt with first and then we will show the results of the phases after mass oscillation (phase (i)).

#### (A) Before mass oscillation and super-horizon mode (phase (iia))

This phase can be dealt with using Eq. (B.44) directly. The background field  $\Psi$  has the following asymptotic form  $\Psi = \Psi_0[1 - u_m^2/5 + O(u_m^4)]$ , and the metric perturbation  $\phi$  can be expressed  $\phi = \phi_0[1 - u_k^2/10 + O(u_k^4)] = \phi_0[1 - 2A_k u_m/15 + O(u_m^2)]$ . To find the asymptotic form of the particular solution  $\psi_p$ , we first have,

$$\psi_r(u_m) = 1 - \frac{2}{3}A_k u_m + O(u_m^2), \quad (\text{B.47})$$

$$\psi_s(u_m) = \frac{1 - 2A_k u_m + O(u_m^2)}{\sqrt{u_m}}. \quad (\text{B.48})$$

Combining with above relations, it follows that  $\psi_p$  becomes

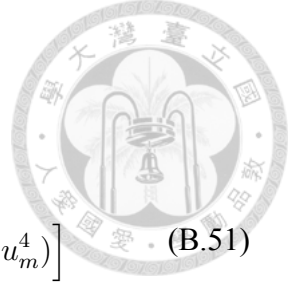
$$\psi_p(u_m) = \Psi_0 \phi_0 \left[ -\frac{2}{5}u_m^2 + \frac{44}{525}A_k u_m^3 + O(u_m^4) \right]. \quad (\text{B.49})$$

Finally, the denominator of Eq. (B.45) is

$$\frac{1}{2} \left[ \left( \frac{d\Psi}{du_m} \right)^2 + \Psi^2 \right] = \Psi_0^2 \left[ \frac{1}{2} + O(u_m^2) \right], \quad (\text{B.50})$$

and the numerator

$$\begin{aligned}
& \frac{d\Psi}{du_m} \frac{d\psi_p}{du_m} + \Psi \psi_p - \left( \frac{d\Psi}{du_m} \right)^2 \phi + \frac{3}{2} \frac{\frac{d\Psi}{du_m} \psi_p}{u_m} \\
&= \Psi_0^2 \phi_0 \left[ \left( \frac{8}{25} - \frac{2}{5} - \frac{4}{25} + \frac{6}{25} \right) u_m^2 - \frac{8}{175} A_k u_m^3 + O(u_m^4) \right] \\
&= \Psi_0^2 \phi_0 \left[ -\frac{8}{175} A_k u_m^3 + O(u_m^4) \right],
\end{aligned} \tag{B.51}$$



where the leading order terms cancel. We thus have

$$\Delta_\psi = \phi_0 \left[ -\frac{16}{175} A_k u_m^3 + O(u_m^4) \right] = \phi_0 \left[ -\frac{12}{175} u_k^2 u_m^2 + O(u_m^4) \right]. \tag{B.52}$$

The gauge covariant  $\psi$ DM energy density perturbation  $\propto u_k^2 u_m^2 \propto a^6$  when both  $u_k$  and  $u_m \ll 1$ .

### (B) Before mass oscillation and sub-horizon mode (phase (iib))

This phase is equivalent to  $u_m \ll 1$  and  $u_k \gg 1$ , which imply  $A_k \gg 1$ . Unlike the previous case,  $u_k$  is the natural variable here instead of  $u_m$ . The variables  $\psi_r$ ,  $\psi_s$  and the driving source  $S$  will be expressed as functions of  $u_k$ .

From the definition of Kummer's function  $M$ , the homogeneous solutions  $\psi_r$  and  $\psi_s$  are

$$\psi_r = \frac{\sin(\sqrt{3}u_k)}{\sqrt{3}u_k} + O(A_k^{-1}), \tag{B.53}$$

$$\psi_s = 2\sqrt{A_k} \left[ \frac{\cos(\sqrt{3}u_k)}{\sqrt{3}u_k} + O(A_k^{-1}) \right]. \tag{B.54}$$

On the other hand, the background field  $\Psi$  has the asymptotic form  $\Psi = \Psi_0 [1 - 9A_k^{-2}u_k^4/80 + O(A_k^{-4})]$ . Hence, the driving source  $S$  becomes

$$S = -\Psi_0 \phi_0 \frac{6}{5} \left[ 2 \frac{\sin(u_k)}{u_k} + \frac{\cos(u_k)}{u_k^2} - \frac{\cos(u_k)}{u_k^3} + O(A_k^{-2}) \right]. \tag{B.55}$$

Substituting Eqs. (B.53), (B.54) and (B.55) into Eq.(B.44) and changing the variable from  $u_m$  to  $u_k$ , the particular solution  $\psi_p$  becomes

$$\psi_p = -\frac{27}{10} \Psi_0 \phi_0 A_k^{-2} [u_k \sin(u_k) + O(1) + O(A_k^{-1})]. \tag{B.56}$$

Therefore, the gauge covariant energy density perturbation  $\Delta_\psi$  is

$$\Delta_\psi = \phi_0 \frac{81}{50} A_k^{-2} [u_k^2 \cos(u_k) + O(u_k) + O(A_k^{-1})]. \quad (\text{B.57})$$



The gauge covariant energy density perturbation grows as  $u_k^2 \propto a^2$  modulating the oscillation of radiation perturbation.

### (C) After mass oscillation and super-horizon mode (phase (ia))

In this phase, rather than dealing with Eq. (B.44) directly we adopt an alternative approach to find the asymptotic solution. This is because the Green's function integral of Eq. (B.44) is quite cumbersome after mass oscillation. Before proceeding, the background fields  $\Psi_r$  and  $\Psi_s$  in Eqs. (B.24) and (B.25) are redefined by dividing a factor  $2^{1/4}\Gamma(5/4)$ , i.e.,  $\Psi_r = J_{1/4}(u_m)/u_m^{1/4}$  and  $\Psi_s = Y_{1/4}(u_m)/u_m^{1/4}$ , to avoid irrelevant numerical factors appearing in the derivation. With this definition, the particular integral  $\psi_p$  will also be divided by the same factor. This change does not affect the values of either  $\delta_\psi$  or  $\Delta_\psi$ .

First,  $\psi_p$  can be expanded as follows,

$$\psi_p(u_m, A_k) = \sum_{n=0}^{\infty} \psi_p^{(n)}(u_m) A_k^n, \quad (\text{B.58})$$

for small  $A_k$ . Similarly, the same expansion applies to the driving source  $S$ ,

$$S(u_m, A_k) = \sum_{n=0}^{\infty} S^{(n)}(u_m) A_k^n, \quad (\text{B.59})$$

The metric perturbation  $\phi(u_k)$  inside  $S(u_m, A_k)$  can also be expanded as

$$\phi(u_k) = 3\phi_0 \sum_{n=0}^{\infty} \frac{(-1)^n}{(2n+1)!(2n+3)} u_k^{2n} = 3\phi_0 \sum_{n=0}^{\infty} \frac{(-\frac{3}{4}u_m)^n}{(2n+1)!(2n+3)} A_k^n. \quad (\text{B.60})$$

Substituting above relations into the perturbed field equation, it follows that,

$$\frac{d^2\psi_p^{(n)}}{du_m^2} + \frac{3}{2u_m} \frac{d\psi_p^{(n)}}{du_m} + \psi_p^{(n)} = \tilde{S}^{(n)}, \quad n = 0, 1, 2, 3, \dots \quad (\text{B.61})$$

where  $\tilde{S}^{(n)} = S^{(n)} - \psi_p^{(n-1)}/u_m$  with  $\psi_p^{(-1)}(u_m) = 0$  and  $\psi_p^{(n)}(0) = d\psi_p^{(n)}/du_m(0) = 0$  for any  $n = 0, 1, 2, 3, \dots$ . It turns out that  $\psi_p^{(n)}$  satisfies

$$\psi_p^{(n)}(u_m) = \int_0^{u_m} \frac{\Psi_s(u_m)\Psi_r(x) - \Psi_r(u_m)\Psi_s(x)}{W(\Psi_r, \Psi_s)(x)} \tilde{S}^{(n)}(x) dx, \quad (\text{B.62})$$

with  $W(\Psi_r, \Psi_s)(u_m) = 2u_m^{-3/2}/\pi$ , which resembles Eq. (B.44) since  $\psi \rightarrow \Psi$  as  $k \rightarrow 0$  or  $A_k \rightarrow 0$ .

Now,  $\tilde{S}^{(0)}(u_m) = -2\phi_0\Psi(u_m)$ . Substituting it into Eq. (B.62), one obtains the two integrals in Eq. (B.62) for  $n = 0$ ,

$$\int_0^{u_m} \frac{x^{\frac{3}{2}}\Psi_s(x)\tilde{S}^{(0)}(x)}{\Psi_0\phi_0} dx = \frac{1 - {}_1F_2\left(-\frac{1}{2}; -\frac{1}{4}, \frac{1}{4}; -u_m^2\right)}{4} + \int_0^{u_m} \frac{x^{\frac{3}{2}}\Psi_r(x)\tilde{S}^{(0)}(x)}{\Psi_0\phi_0} dx, \quad (\text{B.63})$$

and

$$\int_0^{u_m} \frac{x^{\frac{3}{2}}\Psi_r(x)\tilde{S}^{(0)}(x)}{\Psi_0\phi_0} dx = -\frac{\pi}{4}u_m \left[ 2u_m J_{-\frac{3}{4}}^2(u_m) - J_{-\frac{3}{4}}(u_m)J_{\frac{1}{4}}(u_m) + 2u_m J_{\frac{1}{4}}^2(u_m) \right], \quad (\text{B.64})$$

where  ${}_1F_2$  is the generalized hypergeometric function. Due to the fact  $u_m \gg 1$  in this phase, we can have the following asymptotic forms,

$$J_{\frac{1}{4}}(u_m) = \sqrt{\frac{2}{\pi u_m}} \left[ \cos \Theta + \frac{3}{32} \frac{\sin \Theta}{u_m} + O(u_m^{-2}) \right], \quad u_m \gg 1, \quad (\text{B.65})$$

$$Y_{\frac{1}{4}}(u_m) = \sqrt{\frac{2}{\pi u_m}} \left[ \sin \Theta - \frac{3}{32} \frac{\cos \Theta}{u_m} + O(u_m^{-2}) \right], \quad u_m \gg 1, \quad (\text{B.66})$$

$$J_{-\frac{3}{4}}(u_m) = \sqrt{\frac{2}{\pi u_m}} \left[ -\sin \Theta - \frac{5}{32} \frac{\cos \Theta}{u_m} + O(u_m^{-2}) \right], \quad u_m \gg 1, \quad (\text{B.67})$$

$${}_1F_2\left(-\frac{1}{2}; -\frac{1}{4}, \frac{1}{4}; -u_m^2\right) = -4u_m + 2\sqrt{2} \cos(2u_m) + O(u_m^{-1}), \quad u_m \gg 1, \quad (\text{B.68})$$

with  $\Theta = u_m - 3\pi/8$ . After straightforward substitution,  $\psi_p^{(0)}$  becomes

$$\sqrt{\frac{\pi}{2}} \frac{u_m^{\frac{3}{4}} \psi_p^{(0)}}{\Psi_0 \phi_0} = - \left[ u_m \sin \Theta + \frac{21}{32} \cos \Theta + O(u_m^{-1}) \right], \quad u_m \gg 1. \quad (\text{B.69})$$

It is difficult to get an analytic form for  $\psi_p^{(n)}$  with  $n = 1, 2, 3, \dots$ . However, we can take advantage of  $u_m \gg 1$ , and separate the integral  $\int_0^{u_m} = \int_0^{u_m^0} + \int_{u_m^0}^{u_m}$  where  $u_m^0$  is a constant  $\gg 1$ . Decompose  $\psi_p^{(n)}$  as follows:

$$\begin{aligned}\psi_p^{(n)} = & \frac{\pi}{2} \left[ \Psi_s \int_0^{u_m^0} x^{\frac{3}{2}} \Psi_r(x) \tilde{S}^{(n)}(x) dx - \Psi_r \int_0^{u_m^0} x^{\frac{3}{2}} \Psi_s(x) \tilde{S}^{(n)}(x) dx + \right. \\ & \left. \Psi_s \int_{u_m^0}^{u_m} x^{\frac{3}{2}} \Psi_r(x) \tilde{S}^{(n)}(x) dx - \Psi_r \int_{u_m^0}^{u_m} x^{\frac{3}{2}} \Psi_s(x) \tilde{S}^{(n)}(x) dx \right].\end{aligned}\quad (\text{B.70})$$

The first two integrals give constants of order  $O((u_m^0)^n)$ , but the last two integrals are at least order of  $O(u_m^n) \gg O((u_m^0)^n)$ . Now, the last two integrations can be carried out via the above approximate formula (Eqs. (B.60), (B.65), (B.66) and (B.69)). The leading order forms of  $\psi_p^{(n)}$  in the expansion of  $u_m^{-1}$  can be obtained as follows:

$$\begin{aligned}(-1)^{n+1} u_k^{-2n} \sqrt{\frac{\pi}{2}} \frac{u_m^{\frac{3}{4}}}{\Psi_0 \phi_0} \frac{\psi_p^{(n)} A_k^n}{3} = & \\ \left\{ \frac{2u_m \sin \Theta}{(2n+3)!} - \frac{3}{2} \left[ \frac{1}{8(2n+3)!} + \frac{1}{(2n+1)!(2n+3)} + \frac{1}{2n(2n+1)!} \right] \cos \Theta + \right. & \quad (\text{B.71}) \\ \left. O\left(\frac{1}{u_m}\right) \right\}, \quad u_m \gg 1.\end{aligned}$$

Substituting Eqs. (B.69) and (B.71) into Eq. (B.58) and summing up all order  $A_k$ , we



arrive at

$$\begin{aligned}
\frac{\psi_p}{\Psi_0} &= \phi_0 \sqrt{\frac{2}{\pi}} u_m^{-\frac{3}{4}} \left\{ 6 \left( \frac{\sin(u_k)}{u_k^3} - \frac{1}{u_k^2} \right) u_m \sin \Theta - \cos \Theta \times \right. \\
&\quad \left. \frac{9}{2} \left[ \frac{\sin(u_k)}{u_k} + \frac{8 \cos(u_k) - 1}{8u_k^2} - \frac{7 \sin(u_k)}{8u_k^3} - Ci(u_k) + \ln(u_k) + \gamma - \frac{1}{2} \right] + O\left(\frac{\sum_{l=0}^{\infty} a_l u_k^{2l}}{u_m}\right) \right\} \\
&= \phi_0 \left\{ \left[ 6 \left( \frac{\sin(u_k)}{u_k^3} - \frac{1}{u_k^2} \right) u_m + O\left(\frac{\sum_{l=0}^{\infty} b_l u_k^{2l}}{u_m}\right) \right] \Psi_s - \right. \\
&\quad \left. \frac{9}{2} \left[ \frac{\sin(u_k)}{u_k} + \frac{\cos(u_k)}{u_k^2} - \frac{\sin(u_k)}{u_k^3} - Ci(u_k) + \ln(u_k) + \gamma - \frac{1}{2} + O\left(\frac{\sum_{l=0}^{\infty} c_l u_k^{2l}}{u_m}\right) \right] \Psi_r \right\} \\
&= \phi_0 \left[ 6 \left( \frac{\sin(u_k)}{u_k^3} - \frac{1}{u_k^2} \right) u_m + O\left(\frac{\sum_{l=0}^{\infty} b_l u_k^{2l}}{u_m}\right) \right] \Psi_s + \frac{1}{2} \left[ \Delta_C + \phi_0 [9 \left( \frac{\sin(u_k)}{u_k^3} - \frac{1}{u_k^2} \right) + \right. \\
&\quad \left. O\left(\frac{\sum_{l=0}^{\infty} c_l u_k^{2l}}{u_m}\right)] \right] \Psi_r \equiv \Im[\hat{\psi}] \Psi_s + \Re[\hat{\psi}] \Psi_r, \tag{B.72}
\end{aligned}$$

where  $a_l$ ,  $b_l$  and  $c_l$  are constants which make the infinite summation in Eq. (B.72) converges for  $u_k \leq O(1)$ . Here, we identify the coefficient of  $\Psi_r$  to be  $\Re[\hat{\psi}]$  and that of  $\Psi_s$  to be  $\Im[\hat{\psi}]$  discussed in phase (ia) of the main text.

The energy density perturbation  $\delta_\psi$  can be express as

$$\begin{aligned}
\delta_\psi &= 2\Re[\hat{\psi}] - \frac{3\Im[\hat{\psi}]}{2u_m} + \frac{3\Im[\hat{\psi}]}{u_m} \sin^2 \left( u_m - \frac{3}{8}\pi \right) \\
&= \Delta_C + \frac{3\Im[\hat{\psi}]}{u_m} \sin^2 \left( u_m - \frac{3}{8}\pi \right) + O\left(\frac{\sum_{l=0}^{\infty} d_l u_k^{2l}}{u_m}\right) \phi_0. \tag{B.73}
\end{aligned}$$

Similarly, the coefficient  $d_l$  plays the same role with  $a_l$ ,  $b_l$  and  $c_l$ . From Eq. (B.39), one can verify  $\Delta_C \rightarrow 0$  as  $u_k \rightarrow 0$ . This is consistent with the adiabatic condition discussed in the main text.

Finally, the asymptotic form of the gauge covariant energy density perturbation  $\Delta_\psi$  is followed by adding the last term of the numerator in Eq. (B.45) to Eq. (B.73). This additional term exactly cancel the second term in Eq.(B.73) up to the leading order. Hence



the gauge covariant energy density perturbation becomes

$$\Delta_\psi = \Delta_C + O\left(\frac{\sum_{l=0}^{\infty} e_l u_k^{2l}}{u_m}\right) \phi_0, \quad u_m \gg 1. \quad (\text{B.74})$$

Again, the constant  $e_l$  makes the infinite summation in Eq. (B.74) converges when  $u_k \leq O(1)$ . It recovers the CDM result (Eq.(B.46)) to the leading term. The high order terms can be ignored as long as  $A_k \ll 1$  or  $u_k \leq O(1)$ . Since  $u_k \ll 1$  and  $u_m \gg 1$  in this phase, this implies  $A_k \ll 1$ . Hence, the leading term of Eq. (B.74) is a good approximation, and the gauge covariant energy density perturbation of  $\psi$ DM follows the CDM case and grows as  $u_k^2 \propto a^2$ .

#### (D) After mass oscillation and sub-horizon mode (phase (ib))

The order of  $A_k$  can be arbitrary in this phase and so high order terms in Eq. (B.74) cannot be ignored. We shall deal with Eq. (B.44) directly. Noted that

$$\begin{aligned} \lim_{u_m \rightarrow \infty} \int_0^{u_m} \frac{\psi_r(x)}{W(\psi_r, \psi_s)(x)} S(x) dx &= C_1(A_k), \\ \lim_{u_m \rightarrow \infty} \int_0^{u_m} \frac{\psi_s(x)}{W(\psi_r, \psi_s)(x)} S(x) dx &= C_2(A_k), \end{aligned} \quad (\text{B.75})$$

where  $C_1$  and  $C_2$  are constants depending only on  $A_k$ . This simplification is based on that the driving source  $S(u_m)$  diminishes as  $u_m \rightarrow \infty$ , and the integrals in Eq.(B.75) can be approximated by constants as long as  $u_k \geq O(1)$  and  $u_m \gg 1$ .

From the asymptotic relations for  $\psi_r$  and  $\psi_s$ ,

$$u_m^{\frac{3}{4}} \psi_r \propto \frac{e^{i \left( u_m - \frac{3}{8} \pi + \frac{A_k}{2} \ln(2u_m) \right)}}{\Gamma\left(\frac{3}{4} + \frac{A_k}{2} i\right)} + \frac{e^{-i \left( u_m - \frac{3}{8} \pi + \frac{A_k}{2} \ln(2u_m) \right)}}{\Gamma\left(\frac{3}{4} - \frac{A_k}{2} i\right)}, \quad u_m \gg 1, \quad (\text{B.76})$$

$$u_m^{\frac{3}{4}} \psi_s \propto \frac{e^{i \left( u_m - \frac{1}{8} \pi + \frac{A_k}{2} \ln(2u_m) \right)}}{\Gamma\left(\frac{1}{4} + \frac{A_k}{2} i\right)} + \frac{e^{-i \left( u_m - \frac{1}{8} \pi + \frac{A_k}{2} \ln(2u_m) \right)}}{\Gamma\left(\frac{1}{4} - \frac{A_k}{2} i\right)}, \quad u_m \gg 1, \quad (\text{B.77})$$

one can obtain  $\psi_p$  from Eq. (B.44) in terms of the above expressions of  $\psi_r$  and  $\psi_s$  as well as  $C_1(A_k)$  and  $C_2(A_k)$ . A straightforward calculation from Eq. (B.45) shows that the

gauge covariant energy density perturbation can be expressed as

$$\Delta_\psi \simeq B_r(A_k) \cos(A_k \ln(u_k)) + B_s(A_k) \sin(A_k \ln(u_k)), u_m \gg 1, u_k \geq O(1), \quad (\text{B.78})$$



where the mass oscillation of  $\psi_p$  is eliminated by that of  $\Psi_r$  and it is left with only the matter-wave oscillation. Here  $B_r(A_k)$  and  $B_s(A_k)$  are the linear combination of  $C_1(A_k)$  and  $C_2(A_k)$ . The gauge-covariant energy density oscillates with a constant frequency  $A_k$  in  $\ln(u_k)$  space.

Note that Equation (B.78) is valid for any  $A_k$ . One can identify constants  $B_r$  and  $B_s$  in the long-wave limit, i.e.,  $A_k \ll 1$ , where Eq. (B.78) can be approximated as  $\Delta_\psi \sim B_r(A_k) + B_s(A_k)A_k \ln(u_k)$ . The coefficients  $B_r(A_k)$  and  $B_s(A_k)$  can be fixed by solution matching, which demands that Eq. (B.78) with  $u_k \rightarrow 1$  from above should match Eq. (B.74) with  $u_k \rightarrow 1$  from below. Comparing these two equations, one can find

$$B_r(A_k) \rightarrow -9\phi_0 \left( \gamma - \frac{1}{2} \right), B_s(A_k) \rightarrow -9\phi_0/A_k. \quad (\text{B.79})$$

This expression agrees with the result of Phase (ib) in the main text.



# Appendix C

## Full Treatment Evolution

Governing equations are presented here with considerations of neutrino decoupling and photon-baryon coupling. For the zeroth order equations, the Friedmann equations with all relevant species are

$$H^2 = \frac{8\pi G}{3}a^2(\epsilon_{ph} + \epsilon_\nu + \epsilon_b + \epsilon_D), \quad (\text{C.1})$$

$$H' - H^2 = -4\pi Ga^2[(\epsilon_{ph} + P_{ph}) + (\epsilon_\nu + P_\nu) + (\epsilon_b + P_b) + (\epsilon_D + P_D)]. \quad (\text{C.2})$$

In addition, all species obey their own conservation laws (Eq. (B.7)).

To enclose above equations, the equation of state is specified for the neutrino and baryon. Since neutrinos are relativistic particles, the equation of state is the same with photons, i.e.,  $P_\nu = \epsilon_\nu/3$ . Baryons are non-relativistic and described by a pressureless fluid, i.e.,  $P_b = 0$ .

First-order perturbed Einstein equations have the same structures as Friedmann equations, i.e.,

$$-k^2\phi - 3H(\phi' + H\phi) = 4\pi Ga^2(\delta\epsilon_{ph} + \delta\epsilon_\nu + \delta\epsilon_b + \delta\epsilon_D), \quad (\text{C.3})$$

$$\phi' + H\phi = -4\pi Ga^2[(\epsilon_{ph} + P_{ph})\theta_{ph} + (\epsilon_\nu + P_\nu)\theta_\nu + (\epsilon_b + P_b)\theta_b + (\epsilon_D + P_D)\theta_D]. \quad (\text{C.4})$$

We need the continuity (density) equation and Euler (momentum) equation for every species to close perturbed equations. For  $\psi$ DM, it obeys Eqs. (B.14) and (B.15). On the other hand, neutrinos have decoupled from other species and become collisionless

particles very early in the radiation-dominant era. Free-streaming damping will make its energy density perturbation diminished abruptly(Ma and Bertschinger, 1995) upon the mode entering horizon. However, before entering horizon, neutrino perturbations have the same behavior as photon perturbations under the adiabatic condition. Hence the energy density and velocity potential perturbations of neutrinos can be approximated as,

$$\delta_\nu = \begin{cases} \delta_{ph}, & \tau \leq \tau_1, \\ 0, & \tau > \tau_1, \end{cases} \quad (C.5)$$

$$\theta_\nu = \begin{cases} \theta_{ph}, & \tau \leq \tau_1, \\ 0, & \tau > \tau_1, \end{cases} \quad (C.6)$$

where  $\tau_1$  is the conformal time of the first oscillation null of  $\Delta_{ph}(= \delta_{ph} - 4H\theta_{ph})$  and is  $k$ -dependent(Ma and Bertschinger, 1995).

The photon and baryon density and momentum equations read:

$$\delta'_{ph} = \frac{4}{3}k^2\theta_{ph} + 4\phi', \quad (C.7)$$

$$\theta'_{ph} = -\frac{1}{4}\delta_{ph} - \alpha Q - \phi, \quad (C.8)$$

$$\delta'_b = k^2\theta_b + 3\phi', \quad (C.9)$$

$$\theta'_b + H\theta_b = \beta Q - \phi, \quad (C.10)$$

where the subscripts "ph" and "b" stand for photon and baryon respectively,  $Q \equiv \theta_{ph} - \theta_b$ ,  $\beta = (4\epsilon_{ph}/3\epsilon_b)\alpha$  and  $\alpha = l_T^{-1}$  with  $l_T$  being the Thomson scattering mean free path. The last quantity is defined to be  $l_T^{-1} \equiv an_e\sigma_T$ , where  $n_e$  is the electron number density and  $\sigma_T$  the Thomson cross-section. The photon and baryon fluids are coupled through the relative velocity potential  $Q$  via Thomson scattering.

Note that  $l_T^{-1}$  decreases with time as  $a^{-2}$  for fully ionized baryons, and at some point  $l_T^{-1}$  can be smaller than  $k$ . After then, photons can no longer be described by a fluid and the above photon fluid equations fail to hold. Hence, for the analysis below to be valid

we must demand  $kl_T \ll 1$ . Moreover, we shall be focusing on modes that have already entered horizon,  $k/H \gg 1$ . It turns out that  $k_c$  of  $m = 10^{-22}$  eV satisfies the first criteria throughout the radiation dominant era and satisfies the second in the late epoch of the radiation era.

In the sub-horizon regime, the photon momentum equation is dominated by the photon pressure and the coupling term, and hence the gravity can be ignored. This situation is similar to the short wave limit of the self-gravitating non-relativistic fluid where perturbations do not feel the gravity and become sound waves. We therefore drop  $\phi$  in Eqs. (C.7), (C.8), (C.9) and (C.10).

Subtracting Eq. (C.8) from Eq. (C.10), we can derive an equation for  $Q$ :

$$Q' = -\frac{1}{4}\delta_{ph} + H\theta_{ph} - (\alpha + \beta + H)Q. \quad (\text{C.11})$$

Substituting  $(1/4)\delta_{ph}$  from Eq. (C.11) into Eq. (C.8) and solving for  $\theta_{ph}$  and  $\theta'_{ph}$ , we arrive at

$$\theta_{ph} = \frac{3}{k^2 - 3H' + 3H^2} \left[ H[Q' + (\beta + H)Q] - [Q' + (\alpha + \beta + H)Q]' \right], \quad (\text{C.12})$$

$$\theta'_{ph} = \frac{k^2 - 3H'}{k^2 - 3H' + 3H^2} \left[ Q' + (\beta + H)Q + \frac{3H}{k^2 - 3H'} [Q' + (\alpha + \beta + H)Q]' \right]. \quad (\text{C.13})$$

Now, since we are in the regime  $k \gg H$ , any term of order  $O(H^2/k^2)$  or  $O(H'/k^2)$  can be ignored. However, we need to keep terms of order  $O(H/k)$  as will become clear later. The reason for the coupling terms, such as  $\alpha Q$  or  $\beta Q$ , to be finite leading-order terms is that we have large  $\alpha$  and  $\beta$  despite having a small relative velocity potential  $Q$ . Therefore,  $Q'$  is small compared to  $\alpha Q$  or  $\beta Q$ , as  $Q' = O((k/\sqrt{3})Q)$  due to the photon oscillation to be shown below and furthermore  $kl_T \ll 1$ .

After the above considerations, we find

$$\theta_{ph} = -\frac{3}{k^2} [[Q' + (\alpha + \beta)Q]' - \{H\beta Q\}], \quad (\text{C.14})$$

$$\theta'_{ph} = \frac{\beta}{\alpha + \beta} [Q' + (\alpha + \beta)Q] + \left\{ \frac{3H}{k^2} [(\alpha + \beta)Q]' + \frac{\alpha}{\alpha + \beta} Q' \right\}. \quad (C.15)$$

Terms in the brace brackets are terms of order  $O(H/k)$ . If we ignore those high-order terms in Eqs. (C.14) and (C.15), it follows

$$[Q' + (\alpha + \beta)Q]'' + \frac{k^2}{3} \frac{\beta}{\alpha + \beta} [Q' + (\alpha + \beta)Q] = 0. \quad (C.16)$$

The quantity  $Q' + (\alpha + \beta)Q$  oscillates with the photon sound frequency modified by the presence of baryons, and this quantity is nothing more than  $-(1/4)\Delta_{ph}$  from Eq. (C.11), where  $\Delta_{ph}$  is the covariant energy density perturbation of photon. Thus the leading order terms give rise to a fast photon sound oscillation, and so the slow evolution of drag damping entails the next order correction to Eq. (C.16), which all involve  $Q'$ . To the leading order,  $Q' = ik(\beta/(3(\alpha + \beta)))^{1/2}Q$ .

The approach by which we will derive the next order equation is similar to Phase (i) of Section 9.1, where we let  $Q' + (\alpha + \beta)Q = A(\tau) \exp[ik \int (\beta/(3(\alpha + \beta))) d\tau]$  and  $A(\tau)$  is a slowly varying function of  $\tau$ . Substituting this expression into Eqs. (C.14) and (C.15), we find that

$$\frac{dA}{d\eta} = -\frac{\alpha}{2(\alpha + \beta)} \left[ \frac{k^2}{3H(\alpha + \beta)} + \frac{1}{2} \right] A, \quad (C.17)$$

where  $\eta \equiv \ln a$ . This equation has an analytical solution.

It is clear from that Eq. (C.17) that for very long waves,  $k^2 \rightarrow 0$ , the amplitude  $A$  of  $\Delta_{ph}$  will decrease when  $\alpha/\beta (= (3/4)\epsilon_b/\epsilon_{ph})$  becomes non-negligible occurring shortly after radiation-matter equality. On the other hand for shorter waves where  $k^2 > H(\alpha + \beta)$ , the amplitude  $A$  will further decrease and occur earlier in time. We find that  $k_c^2/H\beta \sim 1$  shortly before the radiation-matter equality and the drag damping begins to take effect for the critical mode near the end of radiation-dominant era.

Figure (C.1) shows the evolution of  $\Delta_{ph}$  for  $k = k_c$  and  $k = 0.1k_c$ , where both solutions of Eq. (C.17) and of the full treatment are given. Good agreement is found. Baryon density perturbations can also be calculated from Eqs. (C.9) and (C.14) with an understanding that  $\Delta_b = \delta_b$  and  $\theta_{ph} = \theta_b$  to the leading order. It yields  $\Delta_b = (3/4)\Delta_{ph}$ . We also plot baryons solutions of the above approximate treatment and the full treatment. Again,

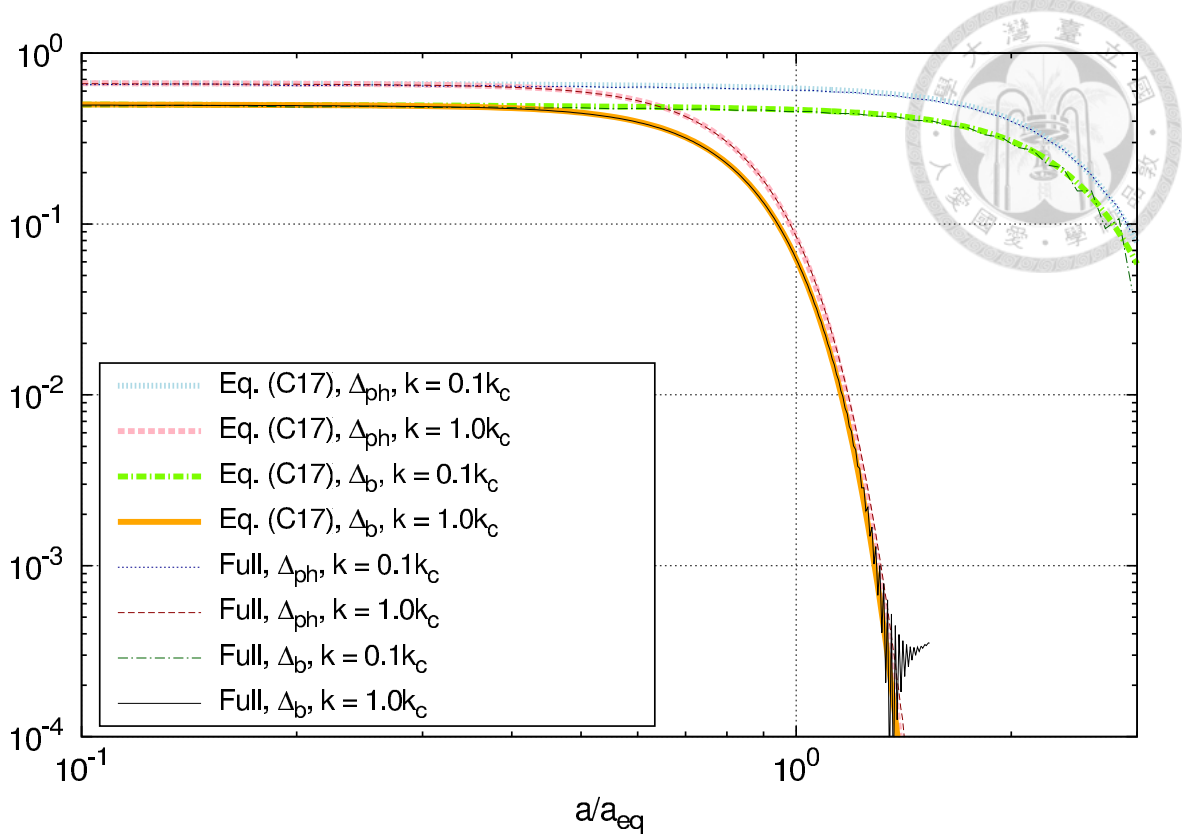


Figure C.1: The envelopes of gauge covariant photon and baryon energy density perturbations solved by Eq. (C.17) (thick line) and full treatment equations (thin line) for two distinct wavenumbers. Solutions of Eq. (C.17) well agrees with those of the full treatment. Noted that damping for short wavelength modes is controlled by  $(\epsilon_b/\epsilon_{ph})k^2l_T/H$ , while damping for long wave modes is  $k$ -independent.

good agreement is found, till after radiation-matter equality, as afterwards the gravity of matter can no longer be ignored.



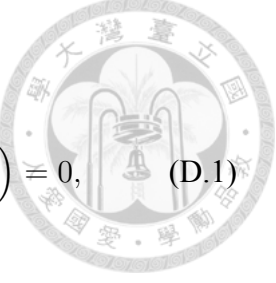


## Appendix D

# Particle Mass Dependence

In Section 10.2 we consider how solutions change with a changing  $a_m$  for a fixed particle mass  $m$ , and concluded that when  $a_m$  becomes large, the effect is equivalent to make  $k$  appear smaller. When the particle mass  $m$  is allowed to change, Eq. (10.10) is invariant to a transformation, which we call the mass-tempo-size transformation. We normalize time  $t$  to  $t_m$ , and note that  $\alpha \propto m^2(a_m/a)^3$ . It is straightforward to show that the solution is invariant, up to a shift in  $\ln(a)$  space, to the changing  $a_m$ ,  $k$  and  $m$  so long as  $ka_m$  and  $ma_m^2$  are kept fixed. This transformation for a changing  $a_m$  is in fact a transformation only of the particle mass  $m$ . We note that  $\ln(a_m) = \ln(a_{m0}) + \ln K(\delta\theta_0)$  for a  $K(\delta\theta_0)$  given in Eq. (10.16); the quantity  $\ln(a_{m0})$  depends only on the particle mass  $m$  and another quantity  $K(\delta\theta_0)$  on how nonlinear the background field is, and hence the particle mass and the nonlinearity appear to be able to vary independently. However, the transformation requires a fixed  $ma_m^2$ , which becomes  $ma_{m0}^2K^2(\delta\theta_0) = (aH)K^2(\delta\theta_0)$  where  $aH$  is independent of the particle mass  $m$ , the scaling factor  $a$  and the nonlinearity. As a result, a fixed  $ma_m^2$  implies fixed nonlinearity  $K(\delta\theta_0)$  in the transformation, and therefore this transformation involves only a varying particle mass  $m$ .

Realizing it, the  $m$  dependence of the spectral peak  $k_{peak}$  can be straightforwardly obtained. This can be carried out since an analytical solution of the perturbed field can be found to a good approximation. From Eq. (10.10), we find that the sub-horizon normalized



fluid density  $\delta n/n$  satisfies

$$\frac{d^2}{d\eta^2} \left( \frac{\delta n}{n} \right) + \left( \frac{k}{k_c} \right)^4 \left[ 1 - \left( \frac{k_c}{k} \right)^2 \frac{\theta_0^2}{4} \left( \frac{a_m}{a_{m0}} \right)^2 \exp(-\eta) \right] \left( \frac{\delta n}{n} \right) = 0, \quad (\text{D.1})$$

where  $\eta \equiv \ln(a/a_m)$  and  $\delta n/n = 2\Re[\hat{q}] \approx \Delta_\theta$ .

As a check of the accuracy of this fluid equation to Eq.(10.8), we solve Eq. (D.1) numerically. The initial  $\eta_i$  starts from  $a_\kappa/a_{m0}$  with the initial slope  $S(\eta_i) \equiv (k/k_c)^2 [1 - (k_c/k)^2 (\theta_0^2/4)(a_m/a_{m0})^2 \exp[-\eta_i]]^{1/2}$ . Solutions are plotted in Fig. (10.2), and one can see that the solutions excellently agree with those of Mathieu's equation.

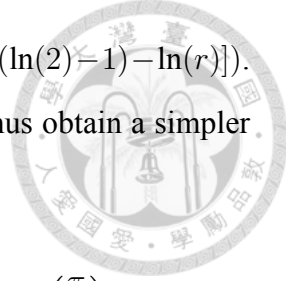
One may adopt the WKB approximation to analyze the solution, for which the phase,  $\int d\eta S(\eta)$ , has an analytical expression. When the integrand is imaginary, it represents a growing solution  $\exp(A(\eta_i) - A(\eta))$ , as  $A(\eta)$  is a decreasing function of  $\eta$ . When the integrand is real, it has an oscillating solution,  $\sin(B(\eta) + d_0)$ , where  $B(\eta) \geq 0$  and is an increasing function of  $\eta$ , and  $d_0$  is the phase. In between, the integrand crosses zero, the WKB approximation fails and we have an Airy function that connects solutions on the two sides, i.e.,  $\exp[A(\eta_i) - A(\eta)] \rightarrow 2 \sin(B(\eta) + \pi/4)$ . Here, the analytical expressions of  $A$  and  $B$  are

$$A(\eta) = 2 \frac{k^2}{k_c^2} \left\{ [r \exp(-\eta) - 1]^{\frac{1}{2}} - \tan^{-1}[(r \exp(-\eta) - 1)^{\frac{1}{2}}] \right\},$$

$$B(\eta) = 2 \frac{k^2}{k_c^2} \left\{ -[1 - r \exp(-\eta)]^{\frac{1}{2}} + \frac{1}{2} \ln \left[ \frac{1 + [1 - r \exp(-\eta)]^{\frac{1}{2}}}{1 - [1 - r \exp(-\eta)]^{\frac{1}{2}}} \right] \right\}, \quad (\text{D.2})$$

where  $r = (k_c/k)^2 (\pi^2/4)(a_m/a_{m0})^2$ , and both  $A(\eta)$  and  $B(\eta)$  equal zero when the integrand crosses zero. The expression of  $A(\eta)$  has been used in Section 10.2 to find the growth factor.

When  $\eta \gg 1$ , we recover that free-particle oscillation, i.e.,  $B \rightarrow (k^2/k_c^2)(\ln(a/a_m) + d)$  with a phase  $d$ . Note that the peak of the solution is located at the oscillating side of the solution. The relation between  $k_{peak}$  and  $m$  is just the solution of a transcendental equation  $B(\eta_{eq}) + \pi/4 = \pi/2$ , where the sine oscillation phase is equal to  $\pi/2$ , where  $\eta_{eq}$  is the value of  $\eta$  at radiation-matter equality. We make a further approximation to simplify the matter. The nonlinear contribution to  $B$  is negligible at the peak of the solution, i.e.,



$r \exp(-\eta) \ll 1$ , so that  $B(\eta) \approx (k/k_c)^2 (\ln(a/a_{m0}) + [\ln(a_{m0}/a_m) + 2(\ln(2) - 1) - \ln(r)])$ .

This approximation is better for a large  $m$  than for a small  $m$ . We thus obtain a simpler transcendental equation for  $k_{peak}$ :

$$\frac{\pi}{4} \left( \frac{k_c}{k_{peak}} \right)^2 + \ln \left[ \frac{\pi}{4} \left( \frac{k_c}{k_{peak}} \right)^2 \right] = \ln \left( \frac{a_{eq}}{a_{m0}} \right) - 3 \ln \left( \frac{a_m}{a_{m0}} \right) - 2 - \ln \left( \frac{\pi}{4} \right), \quad (\text{D.3})$$

which can be solved numerically rather easily. It can be easily seen that  $k_{peak}/k_c < 1$  for  $m = 10^{-22}$  eV, and more so for a larger particle mass because  $\ln(a_{eq}/a_{m0})$  gets larger. Aside from the mass dependence of  $k_c \propto m^{1/2}$ ,  $k_{peak}$  has another weak mass dependence on  $\ln(a_{m0}/a_{eq})$ , with  $a_{m0} \propto m^{-1/2}$ . Another term,  $\ln(a_m/a_{m0})$ , is a measure of  $\delta\theta_0$ , which is given in Eq. (10.16) and has no mass dependence.

Though  $k_{peak}$  is derived here from the passive evolution,  $k_{peak}$  of the full treatment deviates only slightly from this formula; thus, to a good approximation Eq. (D.3) provides an analytical expression for  $k_{peak}$  of the full treatment, and we find this expression is accurate within 10% of the peak of  $k^3 |\Delta_\theta(k)|^2$  of the full treatment. Moreover,  $k_{peak}$  is largely frozen after  $a = a_{eq}$  shown in Fig. (10.3), as  $k_{peak}$  is smaller than the Jeans wave number  $k_J$  in the matter-dominated regime, and therefore this spectral peak persists in the linear matter power spectrum throughout the later epoch.

The particle mass dependence of the quantity  $k_{peak}/k_c$  is mild, shown in the right-hand side of Eq. (D.3). When the particle mass  $m \rightarrow \infty$ , we have  $\ln(a_{eq}/a_{m0}) \rightarrow 0$ , the peak  $k_{peak}/k_c \rightarrow 0$ , and the growth factor of Eq. (10.12) approaches zero. The particle mass scaling of the growth factor can be calculated by determining  $k_{peak}$  and substituting into the growth factor Eq. (10.12). Comparing the growth factor for  $m = 10^{-22}$  eV to find the ratio, one is then able to determine the spectral peak height for any  $m$  by referring to the peak height of Fig. (10.3) for  $m = 10^{-22}$  eV, which can be approximated to be  $\ln |\Delta_\theta/\Delta_{cdm}|^2|_{peak} = 17(k_{peak}/k_c) - 10.2$  as a fit.





## Appendix E

# General Dispersion Relation

The perturbed field equation, Eq. (10.8), has ignored a restoring force proportional to  $\mathcal{H}^2$  compared to the original equation Eq. (10.5). This is a valid approximation for the extreme axion model because at the onset of the much delayed mass oscillation, the Hubble parameter is negligibly small. But for ordinary axions where the initial field angles are not on the top of the potential, this term must be kept. In fact by a straightforward extension of the analysis given in Section 10.2, we can obtain a general dispersion relation valid for the extreme axion as well as ordinary axions:

$$\omega = \mathcal{H} \frac{\sqrt{\frac{k^2}{a^2} + \frac{3}{4}\mathcal{H}^2}}{2\omega_\theta} \left[ \frac{k^2}{\mathcal{H}^2 a^2} + \frac{3}{4} - \frac{2\alpha}{\mathcal{H}^2} \right]^{\frac{1}{2}}. \quad (\text{E.1})$$

Here  $\alpha \sim m^2(\theta_0^2/8)(a_m/a)^3$ , and  $\mathcal{H}^2 = H^2 a^{-2} = (m/2)^2(a_{m0}/a)^4$ . Now, for both very large and very small  $a$ , we have a positive  $Q \equiv k^2/(\mathcal{H}a)^2 + (3/4) - 2\alpha/\mathcal{H}^2$  and thus a real  $\omega$ . Therefore,  $Q$  must have a minimum, and the minimum value of  $Q$  determines whether or not the instability window is open. The quantity  $Q$  is quadratic with respect to  $a$  and so it is straightforward to obtain the window of instability for which  $Q$  is negative.

The quantity  $Q$  is allowed to be negative, when

$$\frac{k}{k_c} < \frac{\theta_0^2}{\sqrt{12}} \left( \frac{a_m}{a_{m0}} \right)^3, \quad (\text{E.2})$$



and the unstable window is  $a_- < a < a_+$  with

$$\frac{a_\pm}{a_{m0}} = \frac{\theta_0^2 \left( \frac{a_m}{a_{m0}} \right)^3 \pm \sqrt{\theta_0^4 \left( \frac{a_m}{a_{m0}} \right)^6 - 12 \left( \frac{k}{k_c} \right)^2}}{8 \left( \frac{k}{k_c} \right)^2}. \quad (\text{E.3})$$

On the other hand, Eq. (10.8) is valid after the mass oscillation and the mode is subhorizon. This yields a constraint on  $a > a_\kappa$  where  $a_\kappa = \max\{a_k, a_m\}$  defined in Section 10.2, and the window of instability is narrowed down to  $\max\{a_-, a_\kappa\} < a < a_+$ . This window is non-empty if and only if  $a_\kappa < a_+$ . In the following, we will discuss the two possibilities,  $a_\kappa = a_k$  and  $a_\kappa = a_m$ .

### (i) Long waves $a_k > a_m$

Here  $a_\kappa = a_k$  and the fact that  $a_k > a_m$  gives  $k/k_c < a_{m0}/a_m$ . On the other hand, to open the unstable window, we must have  $a_k < a_+$  and that gives  $k/k_c < (4/19)\theta_0^2(a_m/a_{m0})^3$ , which also satisfies Eq. (E.2). Therefore the unstable window non-empty when

$$\frac{k}{k_c} < \min \left\{ \frac{a_{m0}}{a_m}, \frac{4\theta_0^2}{19} \left( \frac{a_m}{a_{m0}} \right)^3 \right\}. \quad (\text{E.4})$$

Equation (E.4) implies that long-wavelength modes always have this unstable window for a finite  $\theta_0$ . But for the free-particle axion where  $\theta_0 \rightarrow 0$ , the unstable  $k \rightarrow 0$  as well. However, the growth factor is proportional to  $k/k_c$  (c.f. Eq. (10.12) in Section 10.2), and hence the effect of growth is weak in the long-wavelength limit.

### (ii) Short waves $a_k < a_m$

This case has  $a_\kappa = a_m$  and the inequality of this regime yields  $k/k_c > a_{m0}/a_m$ . Furthermore the fact  $a_m < a_+$  gives

$$\frac{k}{k_c} < \frac{\sqrt{4\theta_0^2 \left( \frac{a_m}{a_{m0}} \right)^4 - 3}}{4 \frac{a_m}{a_{m0}}}. \quad (\text{E.5})$$



Both inequalities of  $k/k_c$  give

$$\frac{a_{m0}}{a_m} < \frac{k}{k_c} < \frac{\sqrt{4\theta_0^2 \left(\frac{a_m}{a_{m0}}\right)^4 - 3}}{4 \frac{a_m}{a_{m0}}}. \quad (\text{E.6})$$

Equation (E.6) provides a constraint on  $\theta_0$  to make the inequality non-empty, thus

$$\theta_0 > \frac{\sqrt{19}}{2} \left(\frac{a_{m0}}{a_m}\right)^2. \quad (\text{E.7})$$

Unlike case (i), there is a minimum value of  $\theta_0$  to open the unstable window for some wavenumber satisfying Eq. (E.6). This short-wave regime is relevant for the high- $k$  extension of the power spectrum. For example, when  $\theta_0 = \pi/2$ , we have  $a_m \approx a_{m0}$ , and the inequality, Eq. (E.7), cannot be satisfied. That is, high- $k$  modes are stable for  $\theta_0 = \pi/2$ , thus no high- $k$  extension in the power spectrum.





# Bibliography

M. Abramowitz and I. A. Stegun. *Handbook of Mathematical Functions*. Dover, New York, 1964.

P. A. R. Ade, N. Aghanim, M. Arnaud, M. Ashdown, J. Aumont, C. Baccigalupi, A. J. Banday, R. B. Barreiro, J. G. Bartlett, and et al. Planck 2015 results xiii. cosmological parameters. *Astron. Astrophys.*, 594:A13, 2016.

N. C. Amorisco, A. Agnello, and N. W. Evans. The core size of the fornax dwarf spheroidal. *Mon. Not. R. Astron. Soc.*, 429:L89–L93, 2013.

E. Armengaud, N. Palanque-Delabrouille, C. Yèche, D. J. Marsh, and J. Baur. Constraining the mass of light bosonic dark matter using sdss lyman- $\alpha$  forest. *arXiv:1702.02116*, 2017.

V. I. Arnold. Sur la topologie des écoulements stationnaires des fluides parfaits. *C. R. Acad. Sci. Paris*, 261:17–21, 1965.

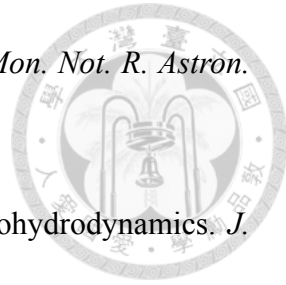
A. Arvanitaki, S. Dimopoulos, S. Dubovsky, N. Kaloper, and J. March-Russell. String axiverse. *Phys. Rev. D*, 81:123530, 2010.

S. A. Balbus. Enhanced angular momentum transport in accretion disks. *Annu. Rev. Astron. Astrophys.*, 41:555–597, 2003.

S. A. Balbus and J. F. Hawley. A powerful local shear instability in weakly magnetized disks. i- linear analysis. *Astrophys. J.*, 376:214–222, 1991.

D. Balsara, D. Ward-Thompson, and R. M. Crutcher. A turbulent mhd model for molecular

clouds and a new method of accretion on to star-forming cores. *Mon. Not. R. Astron. Soc.*, 327:715–720, 2001.



D. S. Balsara. Divergence-free adaptive mesh refinement for magnetohydrodynamics. *J. Comput. Phys.*, 174:614–648, 2001.

R. D. Blandford and D. G. Payne. Hydromagnetic flows from accretion discs and the production of radio jets. *Mon. Not. R. Astron. Soc.*, 199:883–903, 1982.

P. Bode, J. P. Ostriker, and N. Turok. Halo formation in warm dark matter models. *Astrophys. J.*, 556:93–107, 2001.

M. Boylan-Kolchin, J. S. Bullock, and M. Kaplinghat. Too big to fail? the puzzling darkness of massive milky way subhaloes. *Mon. Not. R. Astron. Soc.*, 415:L40–L44, 2011.

E. Calabrese and D. N. Spergel. Ultra-light dark matter in ultra-faint dwarf galaxies. *Mon. Not. R. Astron. Soc.*, 460:4397–4402, 2016.

S.-R. Chen, H.-Y. Schive, and T. TChiueh. Jeans analysis for dwarf spheroidal galaxies in wave dark matter. *Mon. Not. R. Astron. Soc.*, 468:1338–1348, 2017.

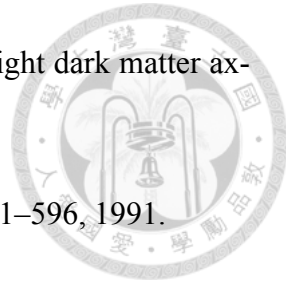
S. Childress. New solutions of the kinematic dynamo problem. *J. Math. Phys.*, 11:3063–3071, 1970.

T. Chiueh. Why is the dark axion mass  $10^{-22}$  ev? *arXiv:1409.0380*, 2014.

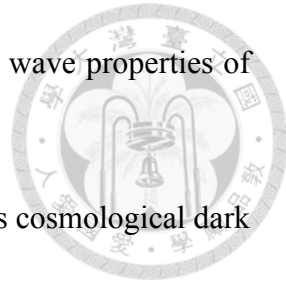
P. Colella. Multidimensional upwind methods for hyperbolic conservation laws. *J. Comput. Phys.*, 87:171–200, 1990.

R. Courant, K. Friedrichs, and H. Lewy. Über die partiellen differenzengleichungen der mathematischen physik. *Math. Ann.*, 100:32–74, 1928.

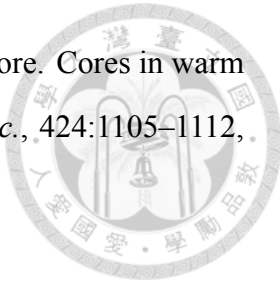
H. Davoudiasl and C. W. Murphy. Fuzzy dark matter from infrared confining dynamics. *Phys. Rev. Lett.*, 118:141801, 2017.



- A. Diez-Tejedor and D. J. Marsh. Cosmological production of ultralight dark matter axions. *arXiv:1702.02116*, 2017.
- S. A. E. G. Falle. Self-similar jets. *Mon. Not. R. Astron. Soc.*, 250:581–596, 1991.
- J. Ferreira. Magnetically-driven jets from keplerian accretion discs. *Astron. Astrophys.*, 319:340–359, 1997.
- B. Fryxell, K. Olson, P. Ricker, F. X. Timmes, M. Zingale, D. Q. Lamb, P. MacNeice, R. Rosner, J. W. Truran, and H. Tufo. Flash : An adaptive mesh hydrodynamics code for modeling astrophysical thermonuclear flashes. *Astrophys. J., Suppl. Ser.*, 131:273–334, 2000.
- K. Fukumura, F. Tombesi, D. Kazanas, C. Shrader, E. Behar, and I. Contopoulos. Magnetically driven accretion disk winds and ultra-fast outflows in pg 1211+143. *Astrophys. J.*, 805:17, 2015.
- T. A. Gardiner and J. M. Stone. An unsplit godunov method for ideal mhd via constrained transport in three dimensions. *J. Comput. Phys.*, 227:4123–4141, 2008.
- G. Gilmore, M. I. Wilkinson, R. F. G. Wyse, J. T. Kleyna, A. Koch, N. W. Evans, and E. K. Grebel. The observed properties of dark matter on small spatial scales. *Astrophys. J.*, 663:948–959, 2007.
- K. Glazebrook, C. Schreiber, I. labbé, T. Nanayakkara, G. G. Kacprzak, P. A. Oesch, C. Papovich, L. R. Spitler, C. M. S. Straatman, K.-V. H. Tran, and et al. A massive, quiescent galaxy at a redshift of 3.717. *Nature*, 544:71–74, 2017.
- T. Goerdt, B. Moore, J. I. Read, J. Stadel, and M. Zemp. Does the fornax dwarf spheroidal have a central cusp or core? *Mon. Not. R. Astron. Soc.*, 368:1073–1077, 2006.
- R. Hlozek, D. Grin, D. J. Marsh, and P. G. Ferreira. A search for ultralight axions using precision cosmological data. *Phys. Rev. D*, 91:103512, 2015.
- W. Hu and N. Sugiyama. Small-scale cosmological perturbations: An analytic approach. *Astrophys. J.*, 471:542–570, 1996.

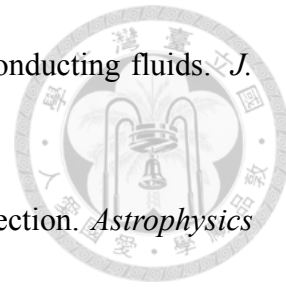


- W. Hu, R. Barkana, and A. Gruzinov. Fuzzy cold dark matter: The wave properties of ultralight particles. *Phys. Rev. Lett.*, 85:1158–1161, 2000.
- L. Hui, J. P. Ostriker, S. Tremaine, and E. Witten. Ultralight scalars as cosmological dark matter. *Phys. Rev. D*, 95:043541, 2017a.
- L. Hui, J. P. Ostriker, S. Tremaine, and E. Witten. Ultralight scalars as cosmological dark matter. *Phys. Rev. D*, 95:043541, 2017b.
- V. Iršič, M. Viel, M. G. Haehnelt, J. S. Bolton, and G. D. Becker. First constraints on fuzzy dark matter from lyman- $\alpha$  forest data and hydrodynamical simulations. *arXiv:1703.04683*, 2017.
- D. Kazanas, K. Fukumura, E. Behar, I. Contopoulos, and C. Shrader. Toward a unified agn structure. *Astron. Rev.*, 7:92–123, 2012.
- A. Klypin, A. V. Kravtsov, O. Valenzuela, and F. Prada. Where are the missing galactic satellites? *Astrophys. J.*, 522:82–92, 1999.
- R. M. Kulsrud and S. W. Anderson. The spectrum of random magnetic fields in the mean field dynamo theory of the galactic magnetic field. *Astrophys. J.*, 396:606–630, 1992.
- R. M. Kulsrud, R. Cen, J. P. Ostriker, and D. Ryu. The protogalactic origin for cosmic magnetic fields. *Astrophys. J.*, 480:481–491, 1997.
- Z.-Y. Li and C. F. McKee. Hydromagnetic accretion shocks around low-mass protostars. *Astrophys. J.*, 464:373–386, 1996.
- P. Londrillo and L. D. Zanna. High-order upwind schemes for multidimensional magnetohydrodynamics. *Astrophys. J.*, 530:508–524, 2000.
- V. Lora and J. Magaña. Is sextans dwarf galaxy in a scalar field dark matter halo? *J. Cosmology Astropart. Phys.*, 09:011–, 2014.
- C.-P. Ma and E. Bertschinger. Cosmological perturbation theory in the synchronous and conformal newtonian gauges. *Astrophys. J.*, 455:7–25, 1995.



- A. V. Macciò, S. Paduroiu, D. Anderhalden, A. Schneider, and B. Moore. Cores in warm dark matter haloes: a catch 22 problem. *Mon. Not. R. Astron. Soc.*, 424:1105–1112, 2012.
- D. J. Marsh. Axion cosmology. *Phys. Rep.*, 643:1–79, 2016.
- D. J. Marsh and J. Silk. A model for halo formation with axion mixed dark matter. *Mon. Not. R. Astron. Soc.*, 437:2652–2663, 2014.
- D. J. E. Marsh and A. R. Pop. Axion dark matter, solitons and the cusp–core problem. *Mon. Not. R. Astron. Soc.*, 451:2479–2492, 2015.
- C. F. McKee. Theory of star formation. *Annu. Rev. Astron. Astrophys.*, 45:565–687, 2007.
- B. Moore. Evidence against dissipationless dark matter from observations of galaxy haloes. *Nature*, 370:629–631, 1994.
- B. Moore, S. Ghigna, F. Governato, G. Lake, T. Quinn, J. Stadel, and P. Tozzi. Dark matter substructure within galactic halos. *Astrophys. J.*, 524:L19–L22, 1999.
- D. J. Mortlock, S. J. Warren, B. P. Venemans, M. Patel, P. C. Hewett, R. G. McMahon, C. Simpson, T. Theuns, E. A. González-Solares, A. Adamson, and et al. A luminous quasar at a redshift of  $z = 7.085$ . *Nature*, 474:616–619, 2011.
- S. Naoz and R. Narayan. Generation of primordial magnetic fields on linear overdensity scales. *Phys. Rev. Lett.*, 111:051303, 2013.
- J. F. Navarro, C. S. Frenk, and S. D. M. White. A universal density profile from hierarchical clustering. *Astrophys. J.*, 490:493–508, 1997.
- S. A. Orszag and C.-M. Tang. Small-scale structure of two-dimensional magnetohydrodynamic turbulence. *J. Fluid Mech.*, 90:129–143, 1979.
- E. Papastergis, R. Giovanelli, M. P. Haynes, and F. Shankar. Is there a “too big to fail” problem in the field? *Astron. Astrophys.*, 574:A113, 2015.

E. N. Parker. Sweet's mechanism for merging magnetic fields in conducting fluids. *J. Geophys. Res.*, 4:509–520, 1957.



C. E. Parnell and A. L. Haynes. Three-dimensional magnetic reconnection. *Astrophysics and Space Science Proceedings*, 19:261–276, 2010.

G. Pelletier and R. E. Pudritz. Hydromagnetic disk winds in young stellar objects and active galactic nuclei. *Astrophys. J.*, 394:117–138, 1992.

H. E. Petschek. Magnetic field annihilation. *NASA Special Publication*, 50:425, 1964.

W. H. Press, S. A. Teukolsky, W. T. Vetterling, and B. P. Flannery. *Numerical Recipes: the Art of Scientific Computing, 3rd Edition*. Cambridge University Press, 2007.

R. E. Pudritz, M. J. Hardcastle, and D. C. Gabuzda. Magnetic fields in astrophysical jets: From launch to termination. *Space Sci. Rev.*, 169:27–72, 2012.

L. Rayleigh. Investigation of the character of the equilibrium of an incompressible heavy fluid of variable density. *Proc. London Math. Soc.*, 14:170–177, 1883.

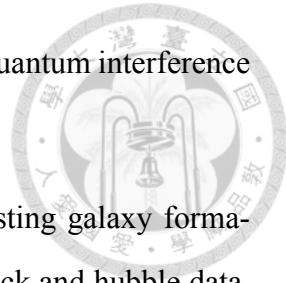
M. N. Rosenbluth, R. Y. Dagazian, and P. H. Rutherford. Onlinear properties of the internal  $m = 1$  kink instability in the cylindrical tokamak. *Phys. Fluids*, 16:1894–1902, 1973.

D. Ryu and T. W. Jones. Numerical magnetohydrodynamics in astrophysics: Algorithm and tests for one-dimensional flow. *Astrophys. J.*, 442:228–258, 1995.

H.-Y. Schive and T. Chiueh. Halo abundance and assembly history with extreme-axion wave dark matter at  $z \geq 4$ . *arXiv:1706.03723*, 2017.

H.-Y. Schive, Y.-C. Tsai, and T. Chiueh. Gamer: A graphic processing unit accelerated adaptive-mesh-refinement code for astrophysics. *Astrophys. J., Suppl. Ser.*, 186:457–484, 2010.

H.-Y. Schive, U.-H. Zhang, and T. Chiueh. Directionally unsplit hydrodynamic schemes with hybrid mpi/openmp/gpu parallelization in amr. *Int. J. High Perform. Comput. Appl.*, 26:367–377, 2012.



- H.-Y. Schive, T. Chiueh, and T. Broadhurst. Cosmic structure as the quantum interference of a coherent dark wave. *Nature Phys.*, 10:496–499, 2014.
- H.-Y. Schive, T. Chiueh, T. Broadhurst, and K.-W. Huang. Contrasting galaxy formation from quantum wave dark matter,  $\psi_{\text{dm}}$ , with  $\lambda_{\text{cdm}}$ , using planck and hubble data. *Astrophys. J.*, 818:89, 2016.
- J. Schober, D. R. G. Schleicher, and R. S. Klessen. Magnetic field amplification in young galaxies. *Astron. Astrophys.*, 560:A87, 2013.
- F. H. Shu, Z.-Y. Li, and A. Allen. Does magnetic levitation or suspension define the masses of forming stars? *Astrophys. J.*, 601:930–951, 2004.
- D. Stepanovs, C. Fendt, and S. Sheikhnezami. Modeling mhd accretion-ejection: Episodic ejections of jets triggered by a mean-field disk dynamo. *Astrophys. J.*, 796:29, 2014.
- J. M. Stone, T. A. Gardiner, P. Teuben, J. F. Hawley, and J. B. Simon. Athena: A new code for astrophysical mhd. *Astrophys. J., Suppl. Ser.*, 178:137–177, 2008.
- P. Svrček and E. Witten. Axions in string theory. *JHEP*, 06:051, 2006.
- P. A. Sweet. The neutral point theory of solar flares. In L. B., editor, *Electromagnetic Phenomena in Cosmical Physics*, volume 6 of *IAU Symposium*, page 123, 1958.
- G. I. Taylor. The instability of liquid surfaces when accelerated in a direction perpendicular to their planes. *Proc. R. Soc. London Ser. A*, 201:192–196, 1950.
- J. B. Taylor. Relaxation and magnetic reconnection in plasmas. *Rev. Mod. Phys.*, 58:741–763, 1986.
- E. F. Toro. *Riemann Solvers and Numerical Methods for Fluid Dynamics: a practical introduction, 2nd Edition*. Springer, New York, 1999.
- M. Torrilhon. Exact solver and uniqueness conditions for riemann problems of ideal magnetohydrodynamics. In *technical report 2002-06*, Zurich: Seminar for Applied Mathematics, ETH, 2002.



M. Torrilhon. Non-uniform convergence of finite volume schemes for riemann problems of ideal magnetohydrodynamics. *J. Comput. Phys.*, 2003:73–94, 2003.

L. Visinelli. Light axion-like dark matter must have anthropic origins. *arXiv:1703.08798*, 2017.

M. G. Walke and J. Peñarrubia. A method for measuring (slopes of) the mass profiles of dwarf spheroidal galaxies. *Astrophys. J.*, 742:20, 2011.

T. P. Woo and T. Chiueh. High-resolution simulation on structure formation with extremely light bosonic dark matter. *Astrophys. J.*, 697:850–861, 2009.